UNIVERSIDAD NACIONAL AUTÓNOMA DE MÉXICO

FACULTAD DE CIENCIAS

Fundamental Study into Rotor Outwash and Dust Kick-up under Mars-like Conditions

T E S I S

QUE PARA OBTENER EL TÍTULO DE:

FÍSICA

P R E S E N T A :

MARIA REGINA APODACA MORENO

DIRECTOR DE TESIS:
DR. CARLOS MÁLAGA IGUIÑIZ

2018

CIUDAD UNIVERSITARIA, CD. MX

Datos del Jurado

1. Datos del Alumno
   Apodaca
   Moreno
   Maria Regina
   52 80 13 94
   Universidad Nacional Autonoma de México
   Facultad de Ciencias
   Física
   313713084

2. Datos del tutor
   Dr
   Málaga
   Iguiñiz
   Carlos

3. Datos del sinodal 1
   Dra
   Stern
   Forgach
   Catalína Elizabeth

4. Datos del sinodal 2
   Dr
   Escobar
   Sotomayor
   Juan Valentin

5. Datos del sinodal 3
   Dr
   Olvera
   Chávez
   Arturo

6. Datos del sinodal 4
   Dr
   Rendón
   Garrido
   Pablo Luis

7. Datos del trabajo escrito
   Fundamental Study into Rotor Outwash and Dust Kick-up under Mars-like Conditions
   115
   2018

Abstract

Humans have reached a limit as to how much information can be collected from a purely ground-based rover exploration mission on Mars [1]. Therefore, an airborne mission would broaden our knowledge of this planet, and at the same time it would allow for a different approach to scientific research. Thus, the Mars Helicopter Scout (MHS) Project was founded. However, as this is only a technology demonstrator, its first and short-term goal is to fly in the vicinity of the Mars Rover and assess where the rover can go. This thesis project attempts to take a first step towards understanding how and if, the MHS' coaxial rotor system may produce dust kick-up and how the in and out of ground effect contribute to a possible "brownout". Brownout here on Earth means the complete or partial blockage of the pilot's vision caused by the lifting of dust particles found on the ground. In our case, we refer to blockage or miscalculations of the sensors, such as the altimeter of the MHS, caused by the kick-up of Martian sand. This thesis further consists on the study of rotor downwash/outwash.

Contents

1 Introduction **7**
1.1 The Mars Helicopter Scout 8

2 Theoretical Background **10**
2.1 Fluid Dynamics Theory 10
2.2 Helicopter Theory 13
2.3 Saltation 20
2.4 Computational Fluid Dynamics Tool 22
2.5 Particle Image Velocimetry 24

3 Design of a 30% Scale Model **25**

4 Dust Test Cell Experiment **31**
4.1 Design of Experiment Test Section 31
4.2 Methodology 34
4.2.1 White Light Experiment 35
4.2.2 Laser Wall Experiment 36

5 Tuft Testing **39**
5.1 Experimental Setup 40
5.2 Methodology 43

6 CFD Flow Field Simulations **45**
6.1 Blade Scanning and Post-Processing 45
6.2 Airfoil Table Creation 47
6.3 Blades and Body Geometry 47
6.4 Methodology 50
6.4.1 Grid Production and Time Step Selection 52

7 Flow field, Dust and Tuft Testing Results **56**
7.1 Dust Testing Results 56
7.2 Tuft Testing Results 59
7.3 Simulation Results 59
7.4 Comparison 62

8 Conclusion **71**

Appendices **74**

A Dust Results **75**
A.0.1 White Light Experiment 75
A.0.2 Laser Wall Experiment 88

B Tuft test Results **90**

C Simulation Results **102**

Chapter 1

Introduction

This thesis project is to be thought as a first approximation to a very complex problem. The dust cloud generation during take-off and landing of a rotorcraft, that may interfere with navigation systems is know as brownout. The landing of a helicopter here on Earth can become dangerous to the people on-board when trying to land over a granulated surface, i.e. snow or sand. Thus, this problem caught the attention of the NASA AMES Aeromechanics branch, as shown in the paper "Rotorcraft Downwash Flow Field Study to Understand the Aerodynamics of Helicopter Brownout" written by Alan J Wadcock and co-workers [2]. Likewise, designing a vehicle capable of multiple take-offs and landings in a different planet has also become one of NASA's main goals. The Mars Helicopter Scout project was thus proposed to be the first vehicle to accomplish this. However, given it is still a rotorcraft vehicle, the threat of a brownout during take-off and landing most be addressed. It is unknown to what extent this phenomenon occurs and how it can endanger the Mars helicopter.

The main objective of the project is to conduct the small-scale hover testing of a coaxial rotor system in and out of ground effect, to study both rotor downwash/outwash, and to examine the conditions under which dust kick-up and "brownout" does or does not occur under Mars-like conditions, with potential application to Mars Helicopter development. Given the exploratory nature of this project, it is limited to a proof of concept of testing techniques that may eventually be used on the full scale MHS. These future tests will help to determine whether or not dust kick-up can pose a problem on the performance of the MHS's altimeter.

The main limitation to this project will be the pressure at which both

the tuft testing and the dust testing will take place. Given this thesis is first approximation, it is sufficient to do testing at room pressure in order to overestimate the dust production. Since it is harder to produce saltation at low air densities [3], it is believed that at Mars-like conditions, there will be minimum dust saltation. Therefore, if tests are done in conditions that are more prone to produce saltation and yet there is none, it can then be concluded that at lower densities, or conditions closer related to those in Mars, the phenomenon will not appear. However, in the case that it is proven that saltation is possible, further testing shall be necessary. The experimental set-up was designed for future testing inside a vacuum chamber where Mars' low air densities can be reached [4].

1.1 The Mars Helicopter Scout

Mars' surface is a very difficult terrain to move around in. Its dunes, rocks and valleys make it a challenge for our vehicles to move about without danger. That is why the current Mars Rover has many difficulties when it comes to making a decision on when and towards where it should move. It relies on the images taken by itself and previous missions that have photographed The Red Planet in order to allow the control station back on Earth to decide whether it is safe for it to keep moving. This is very limiting in nature, given the amount of time lost in communicating between Earth and Mars. This is the seed that lead to the inspiration of the vertical lift vehicle that will be the subject of this project.

The Mars Helicopter Scout is, up until now, a proof-of-concept technology demonstration of what later hopes to become an auxiliary vehicle for the Mars Rover. The short term purpose of this helicopter would be to explore the terrain ahead of the rover, for target selection, path selection, and geologic context. However, for the safety of the rover, the helicopter will not land nor fly near it. Individual daily flights would be limited to $2-3$ minutes maximum due to power consumption, but it should be able to fly approximately 600 m at an altitude of 100 m from the surface.

Besides there not being a set design for this rover, there are set physical features it shall include. These features are: a total mass of 1 kg and a 1.1 m rotor diameter, powered by solar charged batteries; a high resolution camera and a communication system to rely data to the rover. The current design consist of a co-axial main rotor and a cube-shaped, 140 mm each side, body

with four legs as landing gear [1, 5].

The differences between the Martian atmosphere and that of the Earth is what makes Mars such a harsh environment for flight. Since it is composed almost entirely out of CO_2, a density instability, or abrupt change, is caused by this molecule's polar states, gaseous or solid, at pressures and temperatures commonly found in Mars (table 1.1). This poses as an extra difficulty when developing rotary-wing designs [6].

	Mean Radius (km)	Gravity (m/s^2)	Mean Surface Atmos. Temp. (°K)	Mean Surface Atmos. Pressure (Pa)	Mean Surface Atmos. Density (kg/m^3)	Atmos.Gases
Earth	6371	9.82	288.2	101,300	1.23	N_2 78% O_2 21%
Mars	3390	3.71	214	636	1.55×10^{-2}	CO_2 95% N_2 2.7% Ar 1.6% O_2 0.1 %

Table 1.1: Planetary Description[7].

Moreover, as can be seen in Table 1.1, despite Mars' gravity being a little bit over a third of Earth's gravity, the extreme low temperatures and pressure make it very difficult to produce the necessary lift to carry the helicopter given its dependency on atmospheric density (equation 3.1).

Therefore, the autonomous Vertical Take-off and Landing (VTOL) aircraft will have to be extremely light weight and with large lifting surfaces; thus, facing us with an extremely complex problem given the high Reynolds number and possible compressible flow aerodynamics.

Different designs have been proposed rotor such as a tiltrotor, a rotor that is able to change its position from perpendicular to the ground to parallel; quad-rotor, four rotors with different rotor centers; and coaxial rotors, two rotors that share the same rotor-center. The latter being the main focus of study of this project[6].

Chapter 2

Theoretical Background

Given the complexity of the proposed problem, initial background research had to be done in order to fully understand the problem. Basic knowledge of the Martian atmospheric conditions and the fundamentals of fluid dynamics, helicopter theory and computational fluid dynamics, were essential to the development of this thesis.

2.1 Fluid Dynamics Theory

Fluid mechanics governs the flight of helicopters and their interaction with its surroundings, like a dusty landing spot. Throughout this thesis, the fluid in question shall be the air surrounding the helicopter. Air is considered a Newtonian fluid, and so the flow rate of strain (the symmetrised velocity gradient) is linearly proportional to the stress tensor within the fluid. Lets use the Eulerian description of a fluid, so for example the fluid velocity field $\boldsymbol{u}(\boldsymbol{x}, t)$ is interpreted as the velocity at a specific time t of an element of fluid that coincidently passed through the point in space $\boldsymbol{x}$[9].

In the Eulerian description, mass conservation is represented by the continuity equation

$$\frac{\partial \rho}{\partial t} = \nabla \cdot (\rho \boldsymbol{u}), \tag{2.1}$$

where ρ is the density of air, that relates the local density change with the mass flux. The rate of change of the volume of the fluid elements is given by $\nabla \cdot \boldsymbol{u}$. Therefore, a flow is considered incompressible when $\nabla \cdot \boldsymbol{u} = 0$. This is equivalent, by mass conservation (2.1), to considering the density of the

fluid elements to remain constant, expressed in the material derivative of the density

$$\frac{D\rho}{Dt} = \frac{\partial \rho}{\partial t} + \boldsymbol{u} \cdot \boldsymbol{\nabla} \rho \tag{2.2}$$

where in the case of an incompressible flow, $\frac{D\rho}{Dt} = 0$. If the flow of an initially homogeneous fluid is incompressible, the density field remains constant in time and space [9]. Therefore, despite air being a compressible fluid, the air flow caused by the rotor will be considered an incompressible flow. This is justified by the condition of incompressible flow that relates the speed at which a solid moves through the fluid in hand, and the speed of sound in the same fluid, i.e. the Mach number. In this specific case, the Mach number of the blades is less than 0.3 thus it is safe to assume incompressibility [8].

On the other hand, the air is a Newtonian fluid and the stress tensor, for an incompressible flow, can be expressed as

$$\boldsymbol{\sigma}(\boldsymbol{x}, t) = -p\boldsymbol{I} + 2\mu\boldsymbol{e}, \tag{2.3}$$

where $\boldsymbol{e}$ is the rate of strain tensor $\boldsymbol{e} = \frac{1}{2}\left(\boldsymbol{\nabla u} + (\boldsymbol{\nabla u})^T\right)$, μ is the shear viscosity of the fluid and $p(\boldsymbol{x}, t)$ is the mechanical pressure, defined as the average normal stress acting on a fluid element.

The stress tensor is related to the total surface force $\boldsymbol{F}_S$ that is applied to a solid by the fluid surrounding it by

$$\boldsymbol{F}_S = \int_{\partial\Omega} \boldsymbol{\sigma} \cdot \boldsymbol{n} dS, \tag{2.4}$$

where $\partial\Omega$ is the solid boundary in contact with the fluid. On the other hand, the total thrust $\boldsymbol{T}$ of a helicopter in hover. i.e. a helicopter in stationary flight, is equal to the weight of the helicopter $\boldsymbol{W}$. In other words, it can be express as the following

$$\boldsymbol{T} = -\boldsymbol{W}. \tag{2.5}$$

In hover, the interaction of the blades with the surrounding fluid provides the force that allow the helicopter to balance gravity, then

$$\boldsymbol{T} = \boldsymbol{F}_S. \tag{2.6}$$

Now, in order to obtain the equation of motion for a volume Ω that is fixed in space, with a boundary $\partial\Omega$, we recur to Newton. Newton proposes

that the rate of change of momentum is equal to the sum of all the forces acting on the fluid plus the momentum flux through $\partial\Omega$. Therefore, if the momentum of the fluid inside Ω can be written as

$$\int_{\Omega} \boldsymbol{u}\rho dV, \tag{2.7}$$

then the rate of change can be expressed as

$$\frac{d}{dt}\int_{\Omega} \boldsymbol{u}\rho dV = -\int_{\partial\Omega} (\rho\boldsymbol{u})\boldsymbol{u}\cdot\boldsymbol{n}dS + \boldsymbol{F}, \tag{2.8}$$

If it is now assumed that the total force acting on a part of the fluid is the sum of both the volumetric and superficial forces. Then, the total force acting on the volume would be

$$\boldsymbol{F} = \int_{\Omega} \boldsymbol{f}dV + \int_{\partial\Omega} \boldsymbol{\sigma}\cdot\boldsymbol{n}dS, \tag{2.9}$$

where f is the body force density and $\sigma\cdot\boldsymbol{n}$ is the contact force per unit area or stress vector. Using the Divergence Theorem, we can rewrite the superficial forces and momentum fluxes to obtain

$$\int_{\Omega} \frac{\partial}{\partial t}(\rho\boldsymbol{u})\, dV = \int_{\Omega} (\nabla\cdot\boldsymbol{\sigma} + \boldsymbol{f})\, dV - \int_{\Omega} \nabla\cdot(\rho\boldsymbol{u}\boldsymbol{u})\, dV. \tag{2.10}$$

Given that the selected volume Ω, is an arbitrary region in space, we can say that the relation exists between the integrands

$$\frac{\partial}{\partial t}(\rho\boldsymbol{u}) = (\nabla\cdot\boldsymbol{\sigma} + \boldsymbol{f}) - \nabla\cdot(\rho\boldsymbol{u}\boldsymbol{u})\,. \tag{2.11}$$

If the derivatives are now opened and the different parts rearrange, the equation is now:

$$\boldsymbol{u}\left[\frac{\partial\rho}{\partial t} + \nabla\cdot(\rho\boldsymbol{u})\right] + \rho\frac{\partial\boldsymbol{u}}{\partial t} = \nabla\cdot\boldsymbol{\sigma} + \boldsymbol{f} - \rho\boldsymbol{u}\cdot\nabla\boldsymbol{u}. \tag{2.12}$$

However, thanks to equation 2.1, it is known that the parenthesis in the left side of the equation, since the fluid is considered incompressible, is equal to zero

$$\rho\left[\boldsymbol{u}\cdot\nabla\boldsymbol{u} + \frac{\partial\boldsymbol{u}}{\partial t}\right] = \nabla\cdot\boldsymbol{\sigma} + \boldsymbol{f}. \tag{2.13}$$

Now, that which is inside the parenthesis in the left side of the equation, can be seen as the material derivative of $\boldsymbol{u}$

$$\rho \frac{D\boldsymbol{u}}{Dt} = \boldsymbol{f} + \nabla \cdot \boldsymbol{\sigma}. \tag{2.14}$$

If we now substitute the expression found for the stress tensor in equation 2.3 in the previous equation we obtain what is commonly known as Navier-Stokes equation of motion:

$$\rho \frac{D\boldsymbol{u}}{Dt} = \boldsymbol{f} - \nabla p + \mu \nabla^2 \boldsymbol{u}. \tag{2.15}$$

With equations 2.1 and the condition of incompressibility $\nabla \cdot \boldsymbol{u} = 0$ and the equations 2.3,2.15 there are now 4 equations to solve for the velocity $\boldsymbol{u}$ and mechanical pressure p. The initial conditions, such as a no-slip boundary conditions of the fluid around a solid, give further constraints to solve the problem. The no-slip condition means the fluid at the boundary has the same velocity as the solid boundary itself.

2.2 Helicopter Theory

In this section, both the momentum theory and the blade element theory shall be discussed. These two theories are used to explain and simulate the flight of a rotorcraft. For the purpose of this thesis, they are important because the software used to make the simulations, RotCFD, combines them in order to simulate rotorcraft downwash. Furthermore, both theories produce variables of extreme importance to the description of the phenomena addressed by this thesis. Examples of such variables are v_H, the wake velocity, and C_T, the thrust coefficient. The wake velocity is the maximum velocity the fluid in the wake will reach and thus is taken to be the one responsible for saltation (the kick-up of dust). Additionally, C_T was used in this research to assure that the scaling of the problem was done correctly and that we are solving a dynamically similar problem to that in Mars.

A helicopter is an aircraft that uses rotating wings to provide lift, propulsion and control. In contrast to an fixed-wing aircraft, a helicopter is capable of producing aerodynamic forces even when the velocity of the vehicle itself is zero. Thus, allowing it to take-off and land vertically [10].

A helicopter is in hover when it has no velocity relative to the ground, let that be vertical o horizontal. While vertical flight, as the name suggests,

is a vertical movement, it implies axial symmetry of the rotor, causing the velocities and loads on the rotor blades to be independent of the azimuthal position.

In order to do a general analysis of the problem, momentum theory can be used. Momentum theory applies the conservation laws of fluid mechanics (mass, momentum and energy) to the rotor and flow as a whole to estimate the rotor performance. In this theory, the rotor is modelled as an actuator disk. That is, a circular surface of zero thickness that can support a pressure difference and thus accelerate the air through the disk. Moreover, the actuator disk can also support torque, which can thus impart angular momentum to the fluid that passes through the disk [10]. Figure 2.1 shows a diagram of

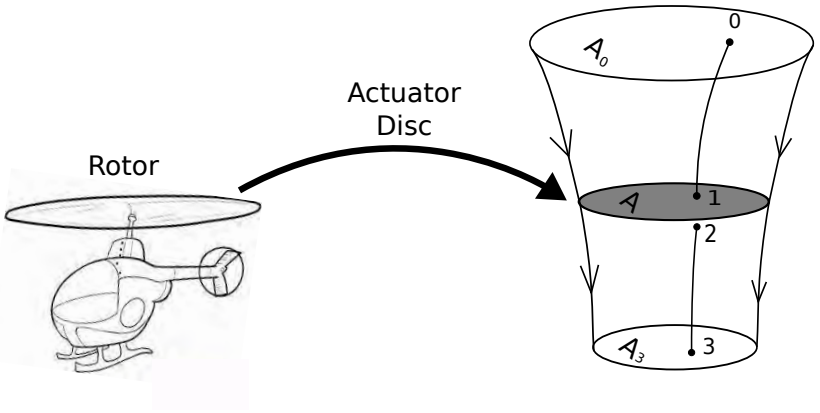

Figure 2.1: Diagram exemplifying the Momentum Theory and actuator disk approximation.

the idealized flow across the actuator disc in hover. The flow is considered to be irrotational and incompressible above and below the actuator disc. The idealized flow across the actuator disc consists of a streamtube, and Ω represents a section of the streamtube split by the actuator disc somewhere in the middle. In Momentum Theory, a relation for the thrust on the rotor can be found by first considering the pressure difference in both sides of the disc and using the Bernoulli equation. Take a stream line starting way above the disc, at the point 0 of figure 2.1 and ending right above the disc, at point 1. Similarly a second streamline can be used below the disc, say from point 2 below the disc to point 3 far away. Using Bernoulli in both streamlines we obtain

$$\begin{aligned} p_0 + \tfrac{1}{2}\rho u_0^2 &= p_1 + \tfrac{1}{2}\rho u_h^2, \\ p_2 + \tfrac{1}{2}\rho u_h^2 &= p_3 + \tfrac{1}{2}\rho w^2, \end{aligned} \tag{2.16}$$

where p_0 to p_3 are the pressure at points 0 to 3 respectively, ρ is the uniform fluid density, u_H is the fluid speed across the disc in points 2 and 3, u_0 and w are the fluid speed in points 0 and 3 respectively. Pressures p_0 and p_3 are approximately the atmospheric pressure. and the pressure difference across the disc represent the magnitude of the thrust T distributed over the disc area A, giving $T/A = p_2 - p_1$. Adding the relations (2.16) we obtain

$$T/A = \tfrac{1}{2}\rho w^2. \tag{2.17}$$

Now consider the momentum balance in Ω given by equation (2.9). Since the velocity field is steady and density is constant the momentum in Ω remains constant and the left hand side of equation (2.9) is zero. The actuator disc imposes a force $-T\hat{\boldsymbol{e}}_z$ on the flow, that appears as a source term in the momentum balance 2.9, leading to the following expression:

$$0 = -\int_{\partial\Omega} \rho \boldsymbol{u}(\boldsymbol{u}\cdot\hat{\boldsymbol{n}})ds + \int_{\partial\Omega} \boldsymbol{\sigma}\cdot\hat{\boldsymbol{n}}ds + \int_{\Omega} \boldsymbol{f}dV - T\hat{\boldsymbol{e}}_z. \tag{2.18}$$

The first integral, the flux of momentum, is roughly $-A_0\rho u_0^2\hat{\boldsymbol{e}}_z + A_3\rho w^2\hat{\boldsymbol{e}}_z$, where u_0 is so small it is negligible compared to w. Meanwhile, the stress integral is approximately $A_3 p_3\hat{\boldsymbol{e}}_z - A_0 p_0\hat{\boldsymbol{e}}_z$, neglecting the contribution coming from the side boundaries. The force applied by the actuator disc, equivalent to the weight of the helicopter, must be considerably larger than the weight of the air in Ω, the integral of $\boldsymbol{f}$. Also, as p_0 and p_3 are equal to the atmospheric pressure, it is reasonable to consider the effect of stresses on $\partial\Omega$ as well as the momentum flux across A_0 to be much smaller than T, reducing equation (2.18) to $-T\hat{\boldsymbol{e}}_z + A_3\rho w^2\hat{\boldsymbol{e}}_z = 0$. Since mass is conserved, mass flux $A_3\rho w$ is equal to $A\rho u_H$, and thrust can be expressed as

$$T = A\rho u_H w. \tag{2.19}$$

Using relation (2.17) an estimate to the velocity below the rotor is obtained

$$u_H = \sqrt{\frac{T}{2\rho A}}. \tag{2.20}$$

On the other hand, in order to explain Blade element theory, lets first introduce some of the terms related to the rotor blade (see Figure 6.4). In this context an airfoil is a 2D representation of a rotor blade which is used to study the aerodynamic forces present when interacting with an air stream. The imaginary straight line that exist between the leading edge and the trailing edge is known as the chord line. The leading edge is the first point of contact between the airfoil and the air stream. While the trailing edge is the opposite end of the airfoil. The blade twist refers to a change (a twist) of the chord line. The angle of attack is the angle between the blade chord line and the direction of the free air stream. Flapping is when the blade is allowed to increase and decrease the angle of attack of each blade during rotation. What is known as the hinge offset is the movement of the flapping hinge from the center of the mast. The pitch angle is the angle between the chord line and the reference plane, which is the same one as that of the rotor hub. If we look at figure 2.3, this reference plane would be the horizontal axis [11]. The collective pitch refers to the pitch angle at which all blades are from the reference plane. Meanwhile, the cyclic pitch refers to the change in angle of each blade depending in its azimuthal position. Lastly, when the helicopter is making a vertical take-off, there are two main forces acting on the rotor blades, the lift that allows it to carry the weight of the helicopter and the centrifugal force on the rotating blades. The result of these two forces on the blades is the coning of their path, as opposed to staying in their original flat position. The angle at which they cone is known as the cone angle.

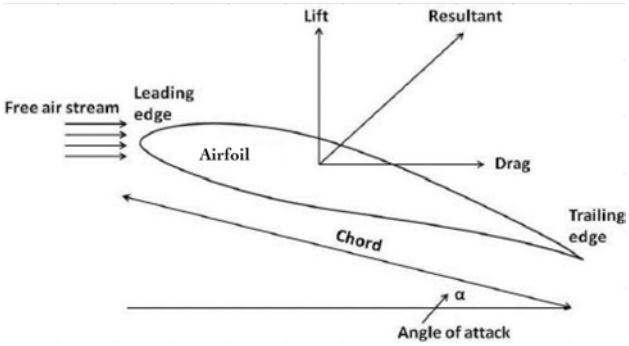

Figure 2.2: Airfoil section diagram where the geometric characteristics are pointed out.[12]

The blade element theory is based on the lifting-line assumption. The Lift-lining assumption considers only rigid flap motion and no lag or pitch

degrees of freedom. Blade Lag is the forward and backwards movement of the blade along the plane of rotation. Lift-lining also assumes small angles and neglects effects of stall, compressibility and radial flow. Stall is when the lift produced by the airfoil is reduced, this occurs when the angle of attack is increased passed the critical angle of attack. Moreover, the blade must have a constant Chord and linear twist. A uniform induced velocity, or the velocity of the fluid surrounding the blades caused by their movement, is also considered [10].

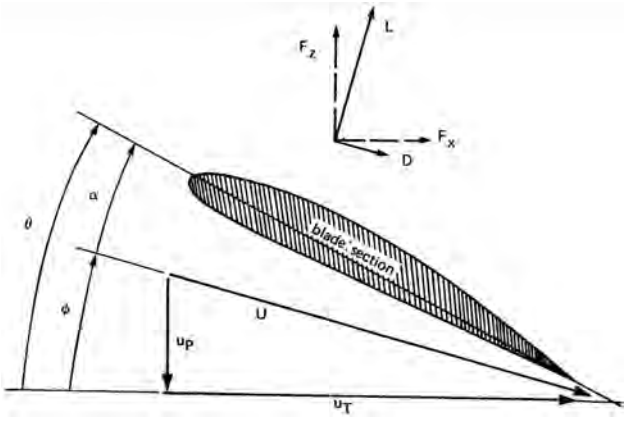

Figure 2.3: Blade section aerodynamics diagram [10].

In figure 2.3 the velocities and forces acting on the blade are shown. The free air stream has two velocity components in this figure, $\boldsymbol{u}_T$ air velocity component tangential to the disk plane, and $\boldsymbol{u}_P$ is the air velocity perpendicular to the disk plane. Therefore, the air stream has a speed

$$U = \sqrt{u_T^2 + u_p^2}, \tag{2.21}$$

and makes an angle with respect to the disk plane given by

$$\phi = \tan^{-1} \frac{u_P}{u_T} \tag{2.22}$$

Given that the air stream can be blowing in any direction, since it is defined by the weather conditions, this angle can be different to zero in hover. Thus, the angle of attack can be defined mathematically as

$$\alpha = \theta - \phi, \tag{2.23}$$

where θ is the angle between the chord line and the plane of rotation. This angle can also take values different to zero since it is the pitch angle of the blades. Additionally, the forces that are being produced by the air flow around the blade are lift, $\boldsymbol{L}$, and drag, $\boldsymbol{D}$. These forces, as shown on the diagram (figure 2.3), are parallel to the related wind ($\boldsymbol{U}$), in the case of the drag, and perpendicular in the case of the lift. The lift coefficient, C_L, and the drag coefficient, C_D, can be defined as

$$L = \frac{1}{2}\rho U^2 C C_L \tag{2.24}$$

$$D = \frac{1}{2}\rho U^2 C C_D \tag{2.25}$$

where ρ is the air density, C the chord.

However, the resultant force can be split into two components $\boldsymbol{F}_x$ and $\boldsymbol{F}_z$ that are parallel and perpendicular to the disk plane, respectively. They are calculated as follows:

$$F_x = L\sin\phi + D\cos\phi \tag{2.26}$$

$$F_z = L\cos\phi - D\sin\phi \tag{2.27}$$

From these, important characteristics of the rotor can be approximated such as the thrust

$$\boldsymbol{T} = N\int_0^R \boldsymbol{F}_z dr, \tag{2.28}$$

where N is the number of blades. These are the values that the blade element provides that are useful when designing a rotor.

The way this theory is implemented into the simulations is by including what is known as the airfoil tables. Given that most blades have smooth surfaces, it is possible to approximate how these 3D objects interact with the fluid, the integral in eqn. (2.28) by solving a 2D boundary layer problem with some of its cross-sections. The airfoil tables contain information about the forces on the cross-sections for different angles of attack.

Another concept in helicopter theory that is essential for this thesis is Ground effect. Ground effect is the name given to the phenomenon that occurs when the rotor dish is in proximity to the ground. What happens is that the induced velocity of the airflow through the rotor disk as well as the rotor wake are constricted and modified by the surface friction. When the

helicopter is out of ground effect, there are two "inner vortices" that produce stall. These vortices appear at the blades tips and close to the rotor mast, reducing lift in these portions of the blade. Interaction with the ground restricts the generation of blade tip vortices making a larger portion of the blade produce lift (Figure 2.4). All these factors contribute to the increase in thrust. This effect is limited to height of about a diameter of the rotor above the ground, and reaches its maximum over a firm smooth surface [11].

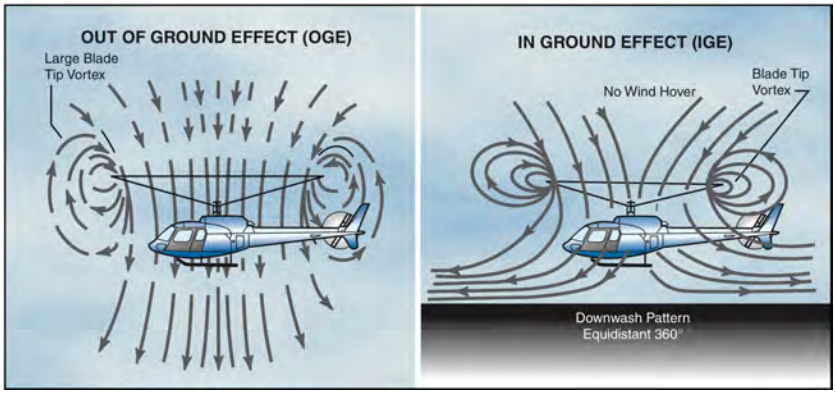

Figure 2.4: Air circulation patterns change when hovering out of ground effect and when hovering in ground effect [11].

The Rotorcraft brownout is the result of the entrainment of dust and/or sand particles due to helicopter downwash. It can also be referred to as whiteout when landing over powdered snow. This effect while landing poses a problem since the dust can reduce or completely block the pilot's visibility. Brownout, can be divided into 3 parts: helicopter downwash, particle entrainment and visual obscuration. Particles become airborne outside the rotor disk at the same distance that the maximum outwash velocity is reached [2]. The three main transport modes for particles on a surface are: surface creep, saltation and suspension. The first one occurs for low-speed flows, since the force being exerted on them only have energy to roll them on the surface. At higher-speed flows, there is saltation, a process in which the particle becomes airborne [13]. Suspension happens once the particles are off the ground and the flow has a high enough speed to counteract the gravitational pull.

2.3 Saltation

Saltation is one of the many ways the wind can transport particles on the surface. The word "saltation" comes from the Latin word "saltare", which means to leap, making the word seem appropriate since the grains being moved by saltation are actually bouncing. Bagnold's "The Physics of Blown Sand and Desert Dunes" [13] talks about two different threshold flow velocities to produce saltation, the static threshold and the dynamic threshold. For the purpose of this thesis, we shall focus purely on the static threshold velocity. That is the necessary wind conditions that will allow the particles of a given size and density to initiate motion from rest. This threshold depends on both the properties of the airflow and the gravitational and interparticle cohesion forces that oppose the motion. The effective gravitational force on the particle, including the buoyancy force, is

$$F_g = \frac{\pi}{6}(\rho_p - \rho)gD^3, \tag{2.29}$$

where g is the gravitational acceleration, D_p is the particles diameter, assuming that the dust particle is spherical. ρ_p is the particle density while ρ is that of the fluid. The drag force exerted by the fluid on a particle is given by

$$F_D = K_d \rho D^2 u_*^2, \tag{2.30}$$

where K_d is a dimensionless coefficient and the threshold friction velocity u_*.[14] The threshold surface stress (τ_t) necessary to start particle motion is directly proportional to the threshold friction velocity

$$\tau_t = \rho u_*^2, \tag{2.31}$$

where ρ is the fluid density and, according to Bagnold, the threshold friction velocity u_* on Earth can be determine by

$$u_* = A\sqrt{\frac{(\rho_p - \rho)gD}{\rho}}, \tag{2.32}$$

where ρ_p is the particle density, g is the gravitational acceleration, D_p is the mean particle diameter and A is an experimental coefficient. Therefore u_* is the flow threshold shear velocity at which saltation is initiated. Bagnold believed A to be a unique function of the particles friction Reynolds number

$$Re = \frac{u_* D_p}{\nu}, \tag{2.33}$$

where ν is the kinematic viscosity. Bagnold and Sagan tried to find a relationship between these two coefficients such that $A = A(Re)$ [13]. This would mean that if we knew Earth's A and Re we could extrapolate this to treat saltation under Mars conditions. However, the results obtained by Iversen *et al.* [3] combined with those by Weinberger and Adlon [15], suggest that the universality of $A(Re)$ for small particles at low pressures is invalid.

The effects of winds upon a loose particulate surface at low pressure, as is the case of the Martian surface, is still a matter of current debate [13], thus, causing there to be a wide range of results for the predicted threshold wind speed, or minimum speed required to cause saltation, at such a low pressure. This project will take the results found by R Greeley *et al.* on "Dust Storms on Mars: Considerations and Simulations" to select the size and material of the particles for the experiments [3]. Despite not satisfying all parameters involved in simulating an aeolian motion in Mars when doing an experiment inside a wind-tunnel conducted on Earth, this paper found an optimum grain size for Mars. That is, the size at which saltation occurs by the lowest winds.

Since Gravity on Mars is 0.38 that of Earth, less force is required to initiate particle lift and movement in Mars. For threshold simulations conducted on Earth, the particles must be 0.38 the density of their equivalent in Mars. Ground walnut shells are the right density and shape to that of the natural windblown materials in Mars [3].

Moreover, in the research done by Greeley, White *et al.* [3], it was found that the particle size with the lowest friction threshold speed at pressures within $10^5 Pa$ to $400 Pa$, were the samples of 64 μm and 330 μm average diameter of ground walnut shells [3]. It was further determined that the minimum threshold friction speed to cause saltation on Mars at its average surface pressure of 500Pa is 2.5 m/s. Additionally, it is concluded that the particle size that is the easiest to move is that of 160 μm in diameter. On the other hand, given that the speed is inversely proportional to the pressure of the test section, the threshold velocity at a pressure of 1000 mb is of 22.61 cm/s (0.02261 m/s). Therefore, we assume this value to be the minimum speed necessary to move particles.

2.4 Computational Fluid Dynamics Tool

Flow simulations used in this work were produced with a program called RotCFD. RotCFD is a computational fluid dynamics (CFD) tool developed at Surka Helitek, Inc. that emphasizes user-friendliness and efficiency that streamline the design process from geometry to CFD solution. RotCFD brings together CFD and Integrated Design Environment (IDE) specifically for rotorcrafts. One of RotCFD's key components is its geometry module. With it, the user is able to import a body geometry in a STL or Plot3D format, which are standard CAD program formats (Computer-Aided Design). Additionally, the user may alter these designs by applying transformations such as rotations, translations and scaling [16].

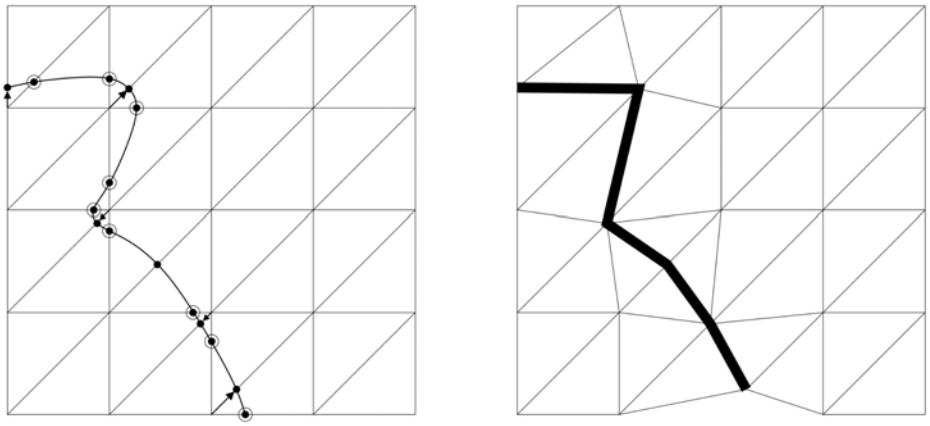

Figure 2.5: 2-D Example of a Body Conforming Grid [17].(The difference betweem both panels is explained in the text.)

Another key component is its semi-automated grid generation module or "UGen". This module generates a Cartesian Octree grid that allows refinement in specified regions of intrest. Octree is a data structure in which a given number of grid cubes are subdivided into 8 smaller grid cubes, producing a local mesh refinement. RotCFD also uses "Body Conforming Gird", a technique that moves the vertices of the grid to fit a given boundary, like the fuselage of a rotorcraft, distorting the shape of the neighboring cell. The cells that intersect the body or are surrounding it are replaced by tetrahedra. To further illustrate this technique, Figure 2.5 shows two drawings. The left panel shows the original grid and the curve represents the outline of an ob-

ject. The right panel shows the result of this grid generation caused by the presence of the object [17].

The grid is not the only approximation, since a new body surface is being generated form these new edges. This produces distortions on the body which are obvious on the example geometry found in Figure 2.6 [16].

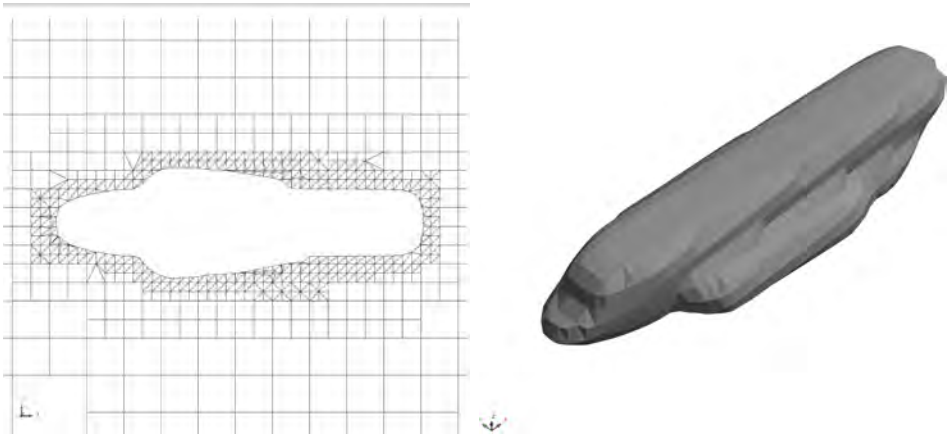

Figure 2.6: Fitted grid around a surface and an example of 2-D Octree Grid (left) and surface faces of the fitted grid (right).[17]

The rotor module is also one of the most important features of RotCFD. This module is based on the concept of rotor blades represented as momentum sources. The rotor momentum sources are primarily a function of the local velocity of the flow, given by the numerical algorithm the solves the Navier-Stokes equations and the two-dimensional airfoil characteristics of the rotor blades. The Navier-Stokes equations and the blade element theory are coupled implicitly in order to obtain the rotor performance and flow field. While the blade element theory provides the forces acting on the rotor blades, the numerical algorithm that solves the Navier-Stokes equations yields the flow field near the rotor blades, including the induced momentum sources.

RotCFD utilizes an incompressible, unsteady Navier-Stokes solver with a staggered grid, based on finite volume method with either implicit or explicit time integration. The pressure field is computed using a SIMPLE algorithm (Semi-Implicit Method for Pressure Linked Equations) [16].

Lastly, a flow visualization and analysis module is included in this program. The idea of having a Graphical User Interface (GUI) is to facilitate the CFD post-processing by allowing the user to visualize the results.

2.5 Particle Image Velocimetry

The Particle Image Velocimetry (PIV) method of visualization of fluids is used to map the velocity field by inserting tracer particles. When using this method, it is assumed that the tracer particles are of equal density to the fluid they are in, and the move along with it without interfering with the velocity fields. In this thesis, dust particles were used as tracers and PIV used to visualize the motion of the dust cloud generated by the helicopter model.

This method illuminates the tracer particles with either a stroboscopic light or a laser, in order to measure the flow velocity field. In this thesis, the PIV statistical analysis needed to obtain the velocity field was performed using the Matlab's PIV package [18]. This package uses cross-correlation to locate the particles in parts of the image in a designated search area, specified by the user.

Chapter 3

Design of a 30% Scale Model

The 30% scale model of the MHS was designed specifically for the experiments described in this thesis. The model was built trying to preserve the shape and the rotor configuration of the full size prototype. Previously, a half-scale version was made in order to run flight tests inside a wind tunnel. The tunnel was designed in order to fit inside a vacuum chamber located at the NASA AMES Research Centre. However, this model was not used in the tests for this thesis.

The dimensions of the experimental model were based on data that has been made public by California Institute of Technology's Jet Propulsion Laboratory, also known as NASA JPL (Figure 3.1). This centre is the main research facility in charge of the Mars Helicopter Scout (MHS) project. Real and accurate dimensions were not made available for the purpose of this thesis except for the real size of the cube box that will be the body of the helicopter.

The electric and mechanical systems used in the design of the model were taken from an off-the-shell RC helicopter. This is a GPTOYS G610 11" ($279.4mm$) Durant Built-in Gyro Infrared Remote Control Helicopter. This helicopter was selected for the size of the blades since it was the closest we could find off-the-shelf of approximately 30% of the full size of the MHS rotor disk diameter D ($D = 1.1m$).

Moreover, the size of the rotor disk was not the only feature of the MHS that had to be scaled in order to consider this model. This model had to fit inside a fuselage that also represented the 30% of the MHS cubed body. The model will now be referred to as the M3HS. At the same time, there were things that had to remain the same, such as the Thrust coefficient, C_T. The

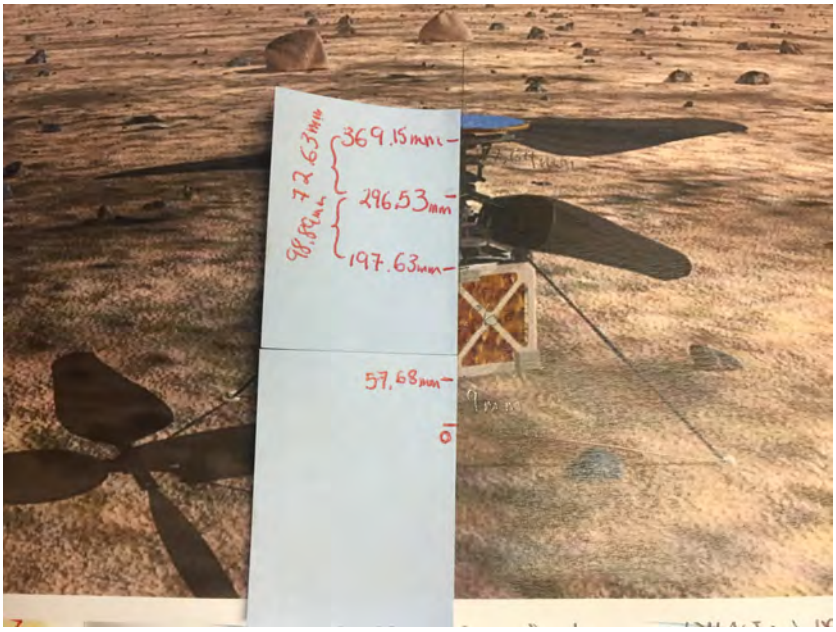

Figure 3.1: Measurements made to the MHS artist's concept.

Thrust Coefficient of a rotor is defined by the formula

$$C_T = \frac{T}{\rho \pi u_{tip}^2 R^2}, \tag{3.1}$$

where T represents the thrust, ρ the density of the atmosphere, R the radius of the rotor disk and u_{tip} is the rotors tip velocity. Given equation 2.20, and knowing that the area of the disk is $A = \pi R^2$ then the scaled wake velocity is given by

$$\frac{u_H}{u_{tip}} = \sqrt{2C_T}. \tag{3.2}$$

The problem can now be considered equivalent if the C_T is specified. Since we consider u_H to be responsible for saltation, we may compare it to that of the full-scale problem.

Therefore, a thrust test was necessary to determine these values. In order to do the thrust test, and further tuft and dust testing, the motors and the rotor had to be removed from the original toy's fuselage. The motors were then placed in a new fuselage that would hold them steady and, at the same time, would have a similar shape and size of the real Mars Helicopter Scout

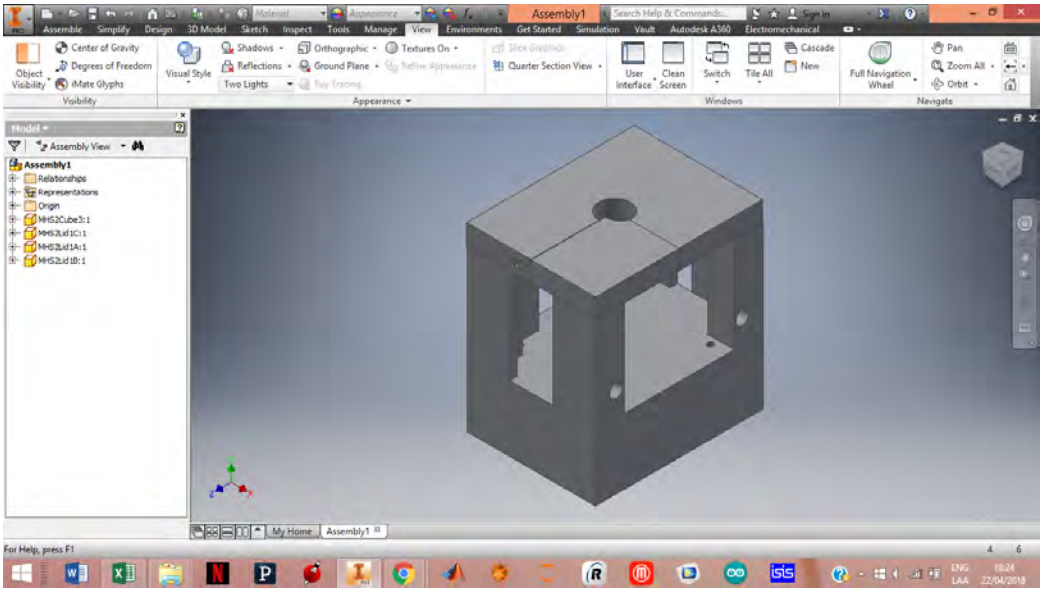

Figure 3.2: Screen shot of the fuselage design using Inventor.

fuselage. This was done using a mechanical design software and 3D CAD software called Inventor. However, given the size of the gear system, the shape of the fuselage could not be fully cubed. Although we could adjust both the height and width of the cube to be the right size, the depth had to be modified to fit the gears. Once the size of the box was designed, an adaptor was then added in order to attach the fuselage to the mounts (Figure 3.2). The dimensions of the fuselage were 39 $mm \times 51$ $mm \times 40$ mm. This design includes side holes to keep cool the motors. The motors would heat up so much it melted older designs that had no ventilation. Lastly, the fuselage was printed using a 3D printer with 30% infill. This level of filling guaranteed the stiffness necessary to avoid vibrations and movement of the body and mast.

Once the model was ready, it was placed on a sting mount that was to be used for the thrust experiment. This experiment consisted on placing the model directly above a ground plate of 1.5 $D \times 1.5$ D, with D now being the diameter of the scaled rotor. In our case $D = 55.8$ cm (22 in). The plate was placed on top of a scale in order to measure the thrust by means of the hydrodynamic force of the flow, produced by the rotor right above, pushing down the plate (figure 3.3). Meanwhile, a tachometer was held steadily and perpendicular to the rotor disk. By placing a reflective sticker on one of the

blade tips, the revolutions per minute (RPM) of the model could be measured at all times. The results of this experiment are shown on Figure 3.3. The blue points represent the data points from the experiment. The blue line represents the linear trend line. From the RPM shown on figure 3.3(top) the tip velocity u_{tip}, was calculated using

$$u_{tip} = \frac{RPM \times R \times \pi}{60s}, \tag{3.3}$$

where R is the radius of the rotor disk and the u_{tip} is in m/s. Meanwhile, the red points in figure 3.3 represent the average values taken from these results, and were used as the tip velocity input in the RotCFD simulations.

From these graphs and using equations 2.20 and 3.1, the following comparison was done. It can be seen on table 3.1 that most variables are roughly the same percentage except for the thrust coefficient that should be the same. Furthermore, this helicopter model seems to be good enough for these initial studies since u_H is bigger than the predicted threshold velocity needed to move the dust particles under Earth conditions [3].

	Full Size MHS	Scaled Model	Percentage
Volume	$140mm \times 140mm \times 140mm$	$39mm \times 51mm \times 40mm$	28.99%
u_{tip}	138.2301 m/s	37.6005 m/s	29.76%
u_H	8.08128 m/s	2.3107 m/s	28.59%
C_T	0.0068	0.0064	93.68%

Table 3.1: Summary of model's Characteristics compared to real MHS in Earth conditions.

One of the original restrictions set to this model were costs. This model's original purpose was to function as an outreach project. Therefore, although the components were selected to be as accurate as possible, they were possibly not the best choice. Moreover, all of the testing done in this thesis is at sea level Earth pressure. Further testing is suggested at Martian pressures, however it is possible that this toy device will not function at such low pressures.

Scaling in this thesis is of high importance since it is by which we justify using a small version of the MHS and experiments done on Earth in order to have a better idea of what may happen with the full-scale MHS in Mars. The most important scaling is found in equation 3.2. Here the u_H velocity,

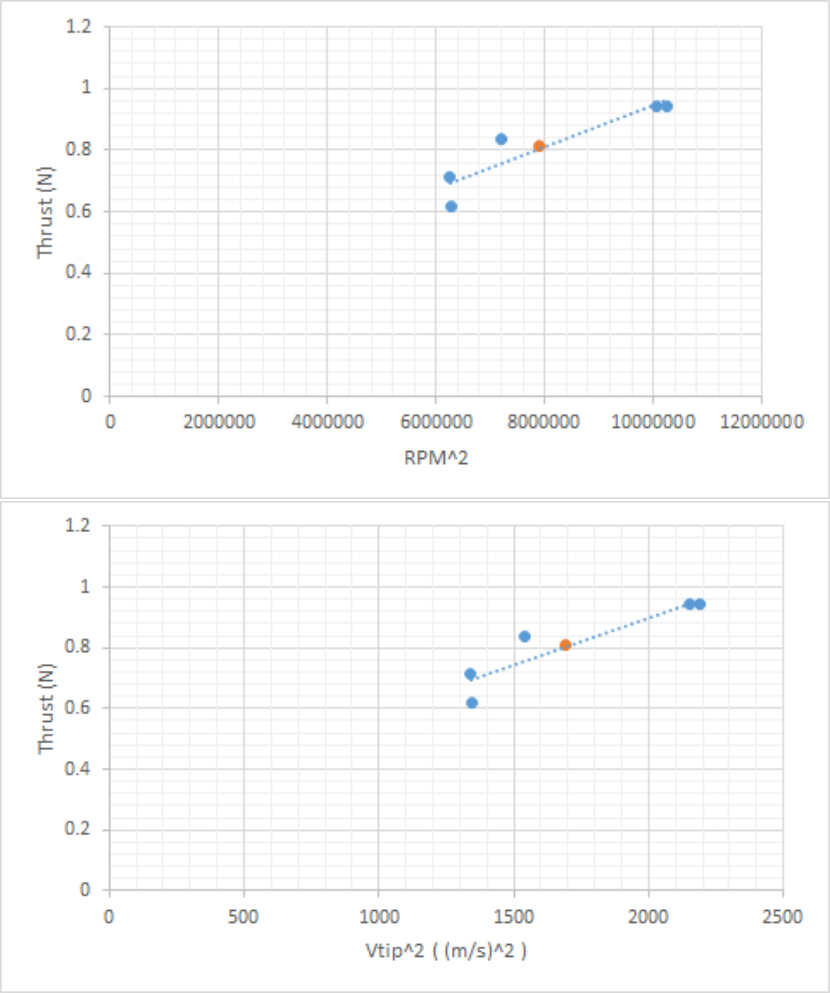

Figure 3.3: Thrust vs. RPM^2 graph based on thrust test of M3HS (top). Thrust vs. u_{tip}^2 graph based on thrust test of M3HS (bottom).

is scaled by the u_{tip} velocity which means that by keeping the C_T constant then the scaled u_h, that will now be refer to as u_H^*, can be related to the full size u_H as

$$u_H^* \simeq \frac{1}{3} u_H \tag{3.4}$$

Now, if we refer back to table 1.1, we see that the atmospheric density on Mars, ρ^M, is roughly 100 times the atmospheric density on Earth, ρ^E. There-

fore, assuming the following drag force (F_D) proportionality

$$F_D \sim \rho u_H^2 D^2 \tag{3.5}$$

[9] where D is dust particle diameter, then the drag force on Earth can be written as

$$F_D^E \sim \rho^E {u_H^*}^2 D^2 \sim \rho^E \frac{{u_H}^2}{3} D^2 \sim \frac{100}{9} \rho^M u_H^2 D^2 \sim 10 F_D^M \tag{3.6}$$

Therefore, we are overestimating the drag force by a factor of 10. Given we are using particles with roughly the same size and weight of the dust particles in Mars, the force the drag would have to beat is of the same magnitude, thus increasing the chances of creating saltation.

Chapter 4

Dust Test Cell Experiment

The Dust Test Cell Experiment included the design of an experimental setup that would allow us to visualize the dust cloud produced by the rotor of the scaled MHS model in Mars-like conditions.

4.1 Design of Experiment Test Section

The Dust Test Cell was designed thinking about the size and scale of the Mars Scout Model that would be tested inside and, the possible tests that could be done. The main objective of this cell is to enable a controlled environment to simulate the possible dust saltation due to the helicopter's coaxial rotor in Mars like conditions. Therefore, it was decided that the Cell had to be an enclosed area, in order to keep the dust from contaminating its surroundings, specially considering that future testing will take place inside a vacuum chamber in order to better emulate Mars conditions. The cell was made using a 91.76 $cm \times 102.55\ cm \times 120.33\ cm$ cardboard box (inner measurements). The bed section had to be large to reduce wall effects on our experiment. We chose the floor of the box to be larger than $2D \times 2D$ where D is the diameter of the rotor being used to ensure the wake of the rotor to be falling completely on the test section. However, since we were unsure at what point or if there would be dust saltation, this area had to be considerably larger to allow us to see the effect. Since both the half-scale and the third-scale models are to be tested, the box's dimensions were selected for the half-scale rotor. The test of the half-scale model will not be addressed on this thesis.

Moreover, it was important to make both the top of the box and the door of the cell transparent in order to see and record the experiments. These were to be filmed and photographed from different angles in order to later compare with simulations. The see-through sections are acrylic windows that are strong enough to resist impact from a broken rotor.

Lastly, the bottom part of the box had to have a wooden barrier to help keep the dust inside the box when it was open. This barrier further helped in the flattening process of the dust. The bottom of the box was also covered by a particle board, material designed to be very smooth with an even surface in order to ensure the flatness of of the sand was not altered by an uneven bottom surface (Figure 4.1).

The material used to simulate the dust on the Martian surface for this experiment was selected based on the research done by R. Greeley *et al.* [3]. They proposed that the best material to simulate the dust grains are crushed walnut shells due to their density and size. Both of these qualities help compensate for Earth's gravity and simulate the weight of the particles in Mars, at the same time it keeps the right ration between the atmospheric density and that of the particles. For purposes of this thesis, only particles of size 60 μm were selected since that is the size that proved to be, in their experiments, the most prone to saltation.

Three heights were selected to gather information about the interaction between the model and the dust. These heights are "wheels on ground", 15 cm drop, and $3R$, where R is the rotor radius. The first height, "wheels on ground", as the name suggest is the height at which the helicopter rotor when it is about to take off. This height is the closest to the ground and therefore it is believed to be the height at which it is most likely to see dust saltation. The second height, 15 cm, refers to the scaled version of that at which the full scale Mars Helicopter Scout (MHS) turns-off the rotor and lands. This height is of extreme importance given that the design of the helicopter has an altimeter that will determine when it has reached the 15 cm, measured from the "wheels" of the helicopter to the ground, and shut down to land softly. It is believed that if the helicopter is ever going to be in danger of brownout, it would be at this point given that it is both the moment of landing plus it experiences in-ground effects. Lastly, the third height will allow us to study saltation effects from a position outside ground-effects. Since the model that was used for this thesis was the 30% scale model of the full size MHS, these heights were scaled in order to see similar effects. Therefore, the heights used for these experiments, shown in Table 4.1, use

Figure 4.1: Test cell box. The fuselage inside the box is the half-scale model.

the half point between the two rotor disks of the model on the mast as their reference point.

Wheels on ground:	99 mm
15 cm drop:	147 mm
3R:	419.1 mm

Table 4.1: Heights used on both Tuft testing and Dust testing.

4.2 Methodology

After the dust test section box was built, it was time to place the dust inside of the box. The depth that was selected for this experiment was the width of the wooden guides on the side of the box, of 3/8 *in* or 9.525 *mm*. The method of "dusting" the inside of the box was of the highest importance. The dusting had to be done with extreme caution to avoid compacting the crush walnut-shells (CWS), while keeping the depth of the dust bed even. This was achieved by first kneeling inside the Test box placing the pail and the screed near you. By placing oneself in a comfortable and strategic location, one was able to place the CWS starting from the far back, forward. Then, the test bed was mentally divided into 4 strips parallel to the far wall. With the help of a plastic scoop, the CWS was generously spread out on the first strip. That is, the one furthest from the entrance (Figure 4.2). The amount recommended was approximately 3 scoops. It is better to put less CWS at a time than a lot. The screed was then used to flatten the CWS by gently pull it towards you, using the flattest side. One must make sure not to apply any downward force since this could alter the thickness of the layer at the same time that one would compact the CWS. It was important to keep the screed at a constant angle while moving it. Furthermore, the direction in which one moves the screed had to remain constant every time. Once the CWS was no longer being pushed, another scoop was grabbed to cover any holes that might exist in the previously flattened strip. This was repeated until there were no more holes on the sand. This process was repeated for the second strip and fourth as well. For the third strip, the procedure changed. Once one is done flattening the strip, there was a "mountain" of CWS in the middle. This was caused by the presence of the pedestal in the centre of the Test Box. In order to level this section the screed was used, always making sure that both ends were on the side guides, and it was rotated around the pedestal. This left an "X" shape pattern on the centre strip area. Therefore, the left and the right sides were flattened separately. One should never try to flatten all in one go.

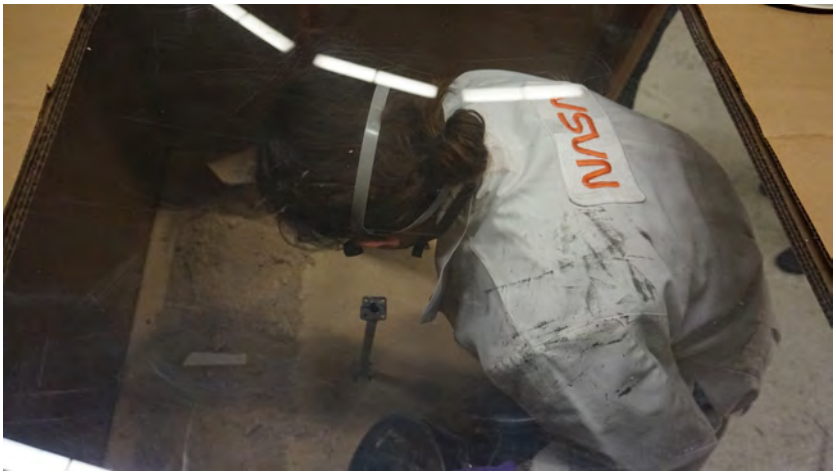

Figure 4.2: Placing crushed walnut shells inside dust test section box.

Once the dust bed was set, the MHS 30% scale model was placed on a mount that could be attached to the centre of the pedestal. Given that the sides of the model were exposed, it was decided to cover them with black tape in order to avoid the dust from getting in between the gears. The height at which the model was held was determined by the length of the mount that was attached to the pedestal. This height was measured not from the bottom of the test bed, but from the surface of the dust bed.

4.2.1 White Light Experiment

For lighting, a LED lamp was placed on the top part of the test cell in order to illuminate as much as possible the inside of the box. All experiments were done with the room lights turned on. It was realised that placing a lamp above was better than by the side window. The reason for this was that the reflection of the lamp on the window did not allow the camera to correctly capture the phenomenon. Moreover, the lamp was not placed directly above the model to avoid creating a shadow directly underneath. For this experiment, the camera used was that of an Iphone 6S, and was placed perpendicular to the MHS disk plane. The camera allowed us to film the experiment at a frame rate of 120 frames per second.

4.2.2 Laser Wall Experiment

These experiments where done in similar conditions to the white light testing. The material used in the bed of the box was CWS. However, the main difference between these two experiments falls in the lighting and the recording of the phenomenon. The lighting consisted on a 2 watts green laser, which was opened using a glass stirring rod in order to produce a "laser wall". The set-up for this experiment consisted on placing the laser outside the Dust Test Cell and by making a small hole on the side of the wall, perpendicular to the window, to allow the laser light through. This hole was sealed off using a thin and clean piece of acrylic. The initial plan was setting up the stirring rod outside the box using a metal stand hand clamp, as to not interfere with the airflow. However, given the size and shape of the mount, it was impossible to place the rod close enough to the wall of the dust test cell in order to lose the least amount of light as possible. Therefore, the mount had to be introduced into the box. The stirring rod was to be held parallel to the bottom of the box, i.e. horizontally and one had to ensure that the laser crossed through the centre of the rod. This made sure a vertical laser wall, that coincided with the rotor's axis (see Figure 4.3). Furthermore, the laser wall was placed perpendicular to the camera axis.

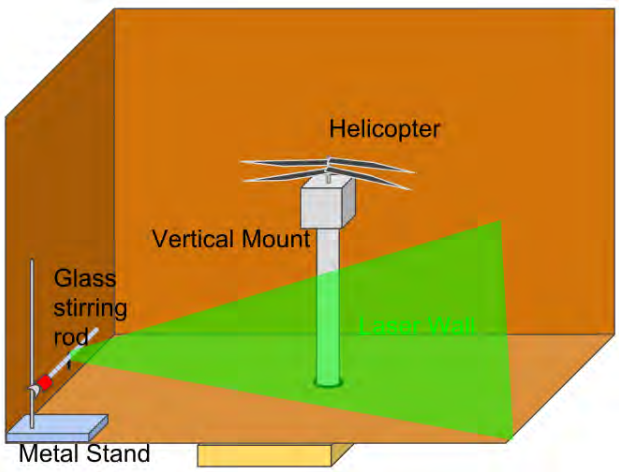

Figure 4.3: Diagram of the view inside the box with the helicopter illuminated with a laser wall.

Three videos were recorded, one for each of the heights, using a phantom camera Miro M 310. Every single time that the height of the model was

changed, one had to make sure that the focus of the camera matched the laser wall and the alignment of the laser was correct. In order to do so, calibration pictures were required. The first of the calibration pictures consisted on placing a set-square exactly where the laser plane, or focal plane, was. Since the length of the bright edge was know, the $pixel/mm$ ration could be calculated (see Figure 4.4). The second picture consisted on introducing a 30 cm ruler to the image and placing the 30 cm mark exactly at the centre of the helicopter-mount, in order to be able to locate the picture frame when comparing it to the simulations.

Figure 4.4: Calibration using a set-square whose bright side measures 152.35 mm.

Figure 4.5: Calibration used to measure the distance from the rotor to any given point in the image. In this picture, one can see part of the helicopter.

Moreover, the camera's frame rate was of 500 frames per second with an exposure time of 2000 μs. Given the lens size available and the distance at which the camera could be placed, outside the box, the area on the laser plane that was visualized was roughly of about 30 cm across by 20 cm tall. The videos were analysed using PIVlab in order to find the velocity field of the dust particles in saltation. The interrogation area was of 84 pixels with 42 pixel steps. Numerical simulations gave an estimate of the maximum speed (5 m/s) used to discriminate PIV disproportionate velocity data. These visualizations were done in the Hydrodynamics Laboratory of the Facultad de Ciencias, UNAM.

Chapter 5

Tuft Testing

In order to validate the RotCFD simulations, an experiment that could allow the visualization of the flow field had to be designed. When studying the flow field for normal earth aircrafts, a method commonly referred to as "Tuft testing" is used. The test consists on laying a grid of "tufts" on the most relevant and easily comparable planes. On rotorcraft theory, it is believed that the rotor wake has radial symmetry when there is no external body to alter this assumption. Therefore, the main planes of interest are those radial to the rotor shaft and that which is perpendicular to it, i.e. the ground plane. The testing methodology used to study the UH-60 helicopter brownout by Alan Wadcock *et al* in "Rotorcraft Downwash Flow Flield Study to understand the Aerodynamics of Helicopter Brownout"[2], was the base of the methodology used in this thesis. However, there were major factors that had to be accounted for that were cause of changes to the experimental setup.

The flow field experiments were done using the 30% scale model that was described in the previous section. Given the difference in scale between our 30% scale-MHS and the life scale UH-60, the size and material of the tufts had to be changed. To represent the air-flow movement it is important to make the tufts as small as possible. When studying the UH-60, given its size, normal pieces of string of 16.51 cm long were used. Our model is so small, that a tuft of that size would not align with the airflow. Thus, it was decided to go for the smallest tufts available, micro-fiberglass tufts. These tufts have a micrometric diameter, which is approximately a tenth of a human hair. They are hardly visible to the human eye when seen with visible light. However, when shone with a UV lamp, the florescent property

of the material increases its visibility to a millimetric diameter, allowing us to capture their movements with a camera.

There are several advantages to using a small scale model. One of those being that by using a much larger box compared to the model's size, it is possible to simulate free-flight without the model actually being outside. Furthermore, by having an enclosed test area, it was possible to reduce the airflow in the room and thus determine that the movement of the tufts was caused strictly by the wake of the rotor.

The tufts used were selected because of their micro-size and material. Their micro-metric diameter allowed them to be easily moved by the wake of the helicopter, at the same time, it made them the least invasive "visualizing particles". However, it is important to point out that although it is the "least invasive" solution, the tufts are still a lot heavier than the air that moves them. Furthermore, despite all the efforts done to make this the less intrusive as possible, one should always keep in mind that the board itself holding the tufts is very intrusive and thus alters the flow. Therefore, in order to improve the experiment one should remove the presence of the board and place the tufts in a less intrusive manner. An example of an improved technique would be to tie the tufts onto a wire wall, allowing to reduce the contact surface of the airflow with that holding the tufts.

An important limitation these tufts had was in fact their size. They were so thin that it made them very fragile and easy to break or bend. Furthermore, they would occasionally get stuck with the ruffles of the cardboard on which they where glued to. Not to mention the orientation they were originally glued to and gravity caused them to have a preferred orientation. Also, the presence of static electricity interfered with their freedom of movement. With the purpose of reducing this problem, the boards where rubbed using dryer sheets.

5.1 Experimental Setup

The experimental setup included black poster-boards of different sizes that were used to glue the tufts on. The poster board thickness, 1.27 cm, was selected by keeping in mind the need for the board to be as less intrusive as possible, at the same time it needed to be stiff in order to avoid the deformation of the board. The colour of the back is important, previous testing showed that the visualization of these tufts was improved by having

a dark background as opposed to a light-bright background. Three different sized boards were made, two vertical test boards and one ground board. The two vertical ones where used to include the three selected heights when studying the radial planes. The dimensions of the largest one of the two, from now on referred to as the Vertical Big Board (VBB), were 28 $cm \times$ 0.4 $cm \times 40.6$ cm, while the Vertical Small Board (VSB) was only 28 $cm \times$ 0.4 $cm \times 7.6$ cm.

Both vertical boards had an angle of inclination of 1.75° from the vertical position. The reason for this was to prevent the air flow from being affected by the edge of the board while trying to maintain the board as vertical as possible. The VBB had 42 vertical rows and 66 horizontal rows giving a total number of 2772 tufts. Meanwhile, the VSB had a total number of 132 tufts. Both boards had borders and separation between rows of 0.64 cm. The ground board was a 91.44 cm square with 71 rows of tufts. Each tuft row ran all across the board and had a separation of 0.64 cm. The total number of tufts on the ground plane was 5041.

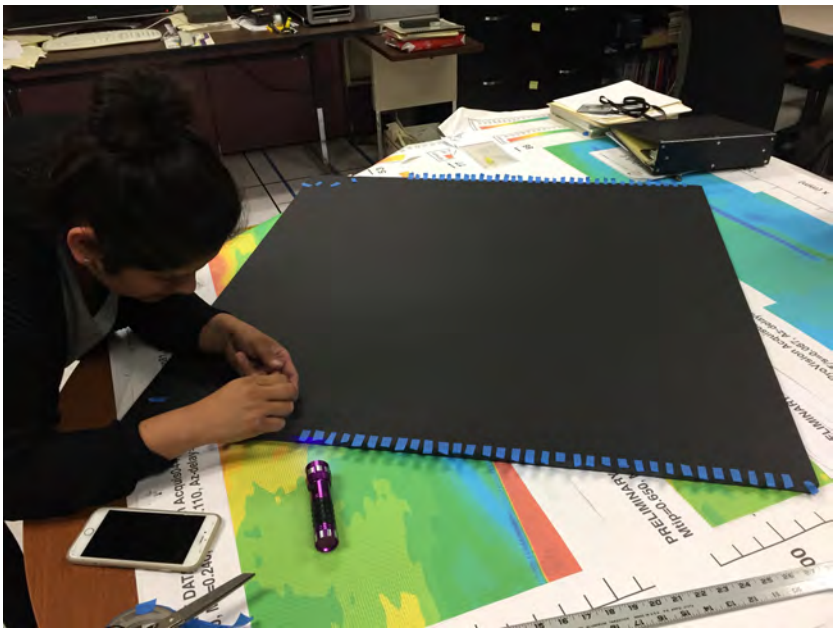

Figure 5.1: Tufting the ground board.

In order to make the boards it was important to indicate accurately where the string of tufts would be placed. This allows to ensure that they are all

evenly spaced and parallel to each other. Additionally, by also drawing lines perpendicular to the tuft rows, it was clear where one was to put the non-reflecting glue. This was done in order to secure the tuft after cutting the roll of material. The tufts were not to be touched in order to avoid static electricity or anything that could cause the tuft to stick on the board. All this was done with the help of a hand-held UV-lamp that was not bright enough to cause eye problems, but facilitated the visualization of the tufts.

The design of the mount represented a challenge on itself. Given the ground floor testing, the model had to be held horizontally since it could not be held down to the board. That is why it was decided that for this test, the model had to be held by a "sting-mount". A sting mount consists on a strong vertical base that has a "sting" held on to it at a 90° angle to which the model is attached to (Figure 5.2). It was paramount to keep the diameter of the tube holding the 3D model as small as possible to be the least invasive as possible, without compromising the stability and stiffness of the mount. For these tests, the base of the mount was magnetic, so to make it a stronger base if placed over a stiff metal surface. The 3D printed version of the model was modified in order to be attached to both the tuft testing sting-mount and the dust testing vertical mount.

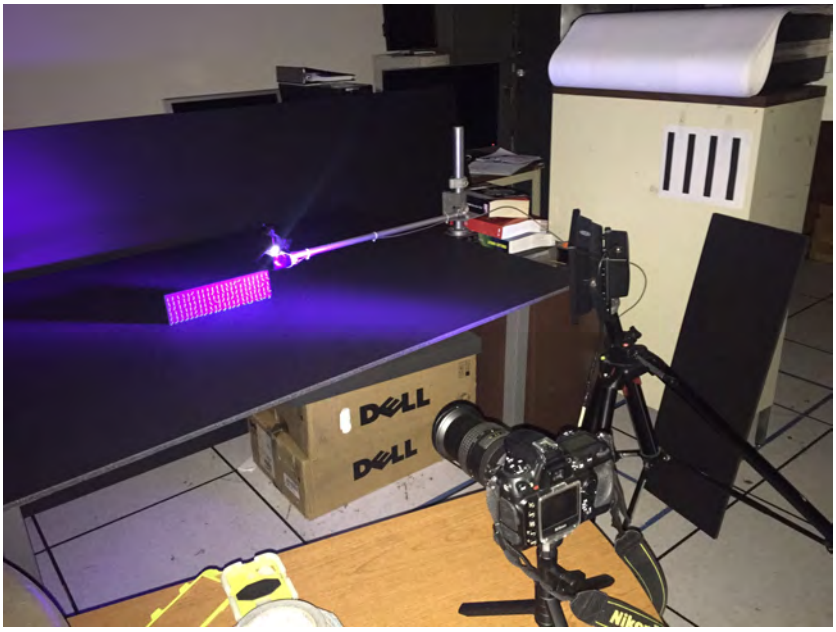

Figure 5.2: Example of a Tuft Test Experimental setup.

5.2 Methodology

The Tuft Experiment consisted on short runs of 30 seconds each in which the 30% scale model was turned on and both video and photographs were taken. Three boards were placed in different positions from the model each time, in order to visualize the phenomenon as well as possible. Analogous to the Dust Testing, the same three heights were selected for these experiments. However, this study was taken one step further by including planes with different inclinations with respect to the plane of the rotor. These angles ranged from 0° to 30° with an increase of 5° each time. By combining both the heights and the angles selected, we obtain a total number of 18 possible configurations. Nonetheless, the total number of runs needed are a lot more, approximately 54, since for each configuration we wanted to get at least three different shots. The variety in geometries of the tuft boards allowed for the visualization of the air flow underneath and next to the rotor and fuselage, from views parallel and perpendicular to the rotor plane.

To observe the phenomenon, both pictures and videos were taken. Two cameras were used in this experiment, one for the recollection of data and the other to record a video that would facilitate the comparison. A professional camera was placed as perpendicular to the tuft plane as possible. Yet, this was not always the case since it was not always the most convenient set-up. Since a large UV lamp was used to illuminate the entire board, placing the camera directly in front of the board would usually result in an over saturation of several pixels in the image due to the lamp's reflection on the smooth black board. Furthermore, the body of the model was cover with black tape in order to avoid having a bright reflecting white body. This also helped keep the aerodynamics of the body as close to the original MHS shape as possible. Given the lighting conditions were controlled and kept constant, the camera settings for all pictures were the same. These settings are shown on table 5.1.

Exposure time:	2 sec.
f (Aperture):	16
ISO sensitivity:	1,600
Frame rate:	1 frame/5 sec.

Table 5.1: Camera settings for all Tuft Testing Experiments.

Notice the long exposure time, the reason for such exposure time is to

capture the motion-cone of each individual tuft 5.3. Thus, making it possible to see the region in which each tuft moved in the given time lapse. The ISO and aperture were selected by consulting the department's photography expert and corroborated via trial and error, to optimise the amount of light entering the camera in order to avoid the over saturation of pixels while maximizing the recollection of information.

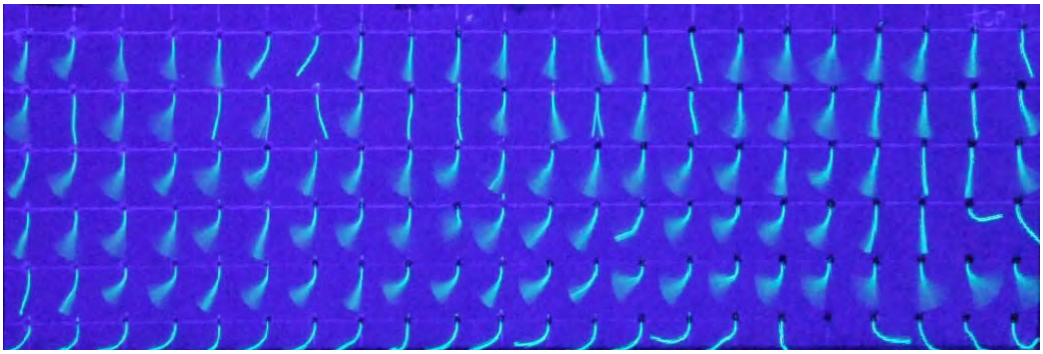

Figure 5.3: Close up of a sample tuft board in which tuft coning can be seen.

On the other hand, the camera used to make the videos was the one on an Iphone 6S. The video was used to accurately record when the camera started taking pictures with respect to the moment in which the model was turned on. This is used when comparing experimental results with simulations.

The experiments were done in an enclosed environment: a room, with no wind currents, low humidity and protection from external contamination by limiting the access to this room. Before setting the tuft board in position, it is imperative to wipe the board with anti-static cloth so to decrease the static electricity. This must be done with extreme caution to avoid damaging the tufts.

Chapter 6

CFD Flow Field Simulations

The Computational Fluid Dynamics' simulations were done using the program RotCFD. However, In order to start the simulations, several steps had to be taken beforehand. These steps will be referred to as the pre-simulations steps. Amongst these are: 3D scanning and processing of the model's blades; creation of the airfoil tables and their implementation into RotCFD.

6.1 Blade Scanning and Post-Processing

In order to get the correct geometry of the blades into the simulation, they were first 3D scanned. A "Metrascan 3D" handheld laser scanner, produced by "Creaform" was used to do the 3D scanning [19].

The scanner produces a CAD file from which the geometry of the blade can be extracted (Figure 6.1). Two scanning methods were tested. The first one was a target based scan. As the name implies, this scanning method relies on target stickers that are placed around the blade in order to calibrate the scanner. However, a down side to this method is that, in order for it to work properly, the blade cannot move. Given the size and weight of the blade, this made it very difficult since we could not find a non-invasive way of securing it in such a way that it would no be affected by external vibrations. Therefore, a second method was utilized for the scanning. This second method does not require placing targets on the blade, but instead uses the targets that were already on the hand-held scanner to triangulate the position. This was the method of choice, although it introduced some errors since we couldn't avoid partially blocking the signal with our bodies while scanning.

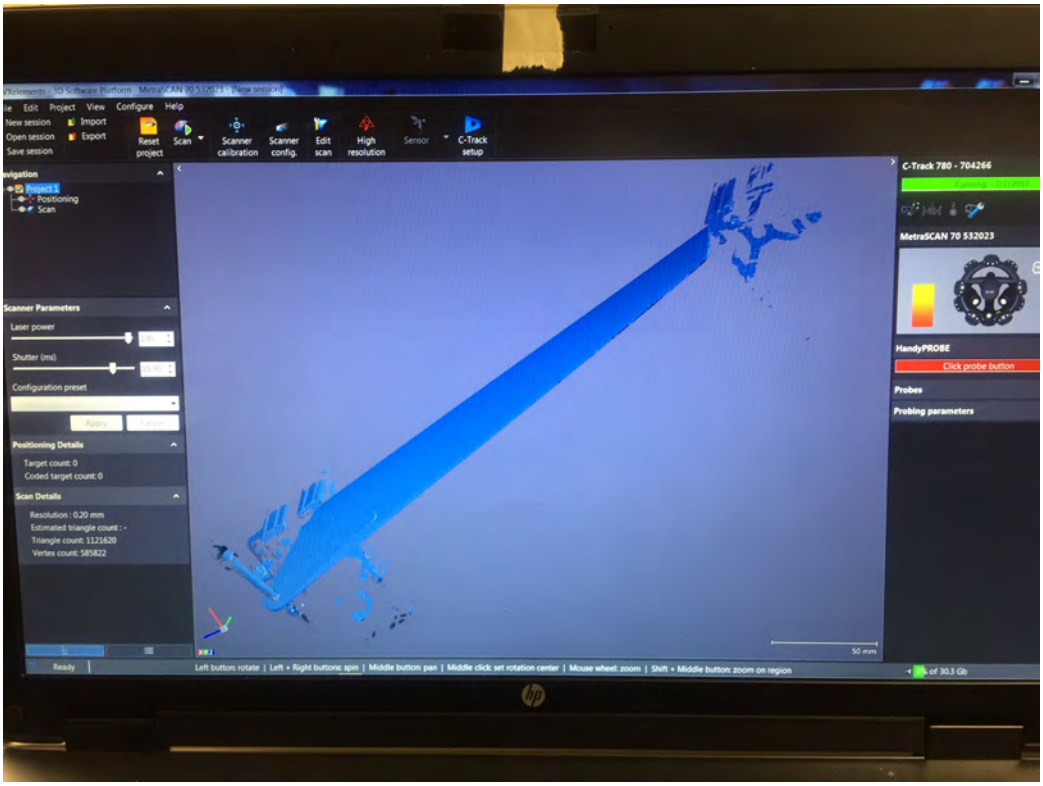

Figure 6.1: Screenshot of the Blade scanned. The blade is the blue smooth figure in the centre. The blue shapes that surround the blade are partial scans of the objects that surround it while it was being scanned. These were all removed during the cleaning process.

Once the laser scanning was done, the CAD file produced was analysed using the 3D CAD modelling software package named "Rhino". This tool allows for the "cleaning" of the blades scan. This refers to the creation of points that "fill up" for the areas of the blades that were not correctly scanned. This was done visually by the person in charge of the post-processing stage at NASA Ames, Eduardo Solis. Once all gaps are filled and the surface of the blades are smooth a point cloud is produced (see figure 6.2). Out of this point cloud, 20 cross-sections are selected and exported into text files that are then used to create the airfoil tables.

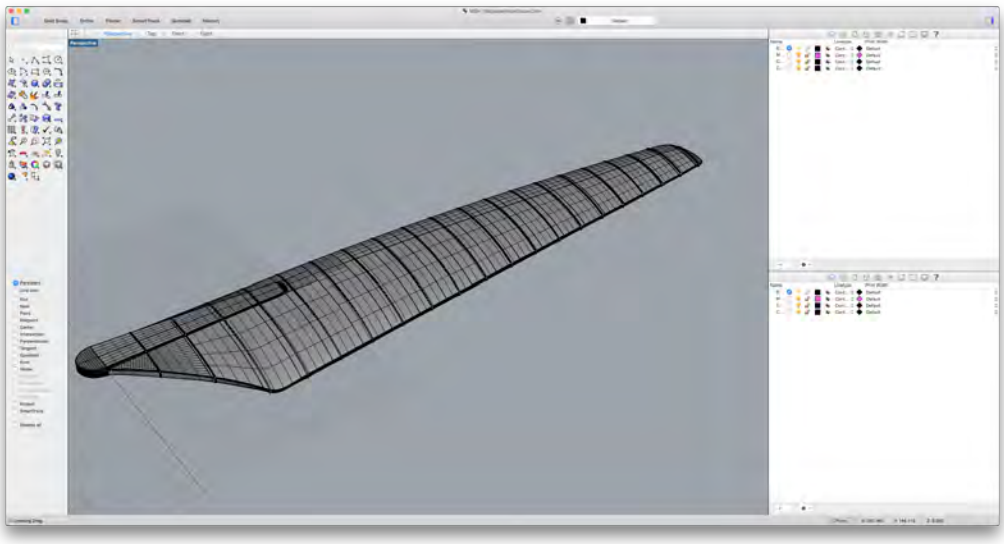

Figure 6.2: Screenshot of Rhino software used to smooth the CAD file of the scanned blade.

6.2 Airfoil Table Creation

The text-files containing the 20 cross-sections were then input into an already existing Matlab code written by Carl Russell designed to plot the cross sections from the text-file. With this, each individual cross-section was graphed and placed next to each other (Figure 6.3). It was decided that five cross-sections represented the different geometries, given the simplicity of our toy helicopter blade design.

As was previously explained in the theory chapter of this thesis section 2.2, Airfoil Tables are of extreme importance since they determine how the air interacts with the rotor blades at different angles of attack. Therefore, obtaining accurate airfoil tables was a high priority. That is why it was decided to use the program "Xfoil", a program designed by MIT to produce airfoil tables, instead of the more commonly used "C81 gen".

6.3 Blades and Body Geometry

RotCFD allows for user to introduce the specific geometry of the rotor blades by allowing the specifications of different parameters such as: radius, chord,

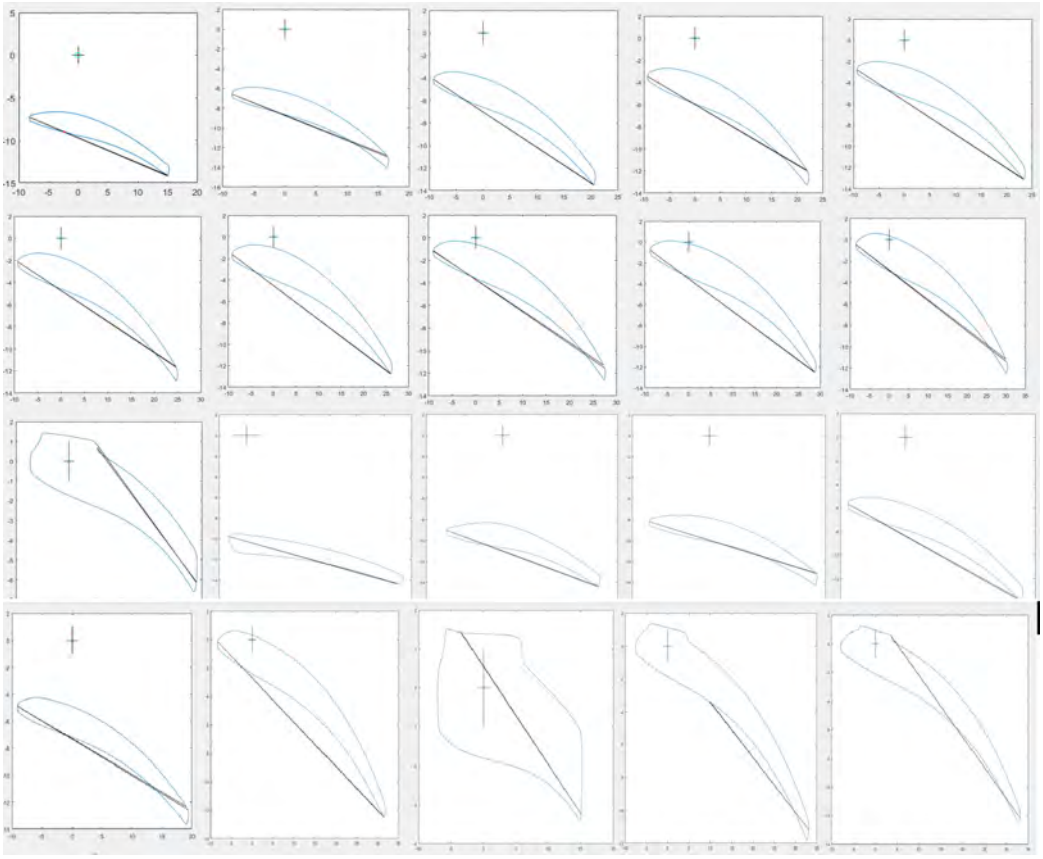

Figure 6.3: All cross-sections available. The top left corner is the rotor tip, while the bottom right corner is the part of the blade that is attached to the rotor mast. They are all different shapes since the blade design and its twists have to be extrapolated from these cross sections. The flat edges that can be identified in the last couple of cross-sections is the part from which the blade is held to the mast.

twist, number of blades and cutout radius. All this information is extracted from the point cloud and exported into a text file produced by the same Matlab script as that of the airfoil tables. This text file exports the Chord and Twist value at specific r/R where r is the radial position from the center of the rotor and R is the full radius of the blade. It is important to note that RotCFD requires consistency in the units that are used in its simulations. By graphing chord $/R$ vs r/R (Figure 6.5), we create a dimensionless plot

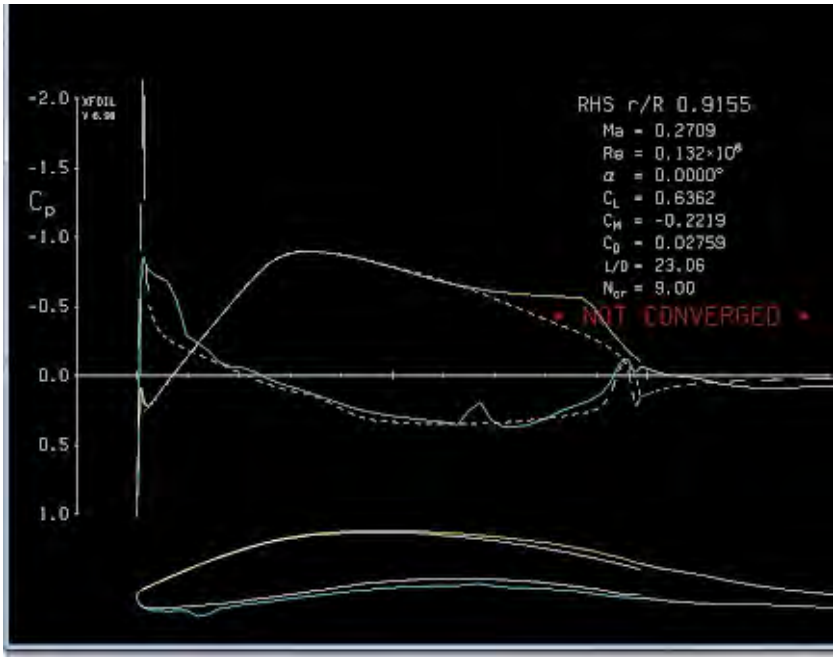

Figure 6.4: Sample Airfoil table. On top right hand side is the list of variables the table provides for each angle of attack.

that allows us to see the smoothness of our blade. The interaction of each blade and the fluid surrounding it is being extrapolated from only 3 airfoil tables. Therefore, the smoother the line is, the better this approximation is. The smoothness would indicate that the blade does not have bizarre changes between the positions of the airfoil tables, that may not be correctly simulated.

On the other hand, the twist of the blade is used to optimise the efficiency in hover. When graphing twist angle vs r/R (Figure 6.6), we see a smooth curve that peaks at roughly 0.3 r/R and then decreases the further away one is to the mast.

Moreover, it is also possible to determine how the rotor blades are positioned and moving by altering the following factors: cone angle, collective pitch, hinge offset, cyclic pitch, and flapping. Given that the model selected for the experiment was built from an off-the-shelf RC helicopter, all of the previously mentioned values are fixed by the manufacturing company and were all zero.

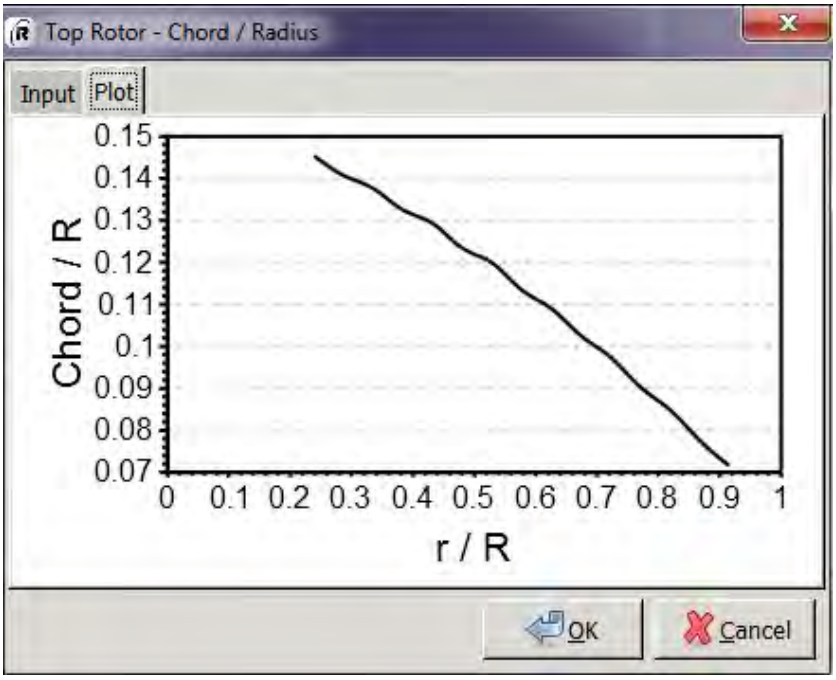

Figure 6.5: Chord/R vs r/R graph used to produce the shape of the blade. The data points had to be manually entered from the text file produced by the Matlab program to RotCFD.

6.4 Methodology

The simulations were done using a program that is currently being developed at Surka Helitek, Inc named "RotCFD". This program specializes in the fluid dynamics that surround rotating objects such as the rotors of a vertical lift vehicle. The main purpose of these simulations was to obtain the maximum velocity values for each height and inclination. In order to correctly represent the real experiments, we have to input the same initial conditions of the system, which are as follows. The flight conditions shown in the table 6.1, describe a rotor that is not moving relatively to the airflow.

The flow properties (table 6.2) describe the type of atmosphere that surrounds the rotor.

Moreover, these are the values necessary to calculate the Reynolds number and set a unit system, in this thesis we shall use metric units. Lastly, the wall properties help determine whether the rotor is completely isolated or if there

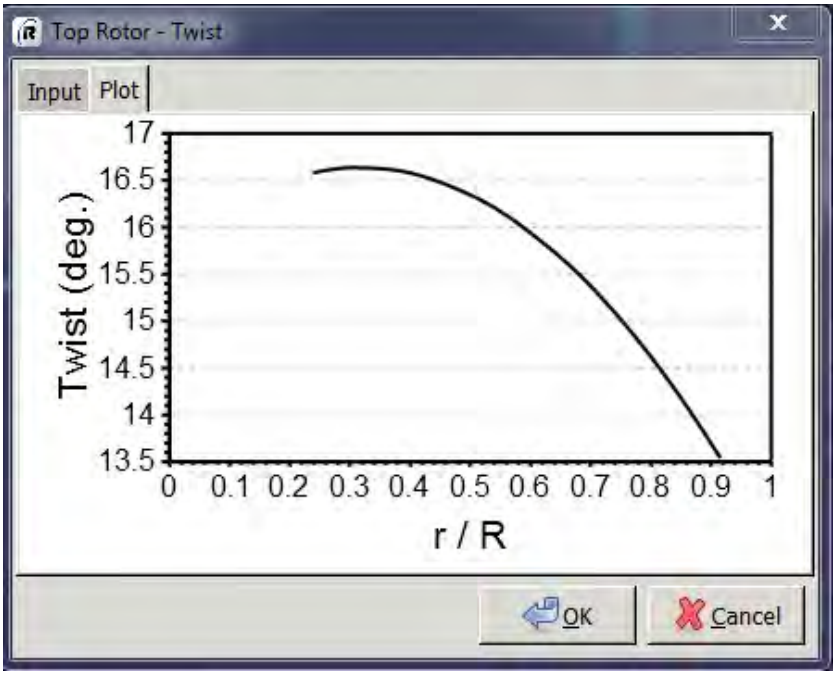

Figure 6.6: Twist vs r/R graph used to produce the shape of the blade. The data points had to be manually entered from the text file produced by the Matlab program to RotCFD.

Flight Condition Type	General	
Free Stream Velocity	0.0000	x
	0.0000	y
	0.0000	z

Table 6.1: Flight conditions for all simulations.

is a "wall" to consider (table 6.3). For these simulations, a non-slip condition was placed on the floor while keeping the other walls at atmospheric pressure and far away, 5D each side, to make them "invisible" to the rotor.

Additionally, the rotor configuration for the simulations had to match that of the real helicopter used for the experiments. Thus, once the geometry of each blade was scanned and introduced, the rotor properties where as shown on figure 6.7. The two blades and the radius are both part of the full size requirements and the scaling down. Meanwhile, the rotor tip speed was determined by the manufacturing company of the motors used to rotate the

Static Density:	1.225
Static Temperature:	288.16
Gas constant:	287.05
Specific Heat Ratio:	1.4
Dynamic Viscosity:	$1.75E-005$
Static Pressure:	101325.0
Calculate Viscosity [Standar Units]	
Calculate Viscosity [Standar Units]	

Table 6.2: Flight properties of all simulations

X-Min type	Static Pressure
X-Min Pressure	101325.0
X-Max type	Static Pressure
X-Max Pressure	101325.0
Y-Min type	Static Pressure
Y-Min Pressure	101325.0
Y-Max type	Static Pressure
Y-Max Pressure	101325.0
Z-Min type	Viscous Wall
Z-Max type	Static Pressure
Z-Max Pressure	101325.0

Table 6.3: Wall properties of all simulations

rotors. However, as previously mentioned in the 30% model design chapter, it is consistent with the tip speed required. It is also important to point out that the rotation of one of the rotor disks was opposite to that of the other rotor.

6.4.1 Grid Production and Time Step Selection

The Grid selection was designed as to maximize the number of cells surrounding the area of interest. The number of cells was limited to the memory availability on the graphics processor available. For this thesis all simulations were done using a Tesla C2070 Nvidia Graphics Card with a total memory of 5376 MB. Each simulation had the external boundary, which contained the

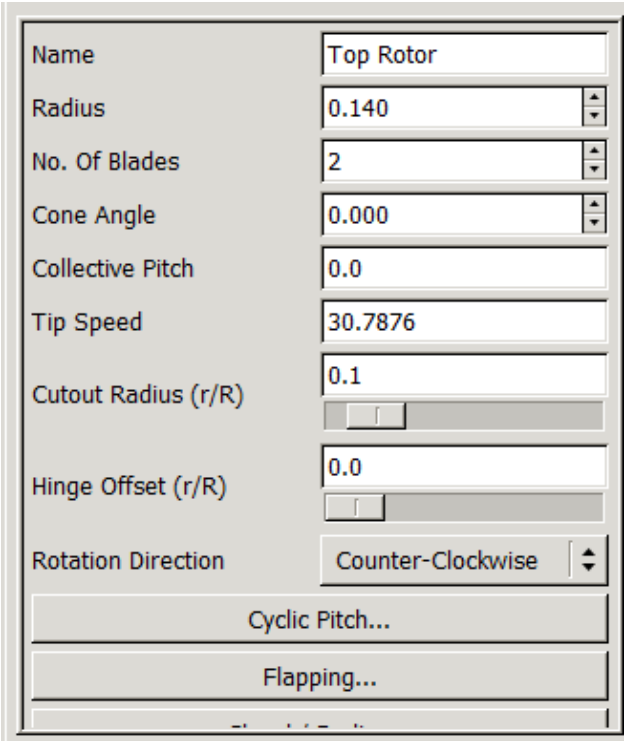

Figure 6.7: Rotor Properties used for all simulations .

information about the helicopters surroundings, and two refinement boxes. The refinement boxes did not input any additional information, they were strictly design to increase the density of cells, and resolution, in the areas of interest.

Figures 6.8a and 6.8b illustrate the grid density at different points of the simulations. It is important to point out that the grid was not "fitted to body" as it generally is. The reason for this was that given the cubed nature of the fuselage, it was not necessary to do so and the grid calculations were less likely to diverge if this was the case. The second refinement box, illustrated in both figures as the white line closest to the body, was selected in order to have a denser grid near the areas of interest, i.e. where the boards were placed on the real experiments.

On the other hand, the Time Step selection was directly related to the rotating speed of the MHS scaled model of 2500 RPM. This was measured experimentally using a hand-held digital Tachometer by placing a reflective

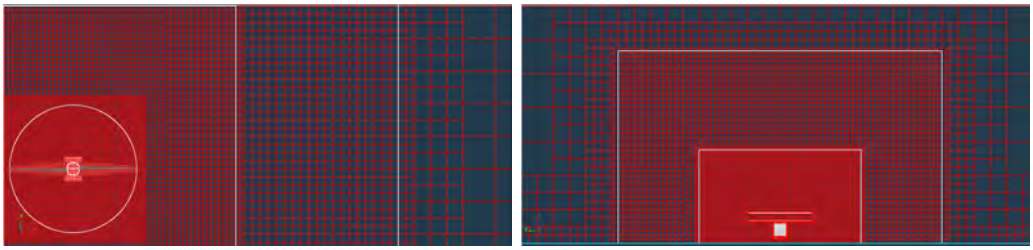

(a) Horizontal plane. (b) Vertical plane.

Figure 6.8: Grid visualization of both planes where the outer white line represents the first refinement box while the inner white line is the second refinement box.

sticker on the tip of one of the blades and holding the tachometer in a set position, perpendicular to and directly above the reflective sticker. The experiment was done whilst it was being held still to avoid the helicopter from flying and moving. The Courant-Friedrich-Lewy condition (CFL) is a necessary, although not sufficient, condition for the numerical scheme used to solve the partial differential equation will be stable [20]. The CFL condition states

$$\frac{u\Delta t}{\Delta x} \leq C_{max}, \tag{6.1}$$

where u is the characteristic velocity of the phenomena, and Δt and Δx are the minimum time and distance steps respectively. C_{max} is the maximum Courant number which, given we are using a fully implicit scheme, is 1. Therefore, if we make $u = u_{tip}$ then the simulations time step is selected to be the time it took for one of the rotor blades to move 1°, which was: 6.667×10^{-5} s. This time step was selected in order to give enough time for the rotor to move enough in order to have a different result from the previous step, without losing too much information of what happened in between. Furthermore, this time step was the smallest time step that would not increase the total simulation real time past four days. This led to the following time settings shown in figure 6.9.

Figure 6.9 shows the time grid for all simulations. It also points out the selection of the "time scheme", in this case fully implicit, that is related to the time discretization method used by the program. The total time simulated was of 1 second. This was primarily limited by the computation time available. It is important to keep in mind that thanks to the CFL

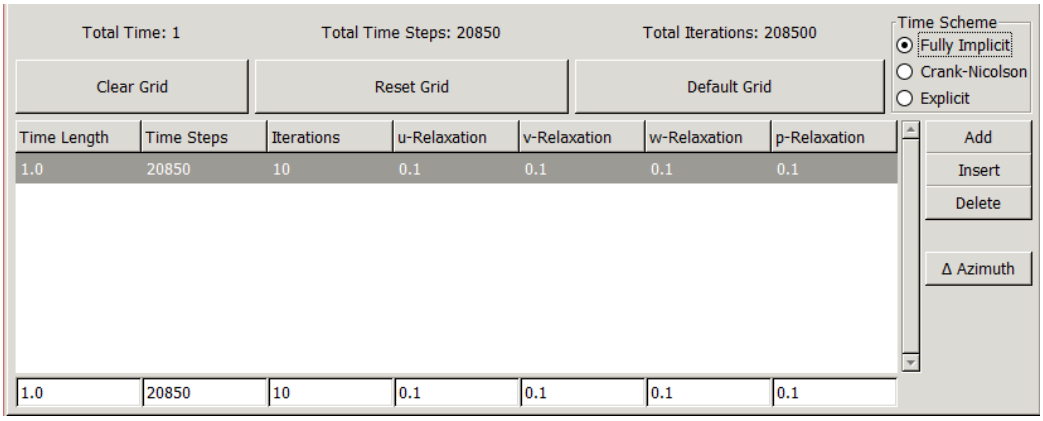

Figure 6.9: Time step setting for all simulations.

condition, the minimum grid cube length was now restricted.

Chapter 7

Flow field, Dust and Tuft Testing Results

Interesting results can be extracted from each individual test and simulations. Furthermore, there is much to gain from the comparison between the three.

7.1 Dust Testing Results

The results of the white light experiment are qualitative results. By selecting frames from the videos, we can appreciate that some dust particles are being moved. An example of this is shown in figure 7.1(bottom), the first frame at which CWS saltation is observed (wheels on ground). Figure 7.1(top) is the pixel difference between two frames, the frame where saltation is first observed minus the initial frame (no saltation).

However, it is important to point out that the dust cloud that was created appeared to have a very low density. This can be seen in figure 7.2, 0.34 s after saltation started, where the bottom image is a picture of the dust cloud at its maximum, which is hard to capture with the camera. The top image is the difference between an image of the test bed before the helicopter model was turned on and that of the test bed 0.7 s after it was turned on. This was done in order to visualize better the results since the white dots are the CWS cloud generated. Given that the tests were done in optimal conditions for saltation, we can thus conclude that the helicopter, which will be exposed to less than ideal conditions during its flight, will not create a dense enough cloud to pose an obstruction problem to the altimeter (brownout).

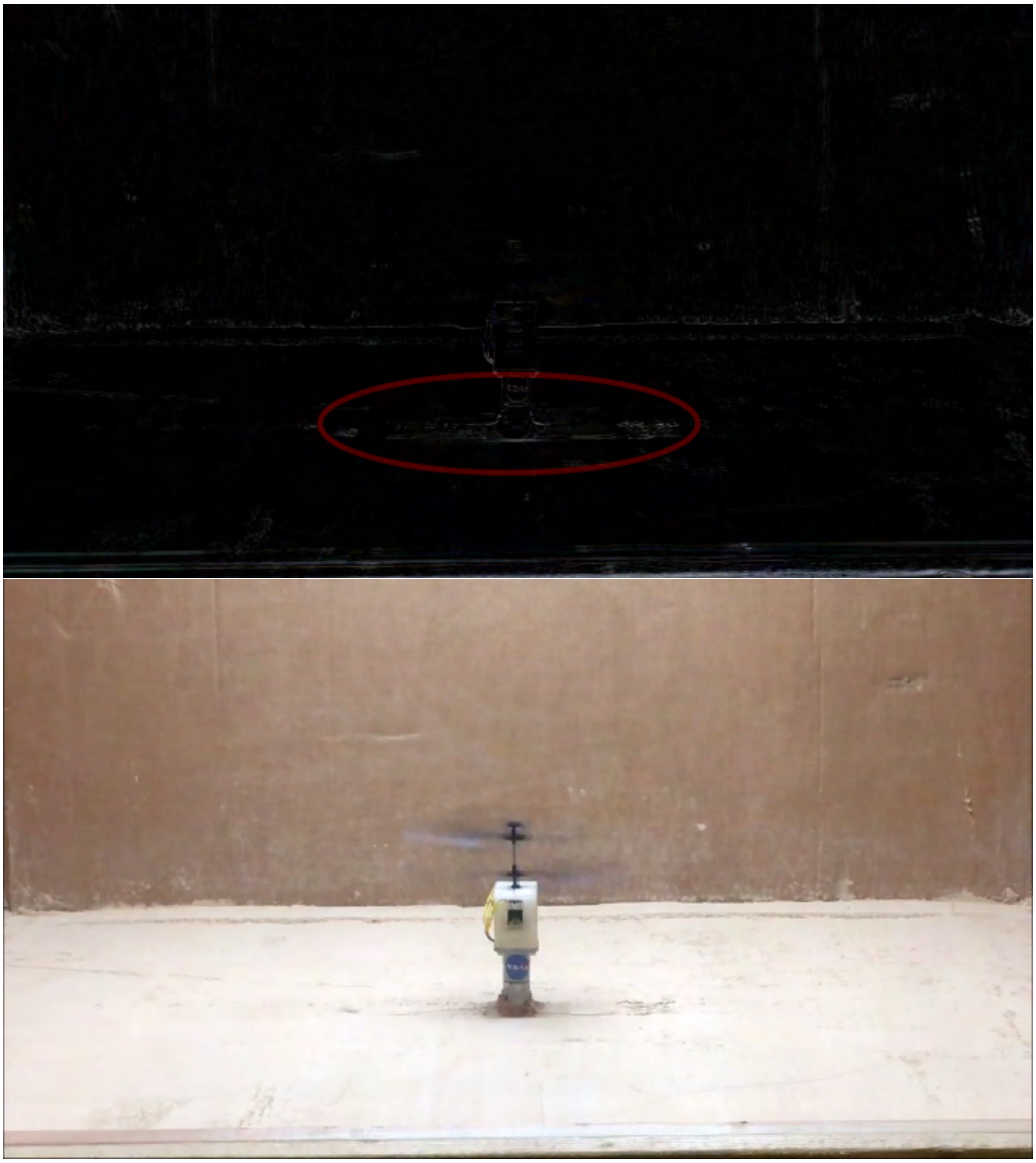

Figure 7.1: Difference between a frame with no CWS movement and that of the first frame where there is movement(0.36 s since helicopter was turned on)(top).1^{st} Still frame of CWS in saltation (bottom).

From the laser wall experiments, we see that the distance at which saltation occurs is less than the distance at which, according to the simulations

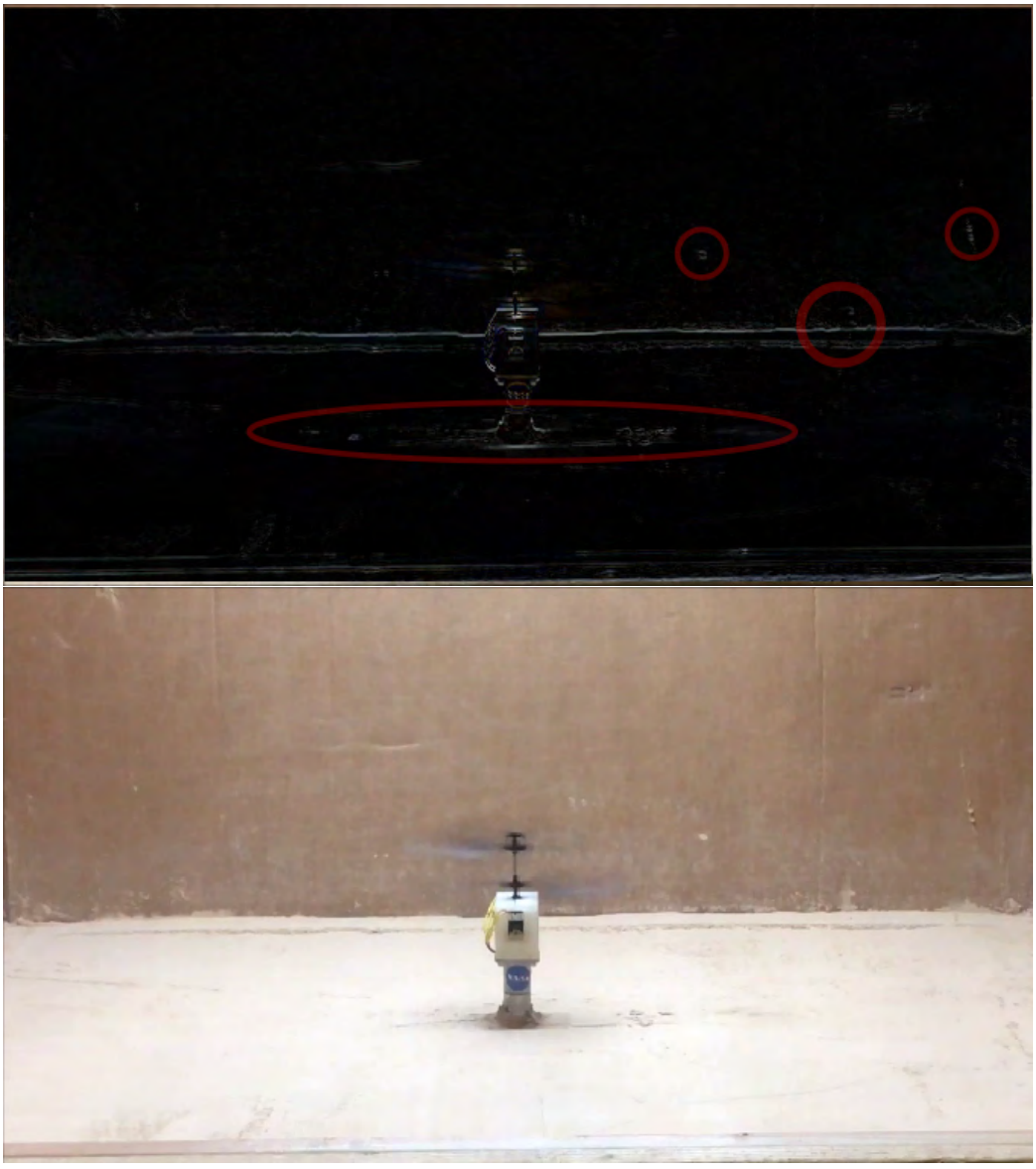

Figure 7.2: Difference between a frame with no CWS movement and that of the eleventh frame where there is movement(0.70 s since helicopter was turned on)(top).11^{th} Still frame of CWS in saltation (bottom).

that will appear later in the text, the maximum wake speed is reached.

The result of both of these experiments can be better appreciated in the

videos in the attached CD. On The white light videos help see the density of the dust cloud. Meanwhile, the laser wall videos contain the PIV results where one can better identify the presence of a vortex at ground level. Thus, it may be concluded that it is not necessary to reach such high speeds in order to induce saltation. This is in agreement with the theory since, as was mentioned in the introduction, the speed necessary to induce saltation is much less. To see all the dust testing images see appendix A.

7.2 Tuft Testing Results

The results from these tests are presented with a single photograph for each configuration, i.e. height and plane inclination. Each picture has an exposure time of 2 seconds, thus showing some degree of tuft coning, were coning is the production of a cone-like shape caused by the movement of the tuft around a point centre. The pictures selected were all taken in the first 2 seconds of the experiment. This was done to compare the images to the simulations.

It is important to point out that the tuft experiment snapshot showing the horizontal plane (such as Figure 7.3, etc.) have been dewarped in order to have an image as if the camera were directly above it. Placing the camera directly above was not a feasible solution since the body of the helicopter would "block" the area of interest for this study: that directly under the rotor. The helicopter was not always placed directly in the centre of the board, causing the airflow pattern to shift from the centre to the board to the top of the picture, as is the case of figure 7.3.

Due to time constraints, the only angle of inclination tested for heights 15 cm and $3R$, apart from zero, was 30°. To see all the tuft testing results go to appendix B.

7.3 Simulation Results

The results of the simulations are shown with a single still image of when the simulation was at exactly 1 second. The colour scales in the bottom right corner of every picture illustrates the velocity magnitude. The white squares that are next to or under the rotor represent the location at which the boards on the tuft experiments where. This was done in order to facilitate the comparison. Moreover, some of the vectors on the images are white, this

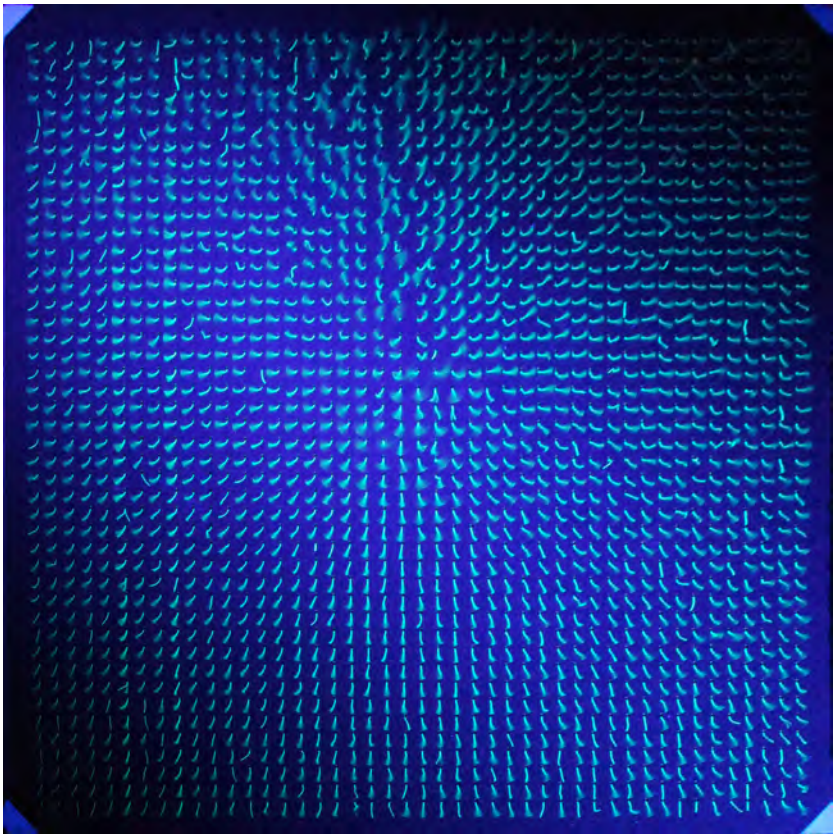

Figure 7.3: Ground Board

Figure 7.4: Tuft pattern visualization of the horizontal board with height "wheels on ground" and plane inclination zero. On this picture, the airflow pattern has slight shifted to the top of the picture because the helicopter was not placed exactly in the centre but instead more to the towards the top.

means that they are exceeding the maximum value shown on scale. The scale was selected for each individual picture in order to gather the most detailed information of the area of interest.

A main distinction between the images presented for all angles of height "15 cm drop" and $3R$, and those of height "wheels on ground" are the lack of tuft tests to compare these sections. To see all the simulation results go to appendix C .

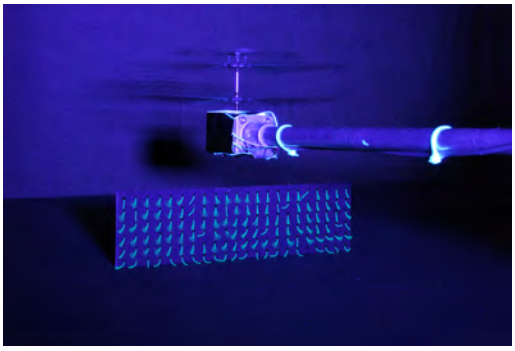

(a) Vertical Small Board

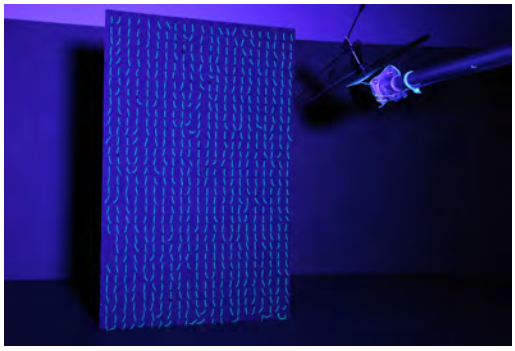

(b) Vertical Big Board (inclination)

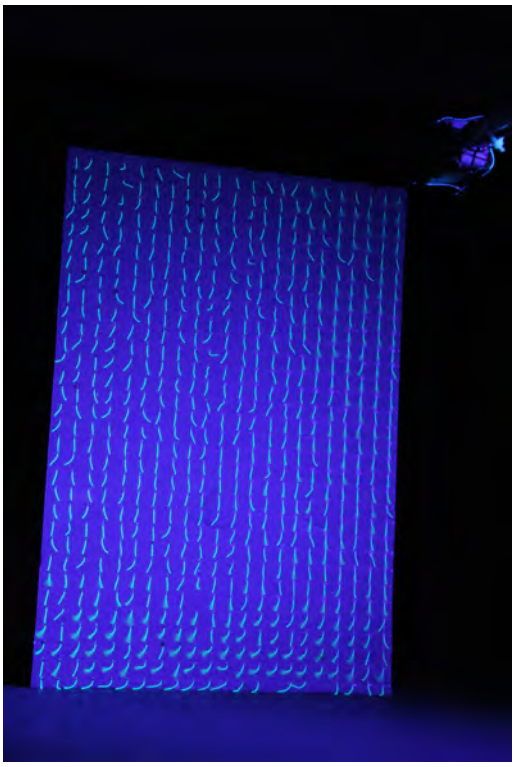

(c) Vertical Board (no-inclination)

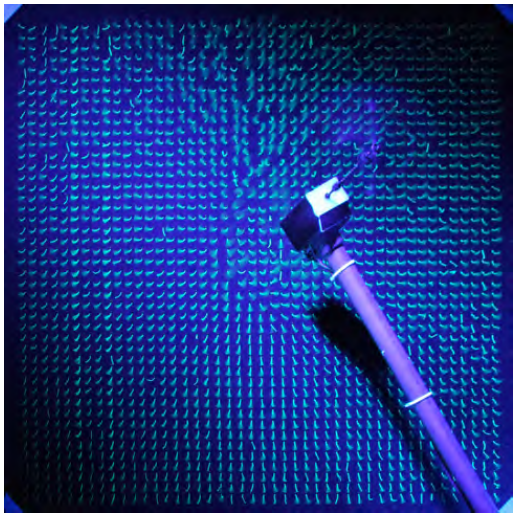

(d) Ground Board

Figure 7.5: Examples of tuft pattern visualization of the vertical and horizontal boards with height for different heights and inclinations.

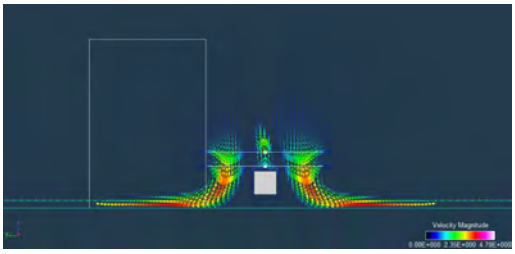

(a) Vertical Big Board

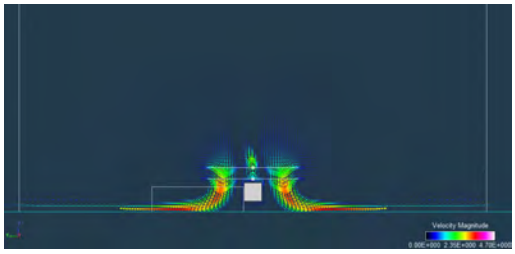

(b) Vertical Small Board

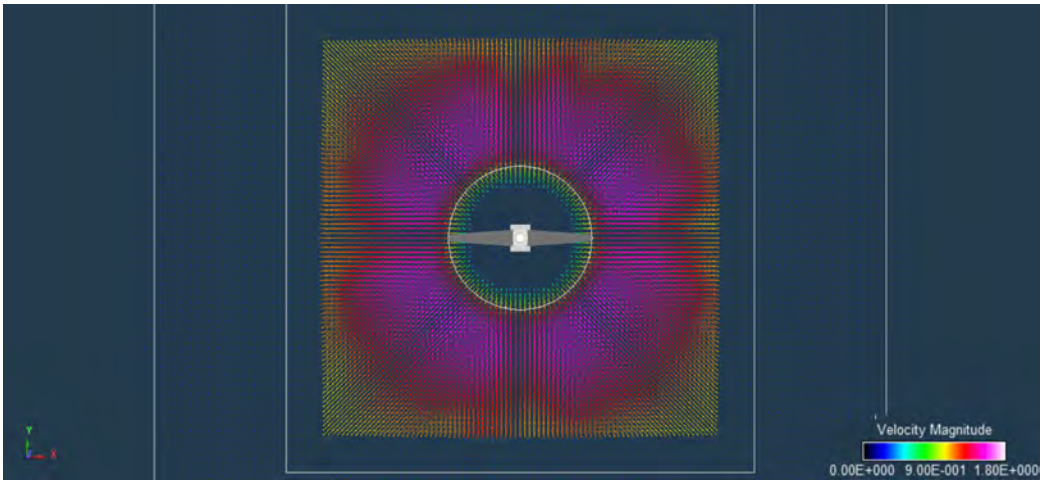

(c) Ground Board

Figure 7.6: Example of the flow field visualization taken from the simulation with height "wheels on ground" and plane inclination zero.

7.4 Comparison

When comparing the results from the simulations and the tuft testing we see a good resemblance between them, what we mean by this is that the direction suggested by the simulation falls somewhat comfortably inside of the tuft conning (Figure 7.7, 7.8 and 7.9). However, one should not overlook the obvious discrepancies between the simulation of the experimental results. As previously mentioned, the centre of the airflow is slightly shifted because the helicopter was not placed perfectly in the centre. It is also possible to see how the rotor wake becomes thinner, the further away you get from the rotor. This last statement is mostly noticeable for the $3R$ height (Figure 7.9).

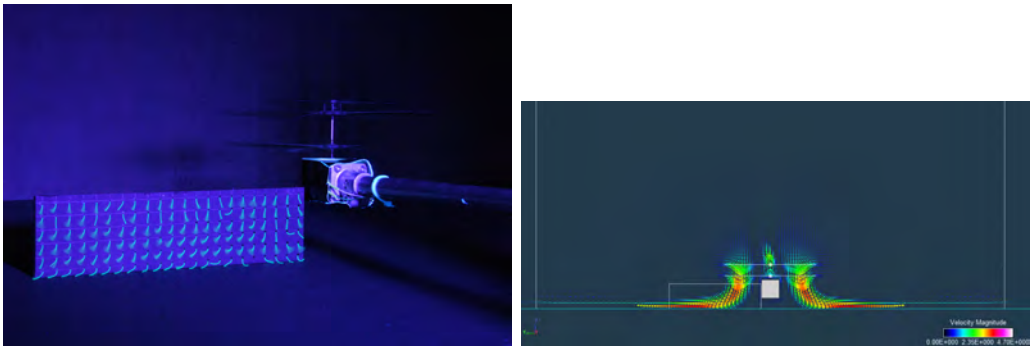

Figure 7.7: Flow field visualization of vertical plane with height "wheels on ground" and plane inclination zero(right).Tuft pattern visualization of vertical plane, under the rotor, with height "wheels on ground" and plane inclination zero(left).

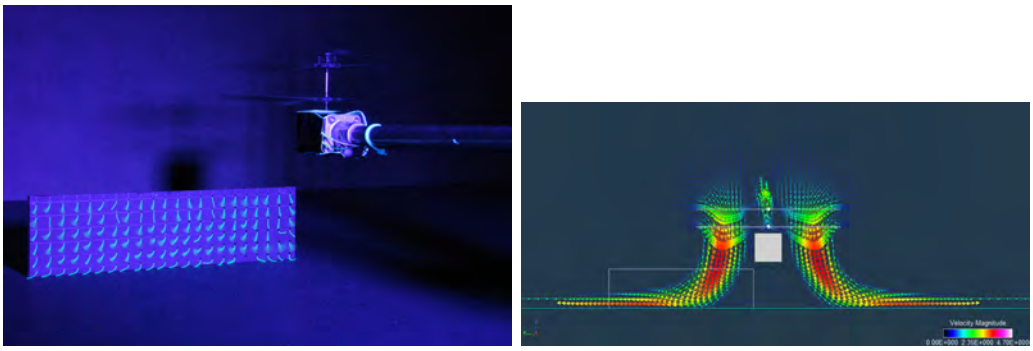

Figure 7.8: Flow field visualization of vertical plane with height "15cm" and plane inclination zero (left).Tuft pattern visualization of vertical plane, under the rotor, with height "15cm" and plane inclination zero (right).

When looking at the ground plane, there is an almost symmetrical pattern of tufts/vectors pointing radially outwards from where the rotor wake hits the surface (Figures 7.10, 7.11 and 7.12). Furthermore, in these simulations in all cases where there was no inclination the maximum velocity observed falls outside of the area directly below the rotor disk. Simulations suggest an azimuthal symmetry and a radial dependency of the speed, therefore justifying the placement of a single vertical board during the tuft testing to visualize the entire phenomena. Moreover, by comparing the ground plane simulations, it is evident that the inclination does not affect the maximum

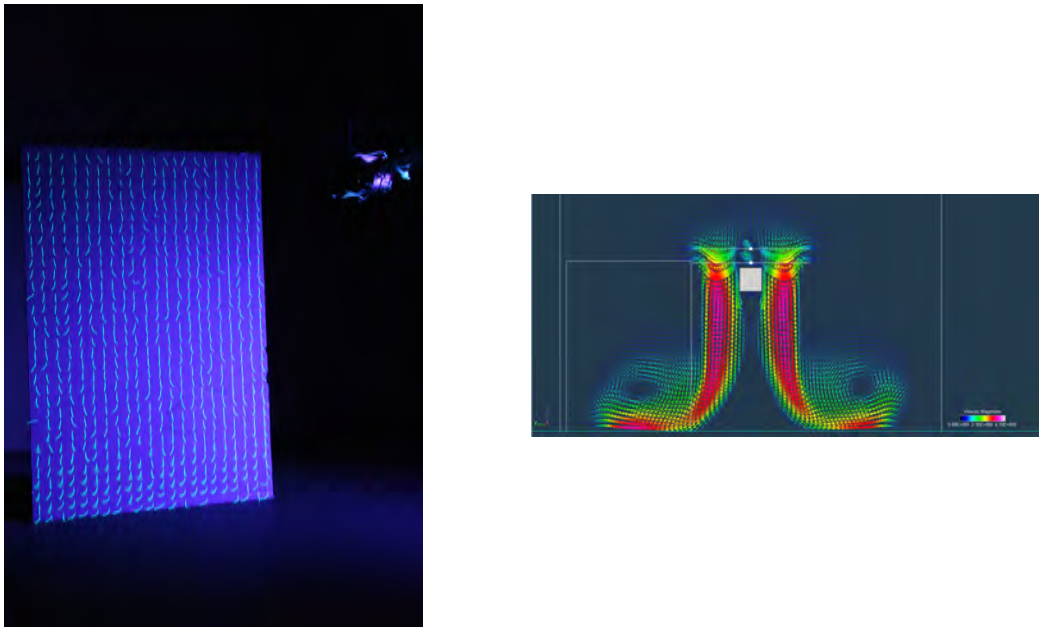

Figure 7.9: Flow field visualization of vertical plane with height $3R$ and plane inclination zero (left). Tuft pattern visualization of vertical plane, under the rotor, with height $3R$ and plane inclination zero (right).

velocity reached at ground level (see figure 7.13).

Unlike the previous conclusion, the heights appear to influence the maximum speed in an inverse proportion. By comparing figures 7.14a, 7.14b and 7.14c it can be concluded that the maximum wake velocity decreases as we get further away from the floor.

For height $3R$, it can be seen that there are vortices forming at ground level (figure 7.9). This is specially interesting considering that it is the one height "out-of-ground effect". It is important to point out that the other two heights also present a vortex. Yet these occur sooner, at 0.35 s as opposed to the 1 s of the $3R$ height.

What is more, the maximum velocities reached in all cases of zero inclination were all not at a same distance from the centre of the rotor (table 7.1).

The maximum velocity ring would shift from directly under the rotor as the inclination of the plane would increase. This ring seemed to increase in diameter as the heights grew taller and would also start distorting slightly

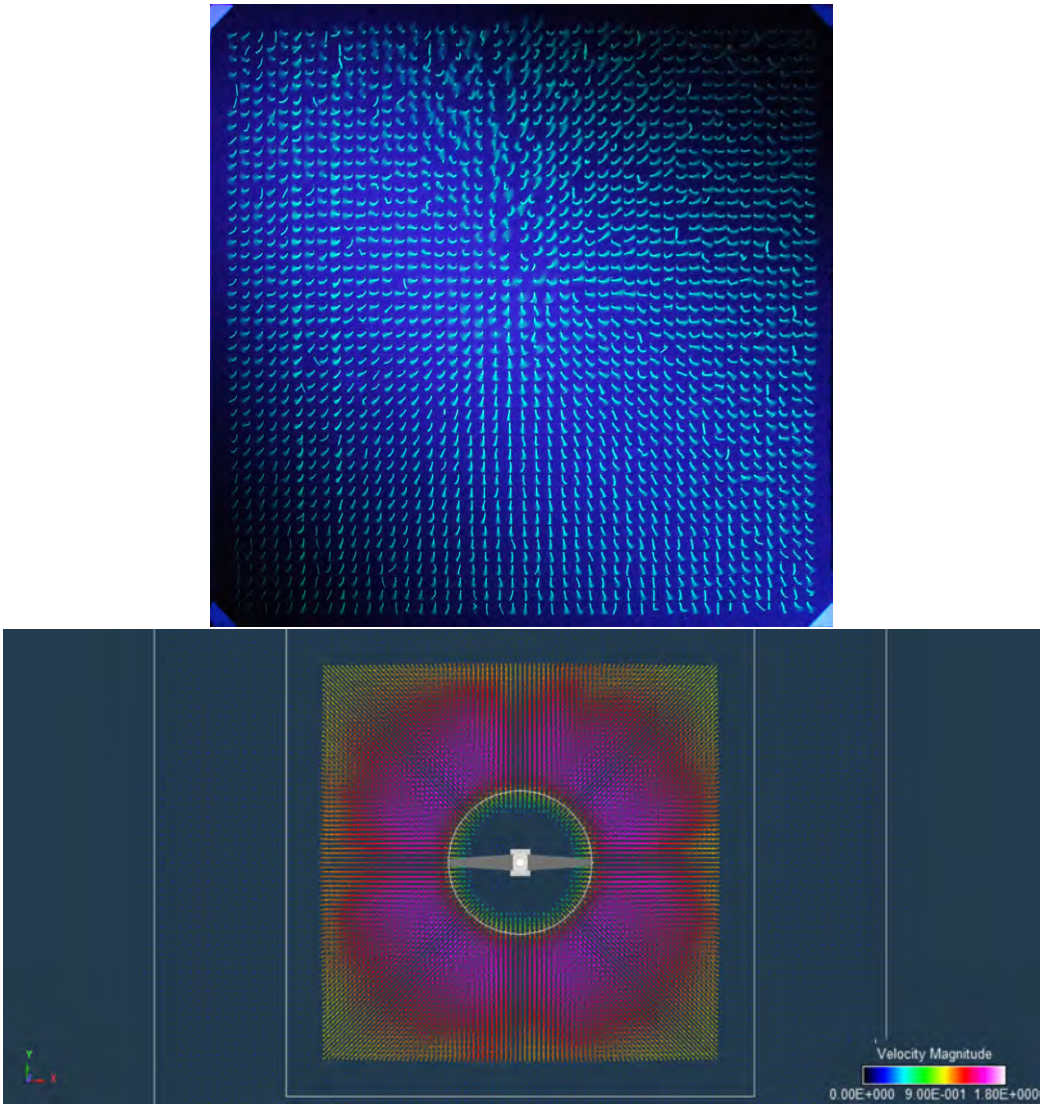

Figure 7.10: .Tuft pattern visualization of horizontal plane, under the rotor, with height "wheels on ground" and plane inclination zero (top). Flow field visualization of horizontal plane with height "wheels on ground" and plane inclination zero(bottom).

into an oval. Despite this not being obvious in the tuft testing results, it is clear in the simulations.

An other important fact to point out from the previous table, (table 7.1)

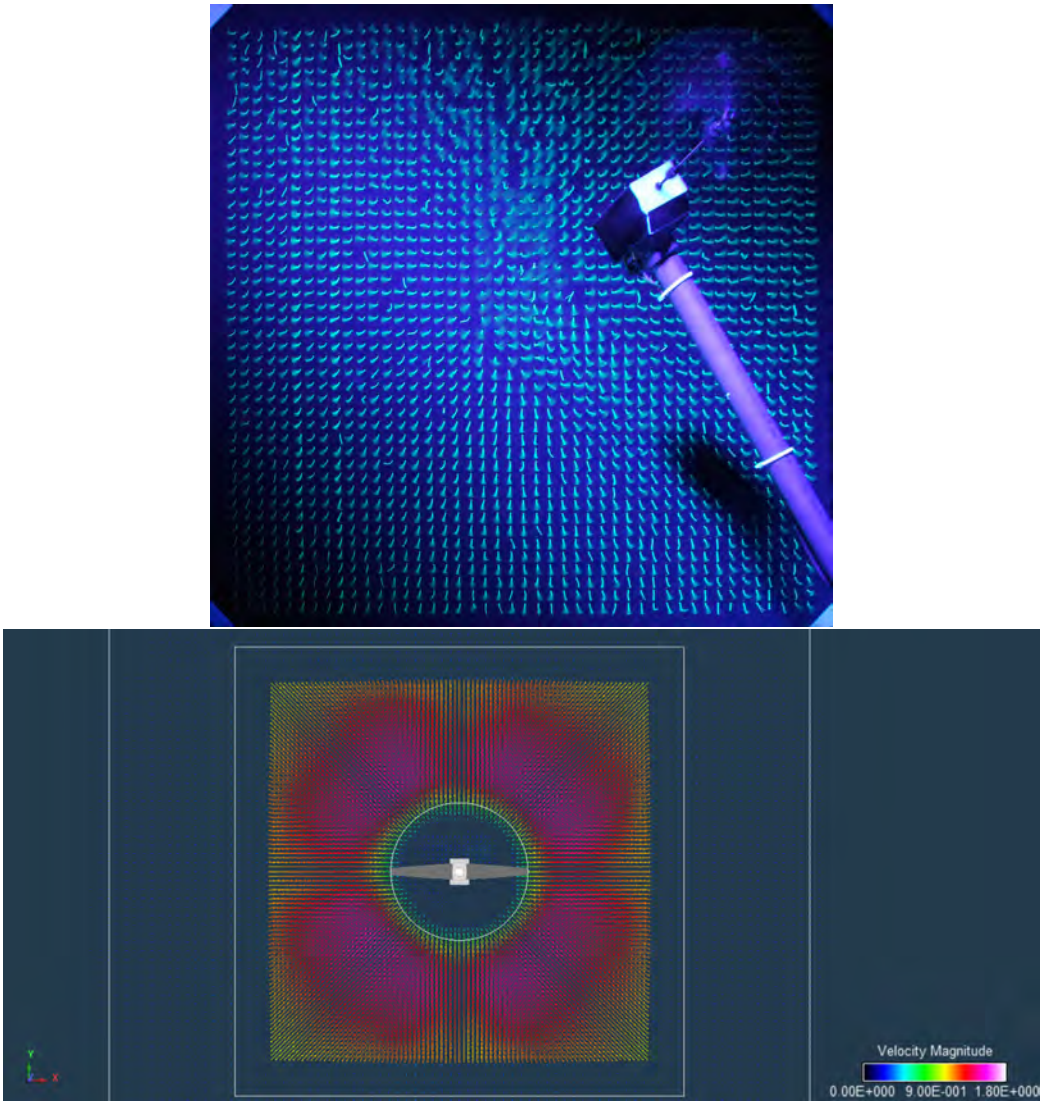

Figure 7.11: Tuft pattern visualization of horizontal plane, under the rotor, with height "15cm" and plane inclination zero(top). Flow field visualization of horizontal plane with height "15cm" and plane inclination zero(bottom).

is how the distance at which the CWS begins saltation also increases as the height of the rotor increases. Furthermore, given the time and distance at which saltation began, according to the PIV and tcomparing these to the simulations, we see how for each height the airflow velocity is of 2.6 m/s

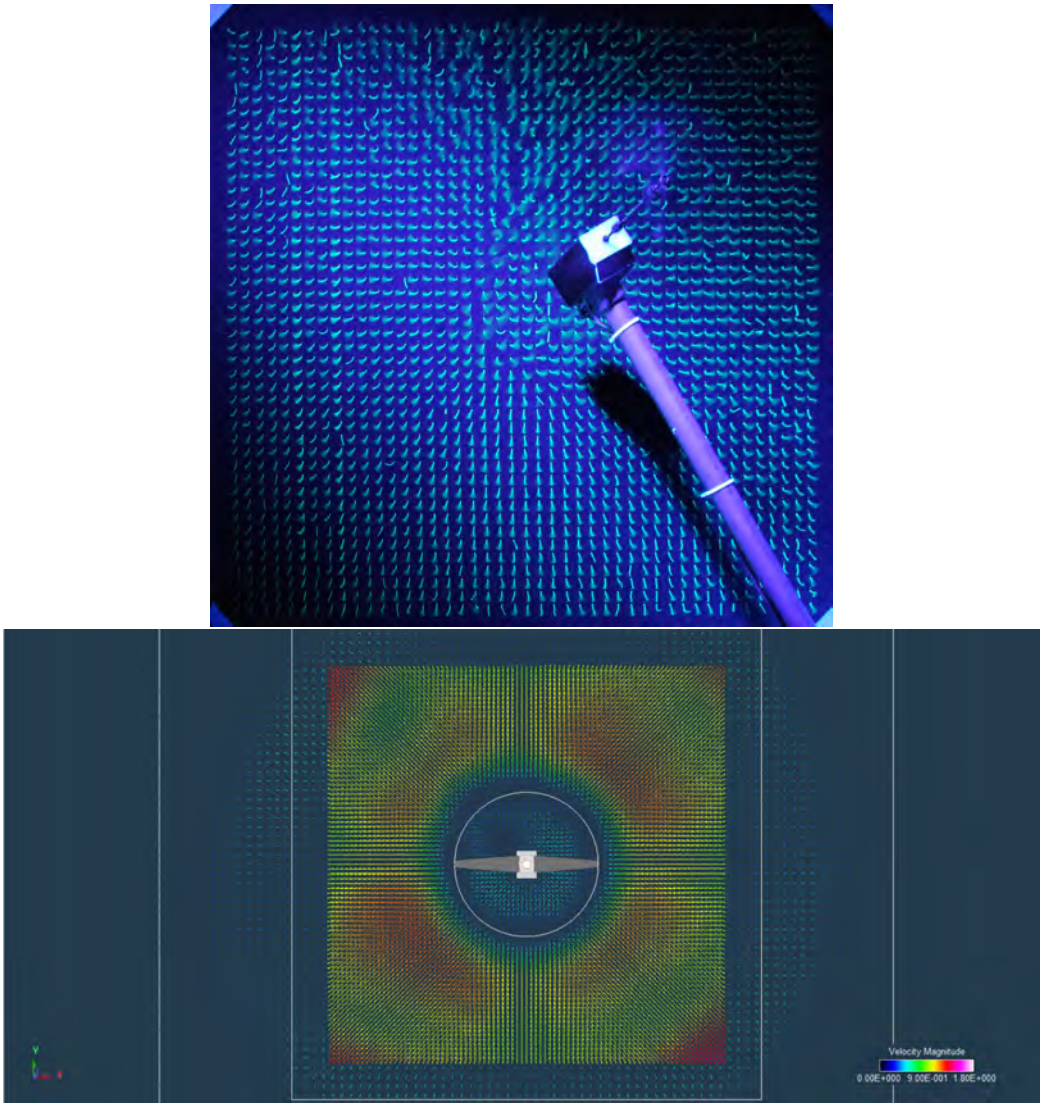

Figure 7.12: Tuft pattern visualization of horizontal plane, under the rotor, with height "3R" and plane inclination zero(top). Flow field visualization of horizontal plane with height "3R" and plane inclination zero (bottom).

(figures 7.15, 7.16 and 7.17).

On the other hand, it is important to point out that the wind velocity rapidly decreases after its maximum (Figures 7.7, 7.8 and 7.9). This would suggest that although it may be enough to initiate saltation, the amount of

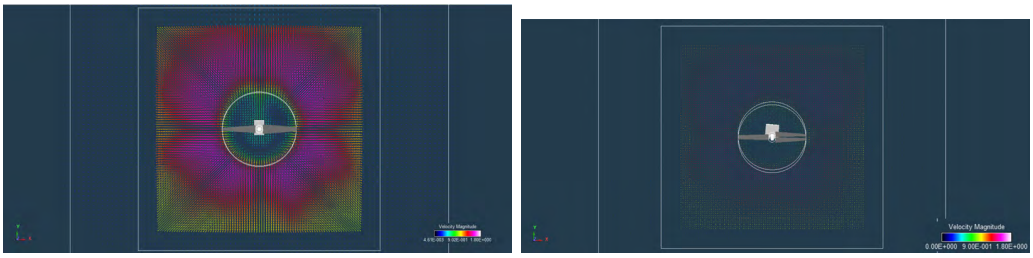

Figure 7.13: Flow field visualization of the horizontal planes with height "wheels on ground" and plane inclination of 5° (left) and plane inclination of 20° (right).

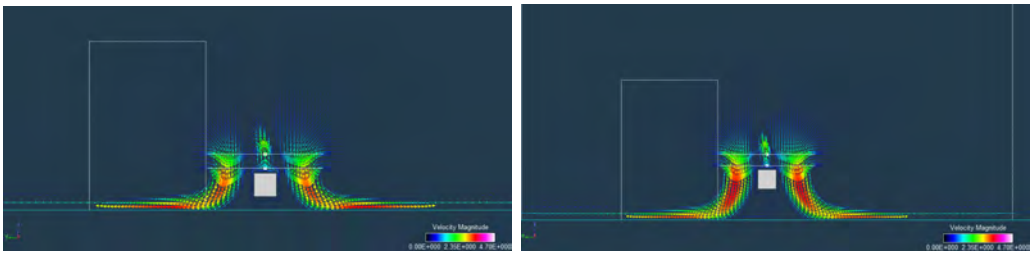

(a) Wheels on ground (b) 15 *cm*

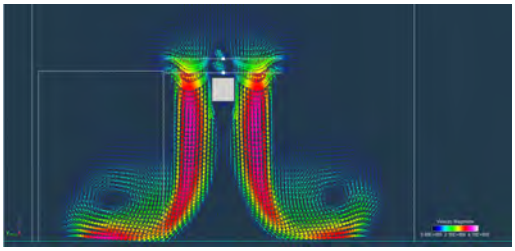

(c) 3R

Figure 7.14: Flow field visualization of the vertical plane with no angle of inclination for all three heights.

dust lifted may not be significant, meaning that the dust cloud would not be very dense, which can be easily seen in both dust experiments (for example figures 7.15 and 7.2).

	Height 1	Height 2	Height 3
u_{max}	149.2 mm ±0.5 mm	183.7 mm ±0.4 mm	264.7mm ± 0.5mm
Saltation	116.6±0.2 mm	166.8±0.2 mm	168.4±0.2 mm

Table 7.1: Comparison between the distances at which the simulations reach their maximum velocity and the distance at which the the CWS particles first began their saltation process in the dust laser wall experiment. These last distances were obtained by doing a particle image velocimetry (PIV) analysis.

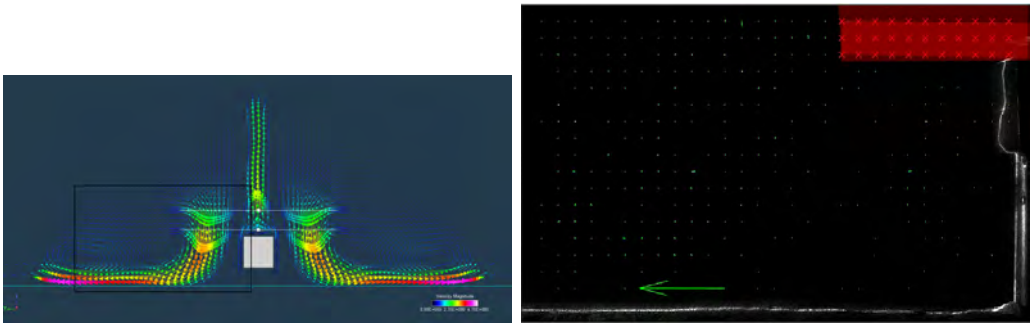

Figure 7.15: Comparison between simulation at 0.36 seconds and the PIV analysis done to laser wall experiment at height "wheels on ground".

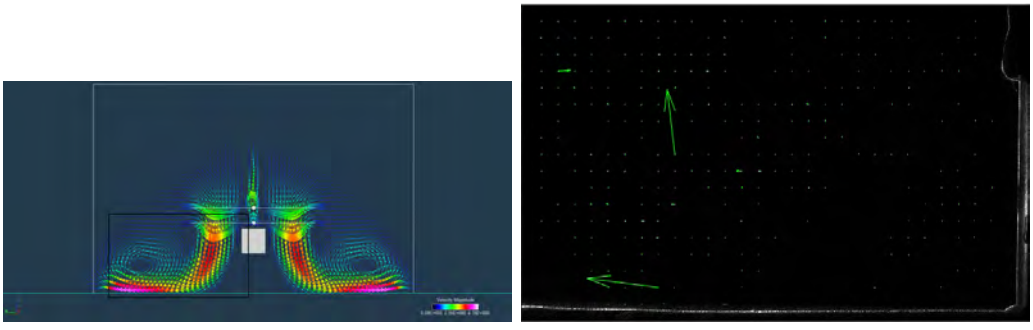

Figure 7.16: Comparison between simulation at 0.45 seconds and the PIV analysis done to laser wall experiment at height "15cm".

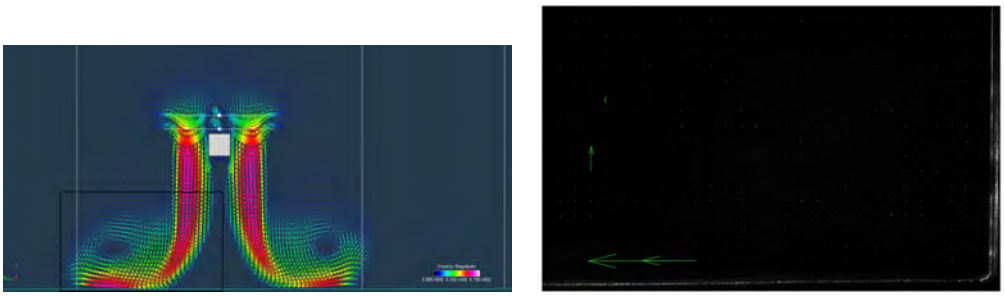

Figure 7.17: Comparison between simulation at 0.56 seconds and the PIV analysis done to laser wall experiment at height “3R”.

Chapter 8

Conclusion

The experiments and simulations in this thesis were all done in optimal conditions for dust saltation, while staying as close to the "real problem" as possible. That is, that despite the helicopter model being a close scaled representation of what is planned to be the full-scale MHS, the environment surrounding it is different. The density and composition of the atmosphere were the main differences, since gravity was accounted for in the selection of the "Martian dust" emulator, crushed wallnuts. From the simulations done we see that the case in which the air reaches its maximum velocity is when the plane is at inclination zero and height "wheels on ground"(figures 7.14a, 7.6b and 7.6c).

In conclusion, the maximum wind speed the model reached at ground level is: 3.326 m/s (figure 7.14a). The direction of this velocity is parallel to the ground and its magnitude is much larger than the theoretically necessary to induce saltation at Martian atmospheric density (0.5366 m/s) and at Earth's (0.02261 m/s). However, saltation begins at a distance grater than the rotor radius at all heights. Therefore, given that the cloud density was very low (for example figure 7.2) and begins far from the rotor, it is possible to say with the information at hand, that the dust cloud created by the MHS will not pose a problem when taking off and landing, since it will not be dense enough to block or obstruct the sensors.

Given the exploratory nature of this thesis, the experiments proposed to study this phenomenon came up as the study progressed. Thus, it is important to point out the obvious disadvantages of the methodology of one of the experiments in particular; the tuft experiment. Although some information may be extracted from these tests, there is a highly evident

problem which is the presence of the board in the experiment, not to mention the tufts themselves. The presence of a rough surface in an airflow changes entirely the problem to the extent that it may be considered incomparable to the simulations. Moreover, given the success of the last experiment done, the laser wall experiment combined with the PIV analysis, it is recommended for further work. Despite these tests suggesting a positive result regarding the lack of danger caused by the cloud, further tests are recommended. The next suggested test would be repeating both the dust test and the tuft test at reduced pressures. This would give us more information regarding saltation at low atmospheric densities. Moreover, dust simulations using RotCFD's dust unit are recommended for both the dust testing presented in this thesis and those proposed at lower pressure. Furthermore, additional alterations must be done in order to get better results. In the tuft test experiment, a suggested improvement would be to substitute the boards for a string mesh in order to intrude less on the airflow. Placing the camera perpendicular to the planes is also recommended since it is difficult to properly compare results with the simulations. This would be possible since there would no longer be a plane to reflect the light of the UV-lamp and saturate the camera.

Further information can be extracted from doing a more thorough analysis of the numerical simulations. For example, finding quantitative relation between the structure of the airflow near the bottom surface, and the height, inclination, and tip velocities of the rotor disk relative to the floor. Another quantitative result would be a graph reflecting the changes in airflow speed throughout time at different points of the area of interest. These changes would give a better idea of what is happening and at what point in time and space could one expect saltation. Furthermore, finding the RPM of the helicopter at which a dust cloud is produced that can be considered dense enough to be a problem, is also proposed for future tests. This could help us further understand the relation between the rotor's rotation and dust saltation.

After this first attempt to study the complex applied problem of brownout, it has become clear what the path to finding the theoretical description is. The experimental techniques and simulations have left us with a desire for quantitative results in order to explore the physical phenomena and go beyond a simple qualitative answer.

Acknowledgements

- NASA AMES Aeromechanics Branch
- Dr. William Warmbrodt
- Dr. Larry Young
- Dr. Alan Wadcock
- Eddie Solis
- Michelle Dominguez
- Geoffrey Ament
- Witold Konning
- NASA I^2 Program
- Agencia Espacial Mexicana
- Sofia Ixchel Michaelian Martínez
- Hydrodynamics Laboratory of the Facultad de Ciencias, UNAM

Appendices

Appendix A

Dust Results

A.0.1 White Light Experiment

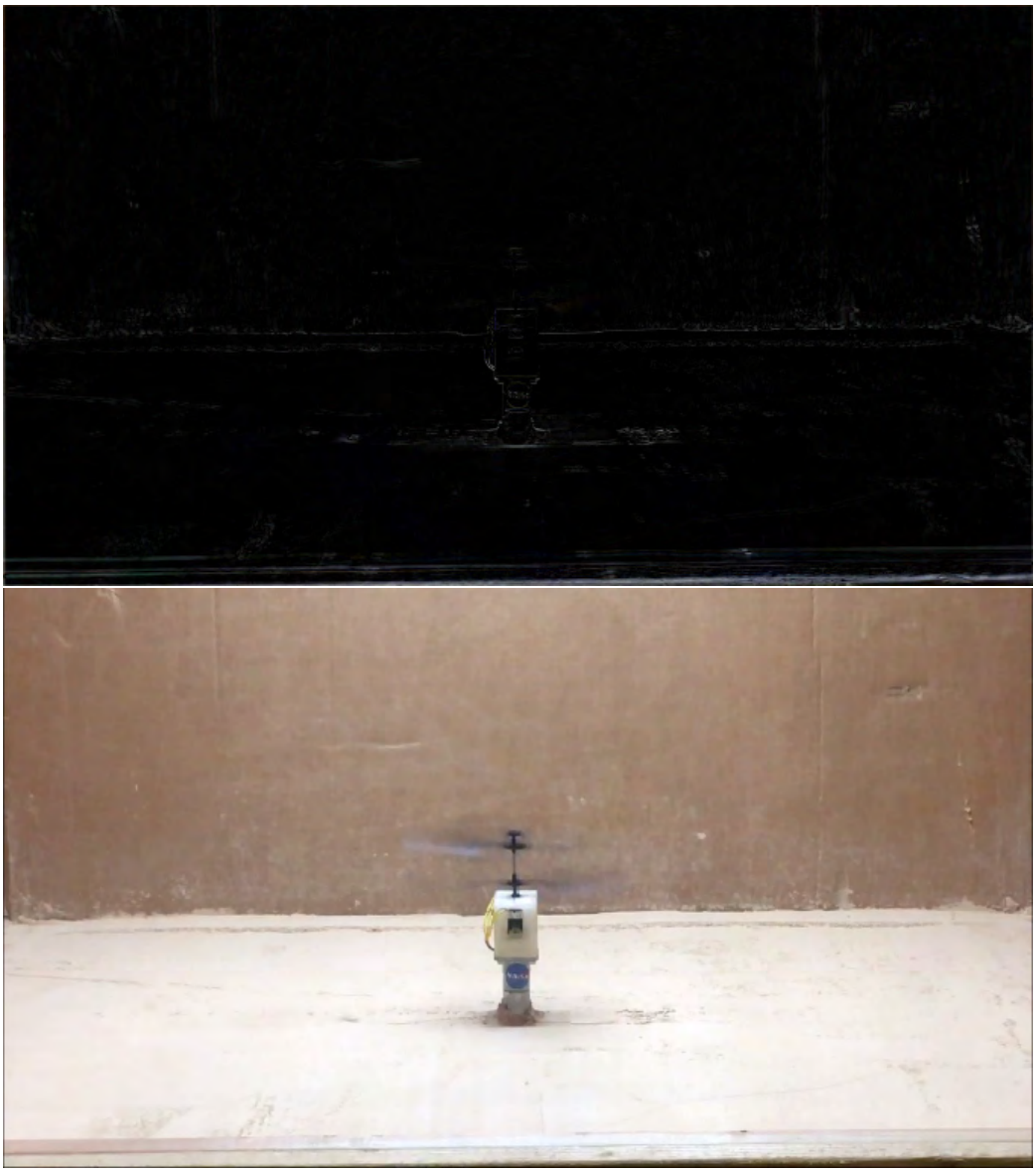

Figure A.1: Difference between a frame with no CWS movement and that of the first frame where there is movement(0.36 s since helicopter was turned on)(top).1^{st} Still frame of CWS in saltation (bottom).

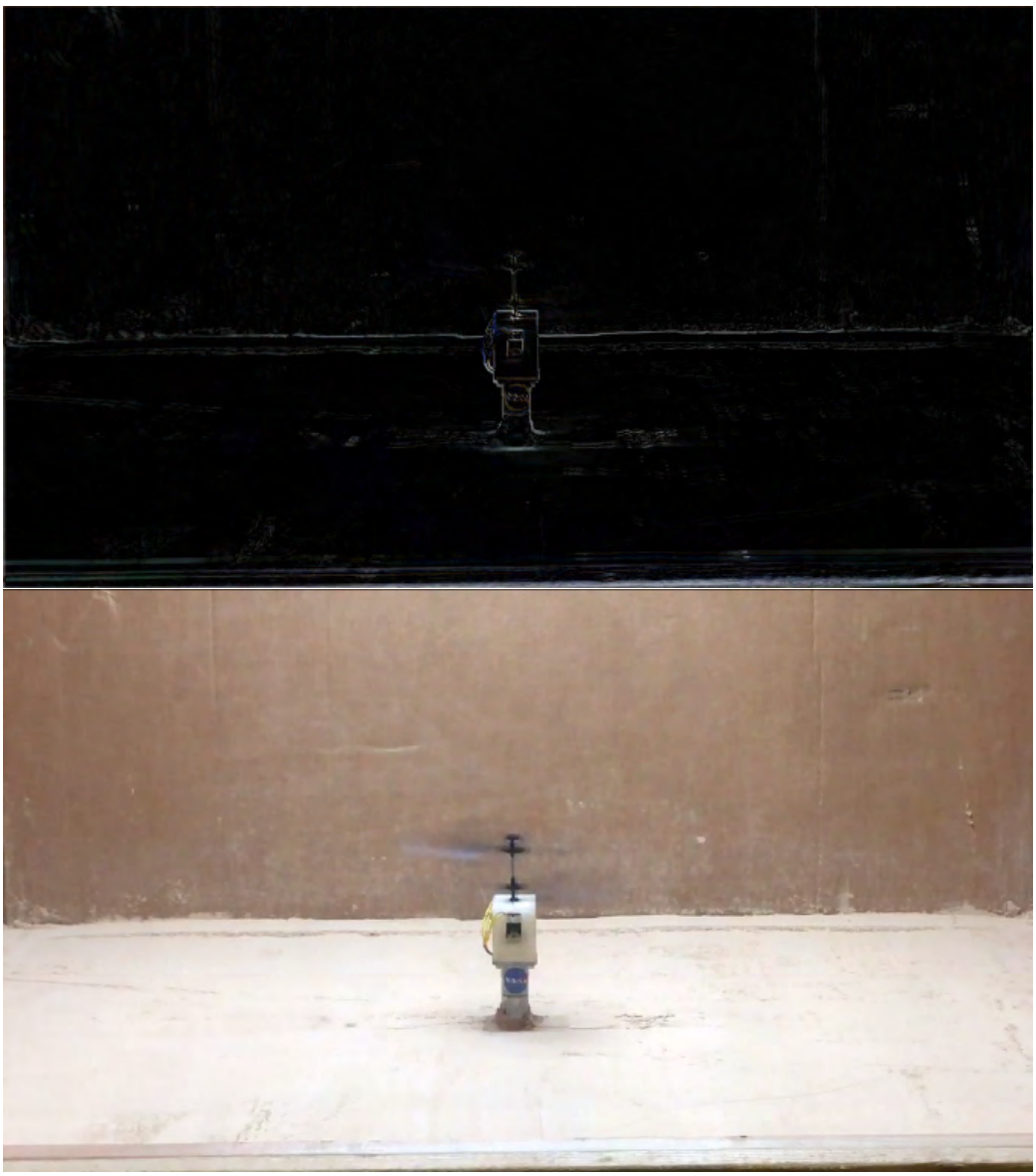

Figure A.2: Difference between a frame with no CWS movement and that of the second frame where there is movement(0.40 s since helicopter was turned on)(top).2^{nd} Still frame of CWS in saltation (bottom).

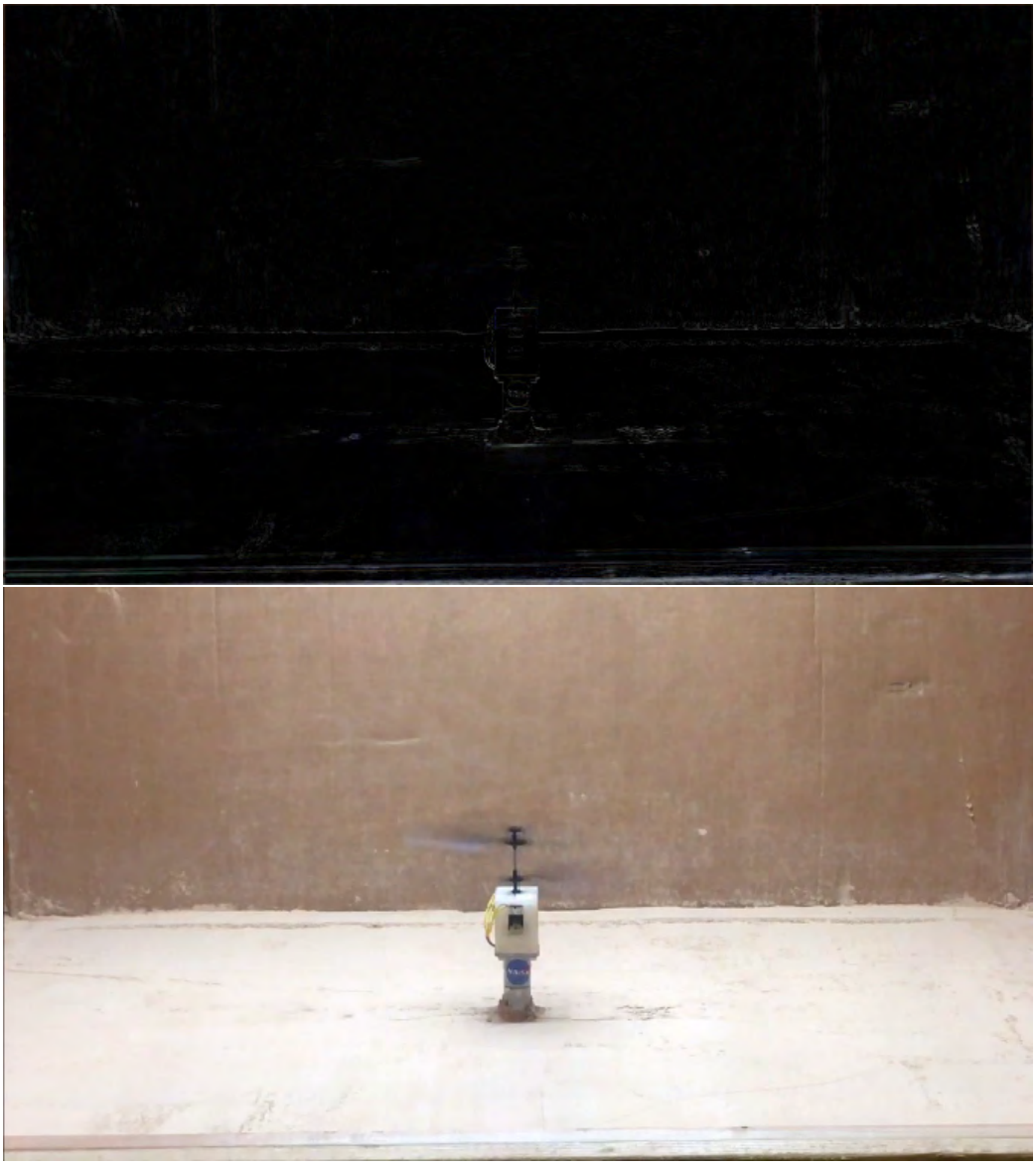

Figure A.3: Difference between a frame with no CWS movement and that of the third frame where there is movement(0.43 s since helicopter was turned on)(top).3^{rd} Still frame of CWS in saltation (bottom).

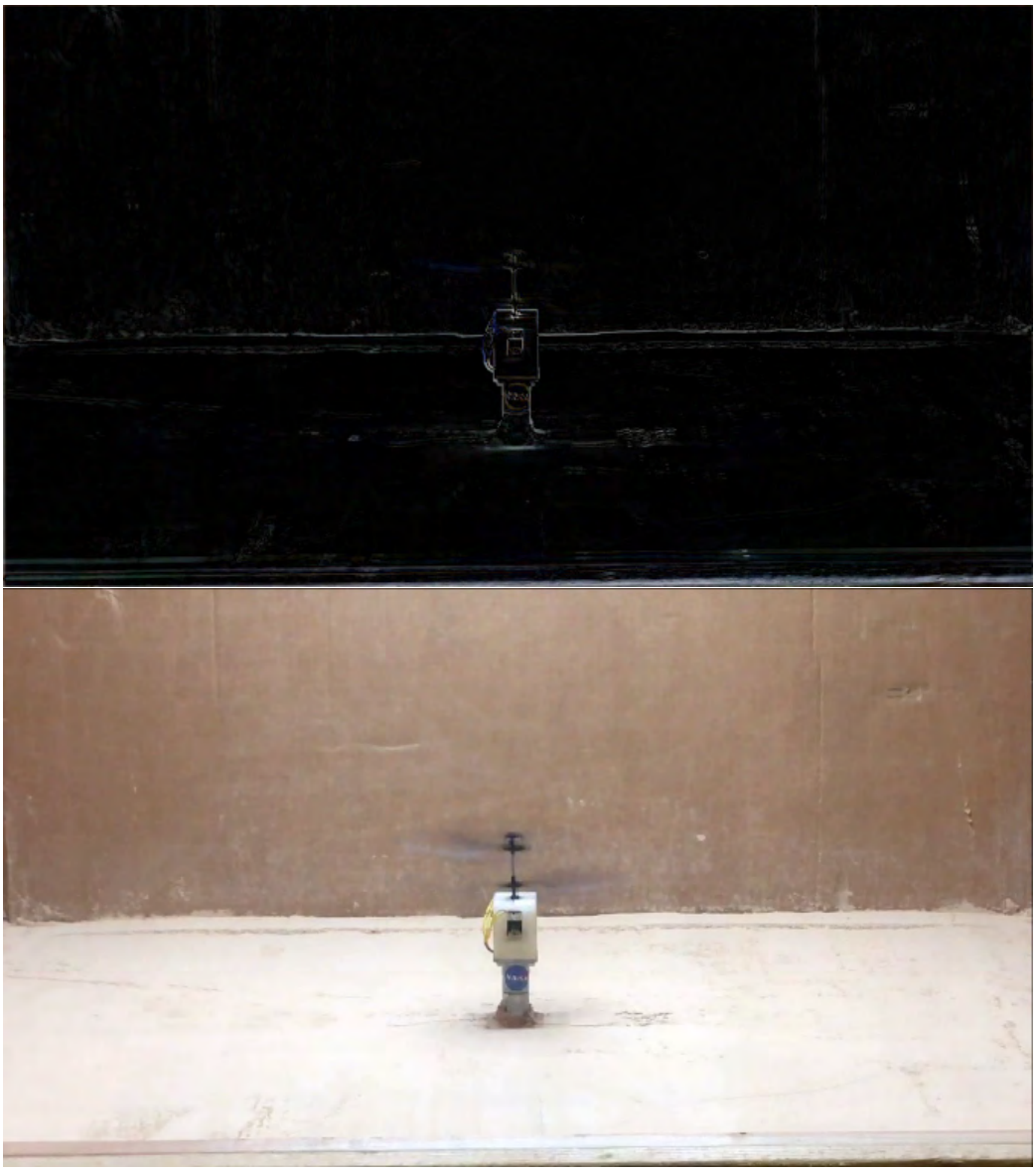

Figure A.4: Difference between a frame with no CWS movement and that of the forth frame where there is movement(0.46 s since helicopter was turned on)(top).4^{th} Still frame of CWS in saltation (bottom).

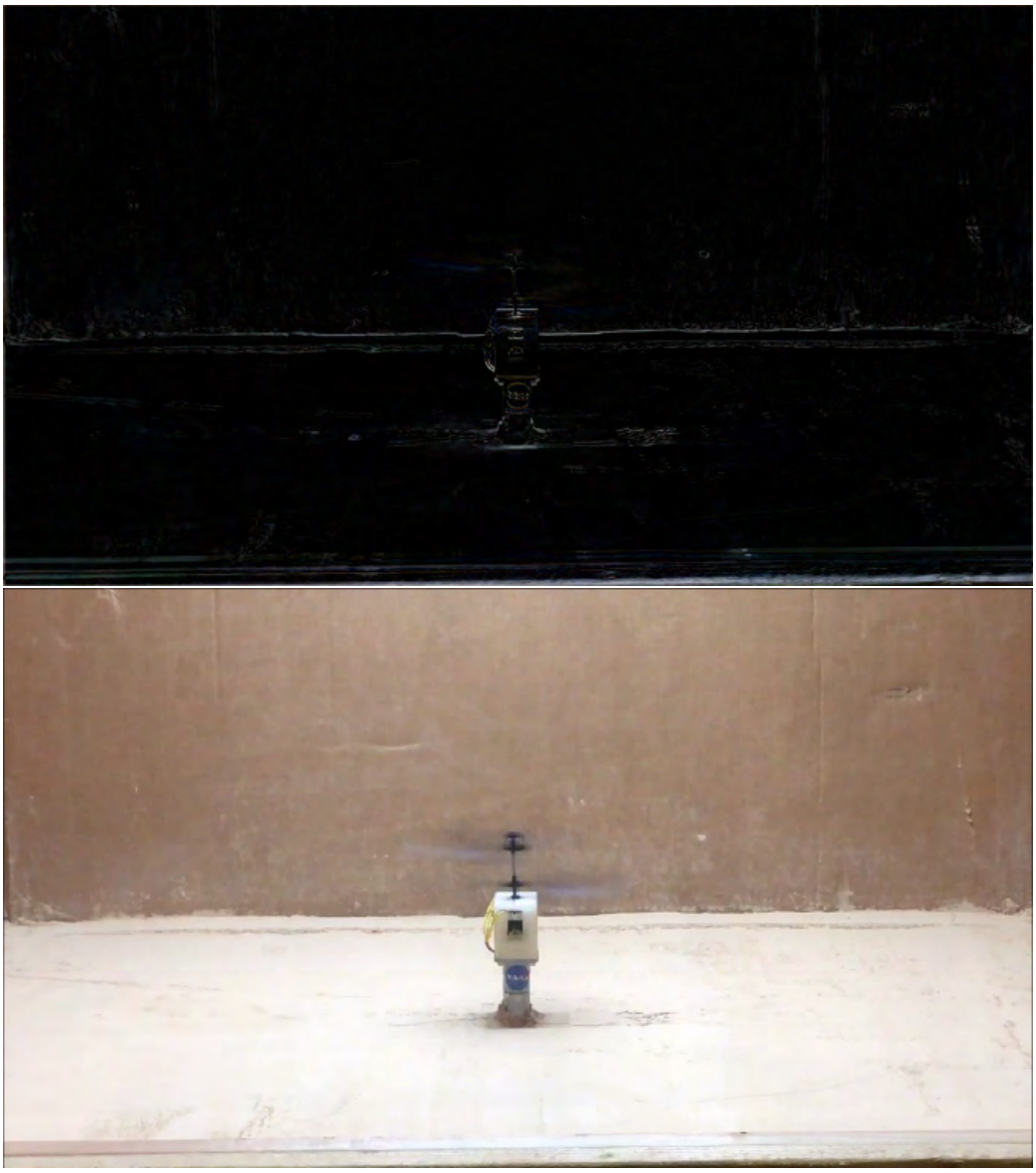

Figure A.5: Difference between a frame with no CWS movement and that of the fifth frame where there is movement(0.50 s since helicopter was turned on)(top).5^{th} Still frame of CWS in saltation (bottom).

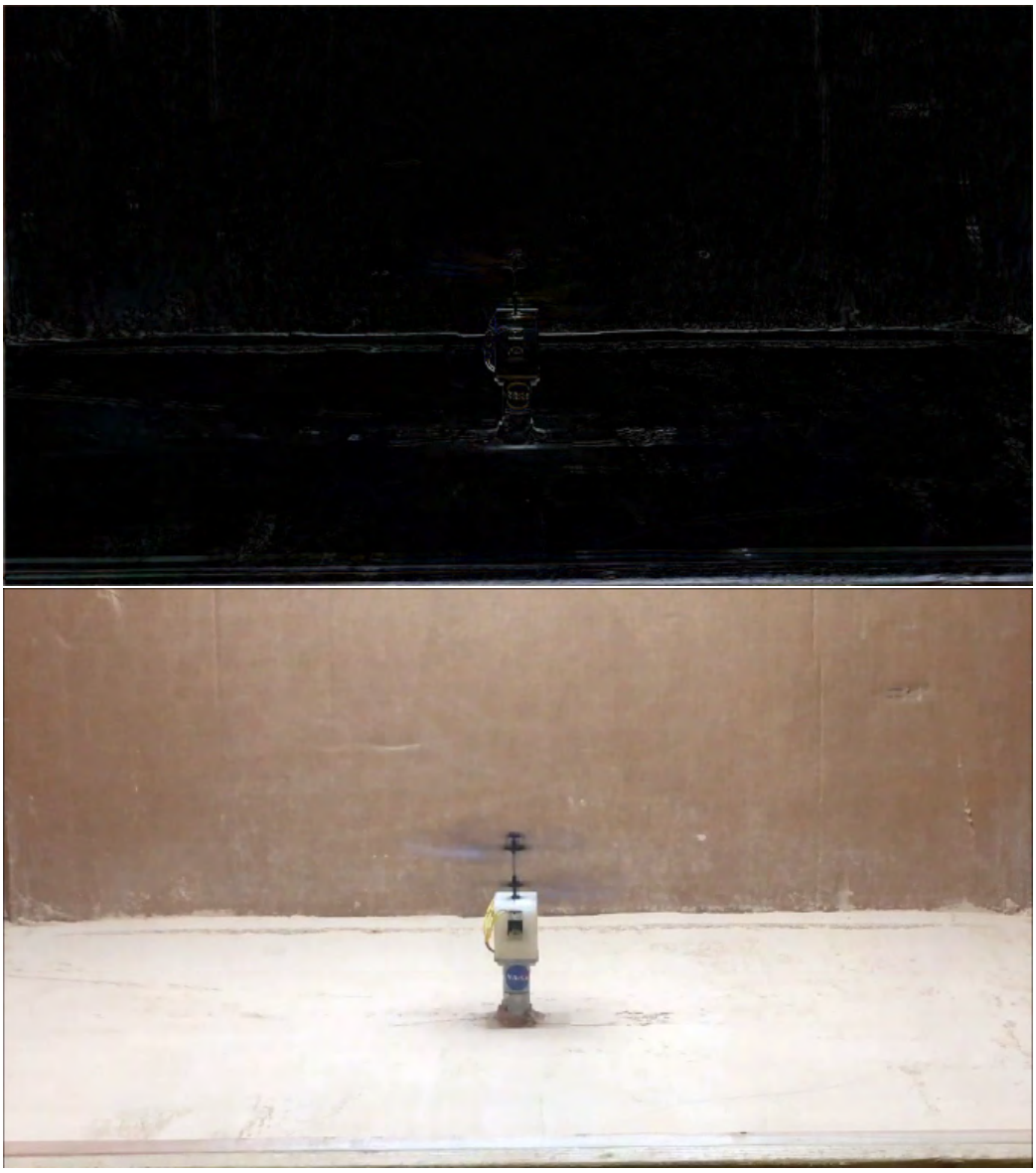

Figure A.6: Difference between a frame with no CWS movement and that of the sixth frame where there is movement(0.53 s since helicopter was turned on)(top).6^{st} Still frame of CWS in saltation (bottom).

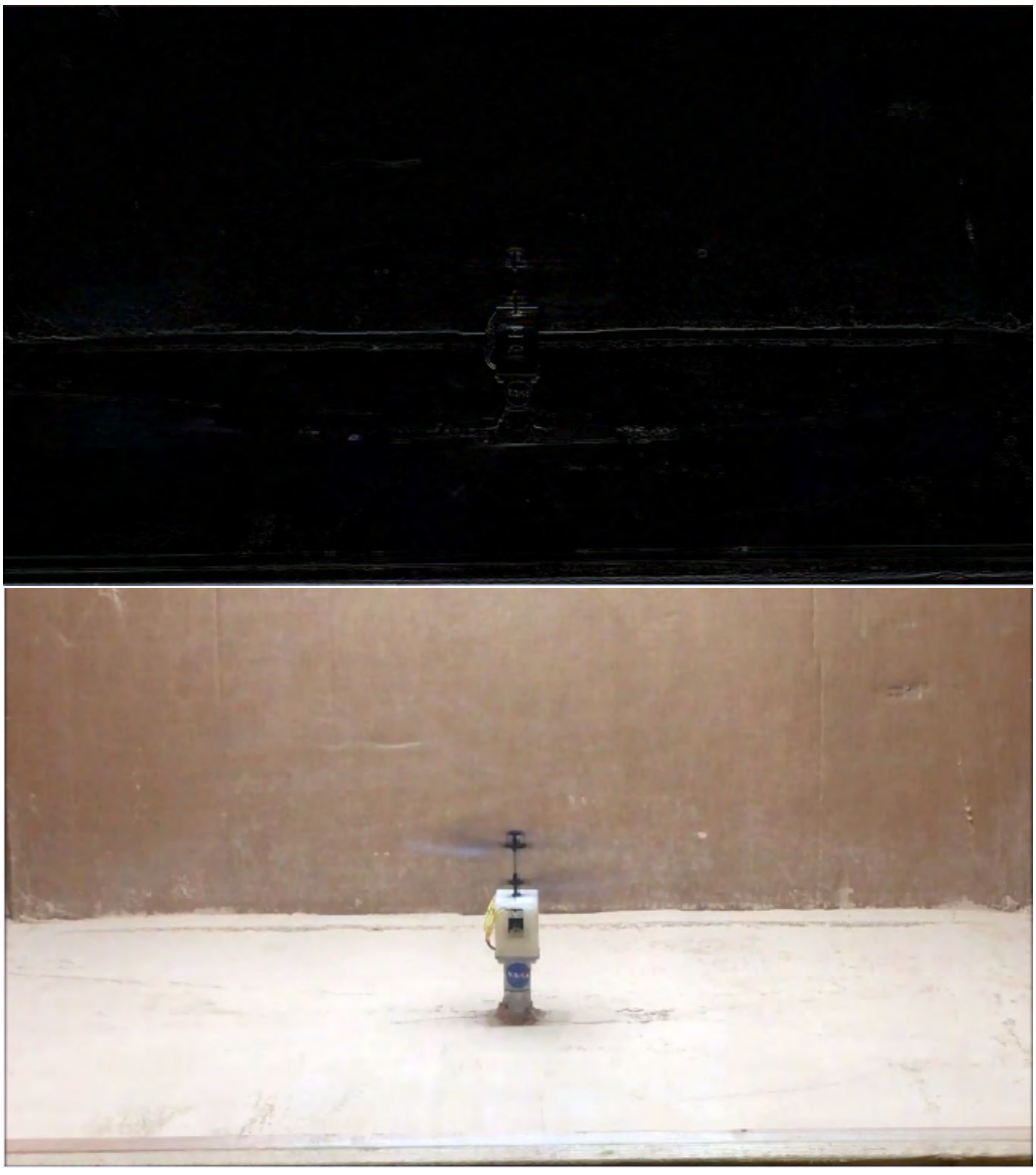

Figure A.7: Difference between a frame with no CWS movement and that of the seventh frame where there is movement(0.56 s since helicopter was turned on)(top).7^{th} Still frame of CWS in saltation (bottom).

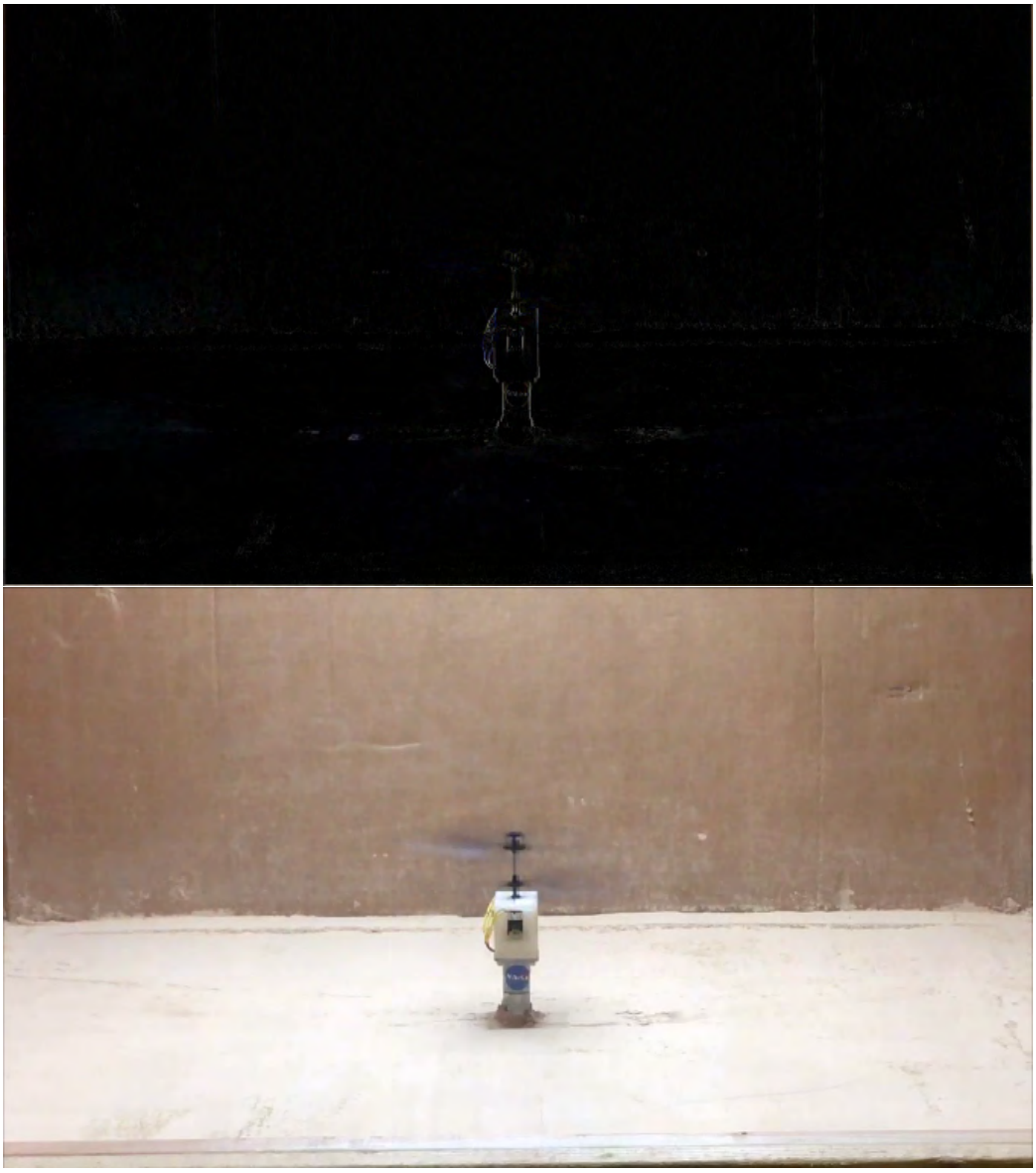

Figure A.8: Difference between a frame with no CWS movement and that of the eighth frame where there is movement(0.60 s since helicopter was turned on)(top).8^{th} Still frame of CWS in saltation (bottom).

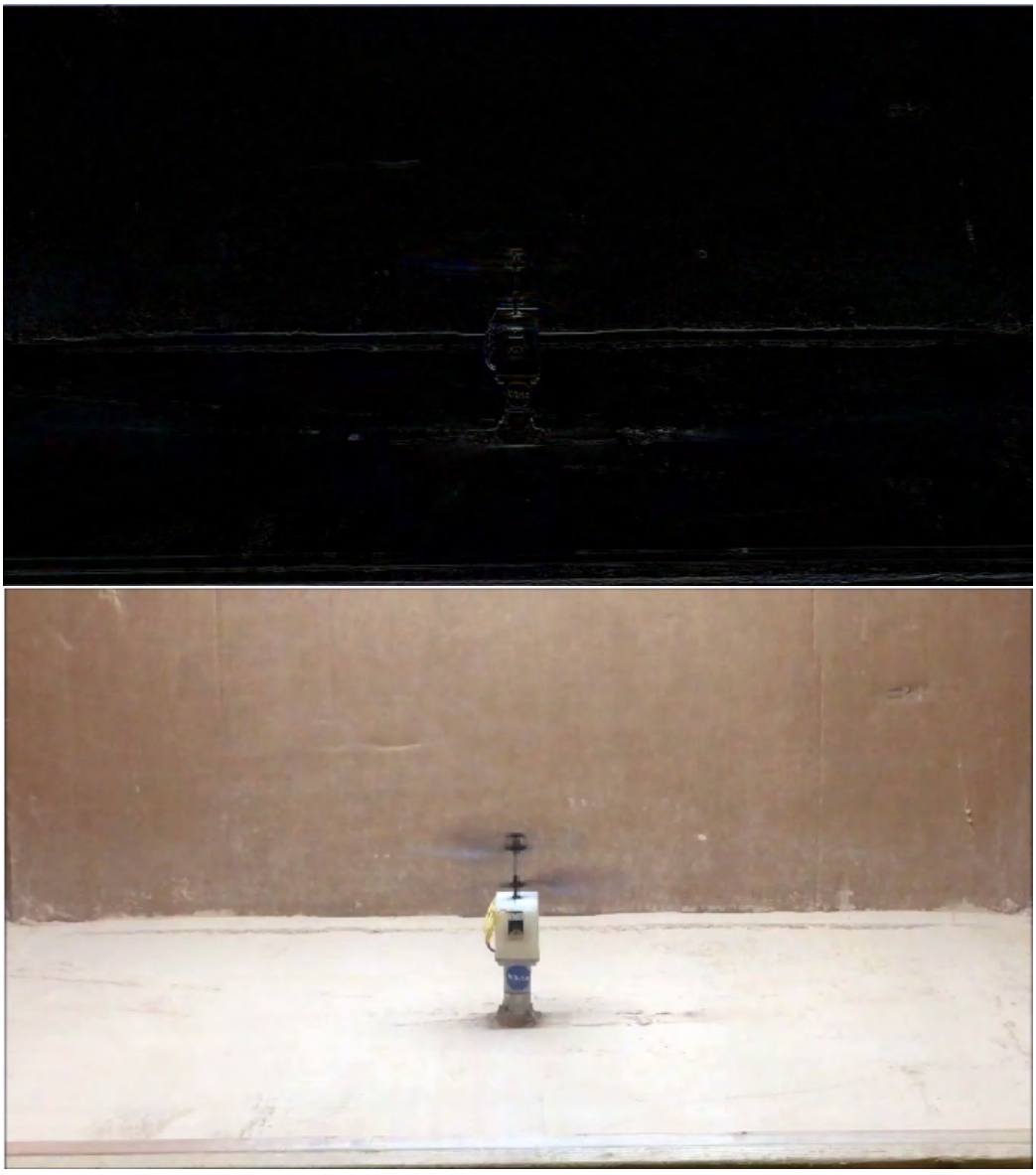

Figure A.9: Difference between a frame with no CWS movement and that of the ninth frame where there is movement(0.63 s since helicopter was turned on)(top).9^{th} Still frame of CWS in saltation (bottom).

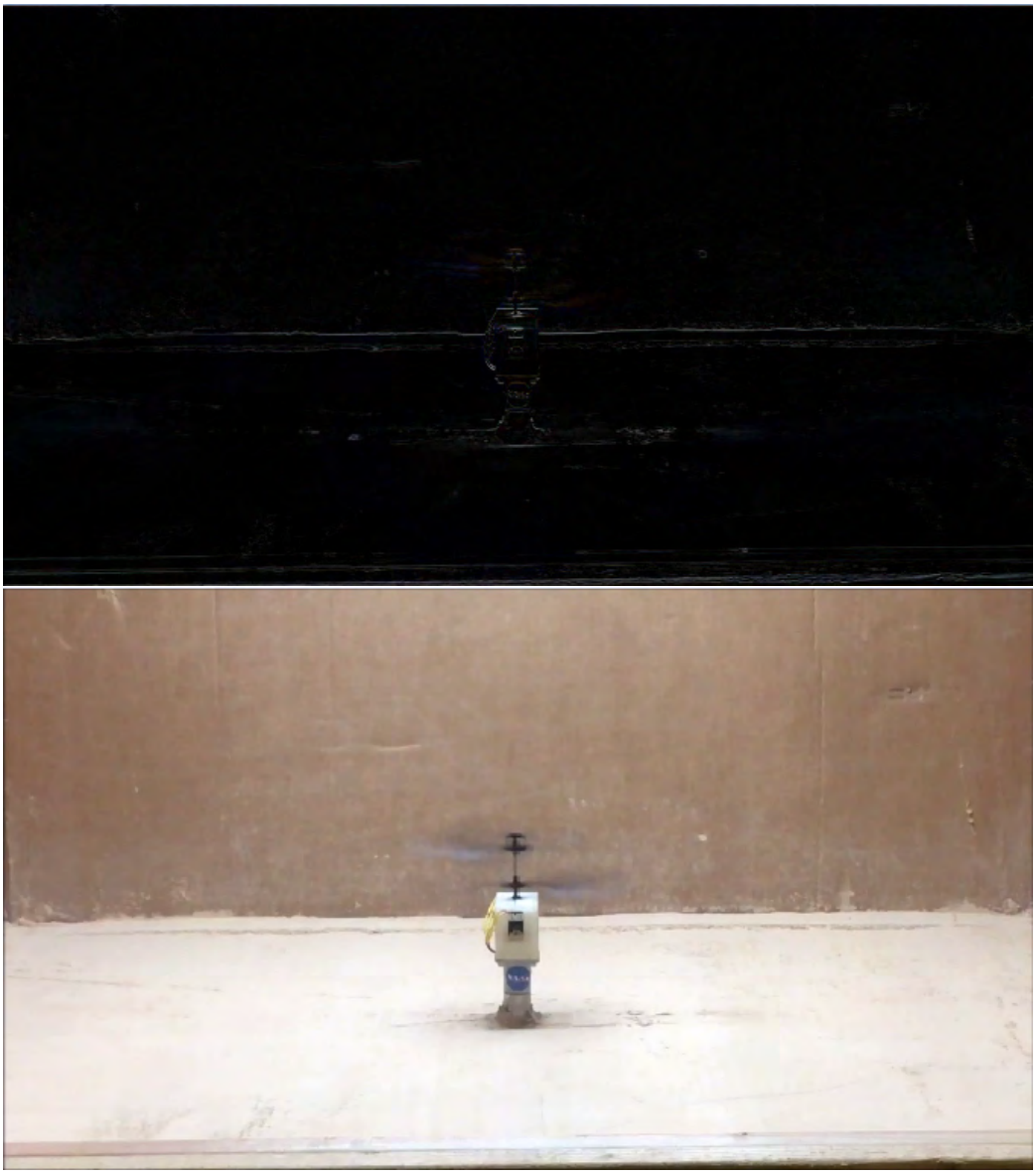

Figure A.10: Difference between a frame with no CWS movement and that of the tenth frame where there is movement(0.66 s since helicopter was turned on)(top).10^{th} Still frame of CWS in saltation (bottom).

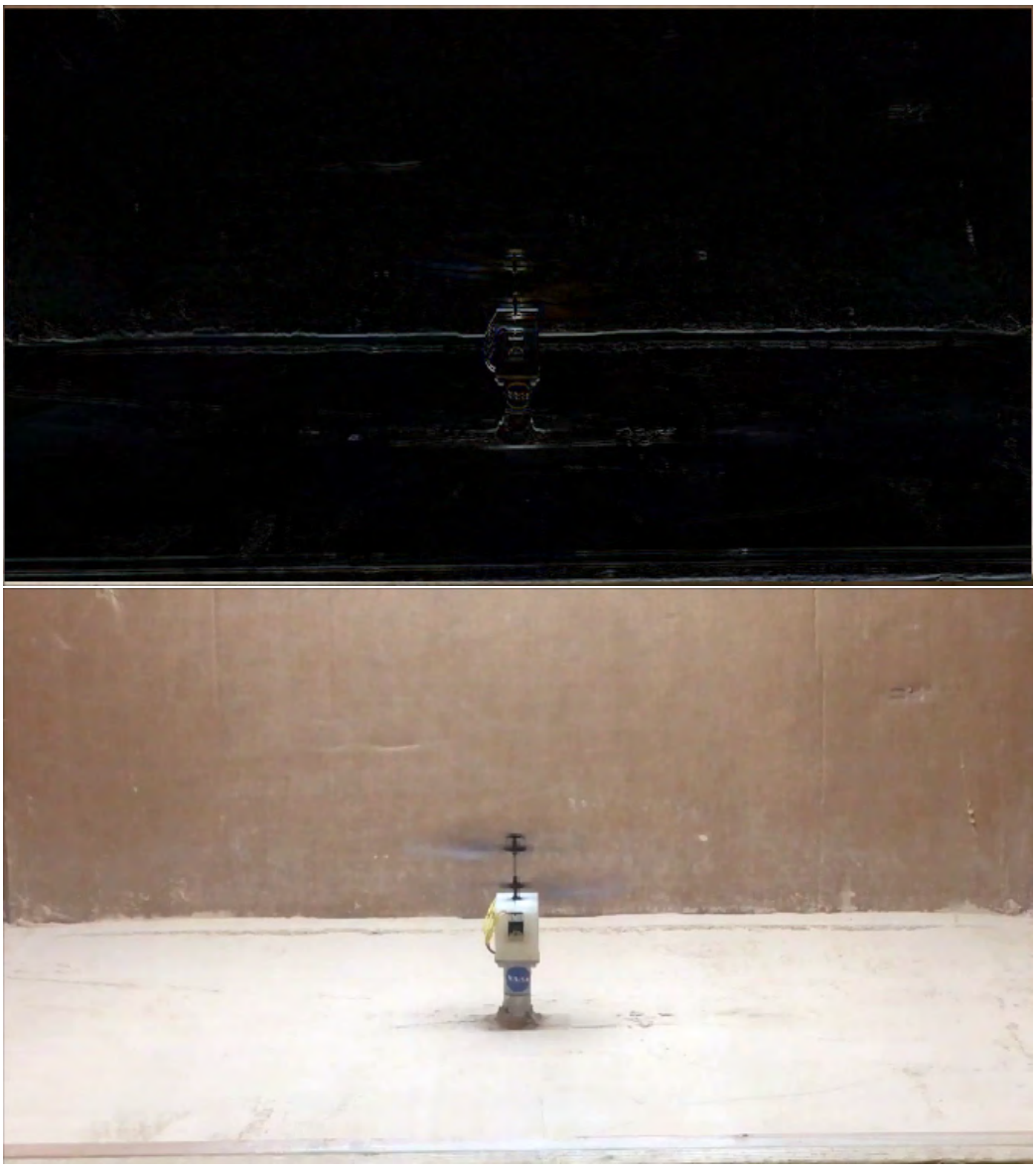

Figure A.11: Difference between a frame with no CWS movement and that of the eleventh frame where there is movement(0.70 s since helicopter was turned on)(top).11^{th} Still frame of CWS in saltation (bottom).

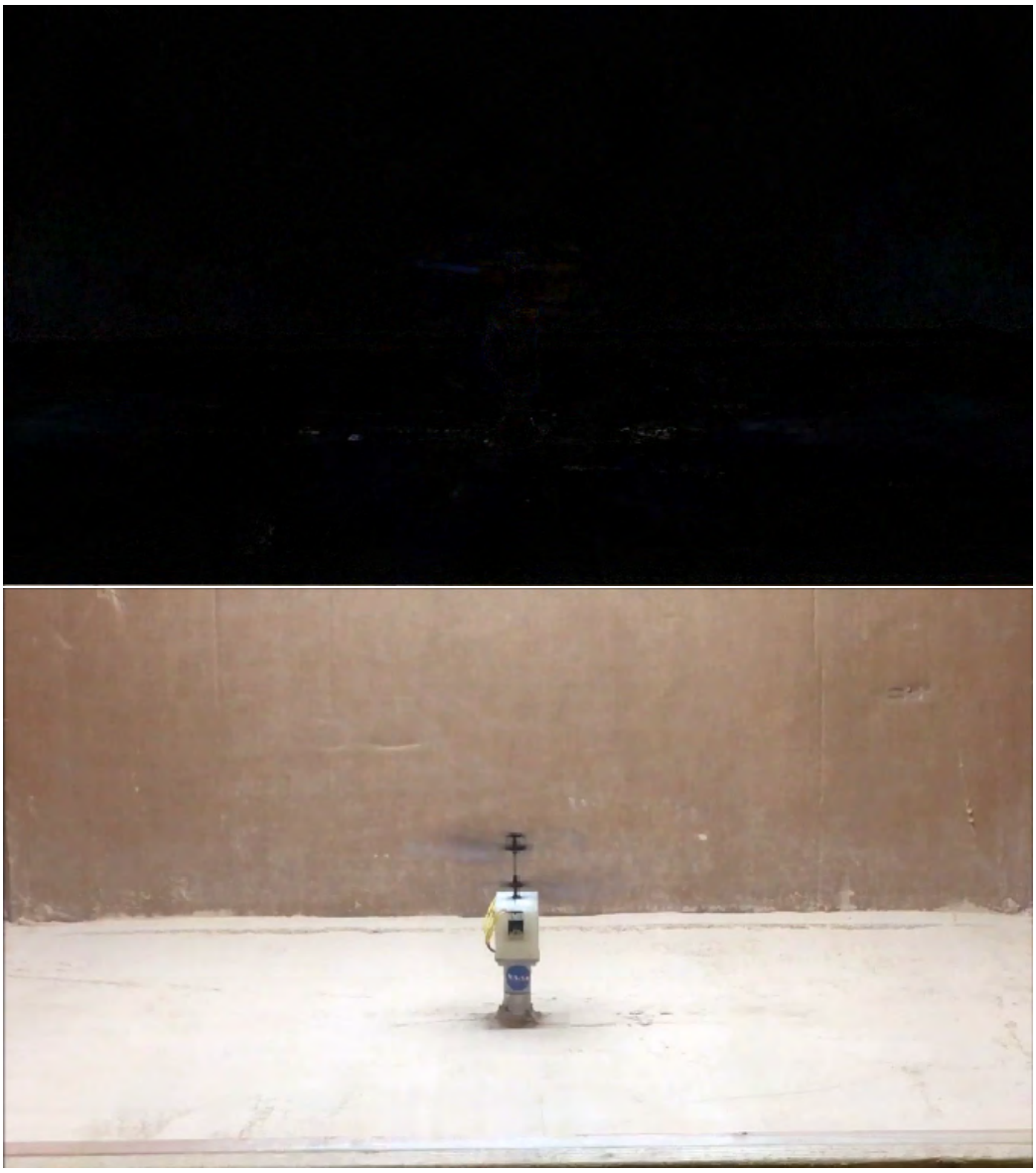

Figure A.12: Difference between a frame with no CWS movement and that of the twelfth frame where there is movement(0.73 s since helicopter was turned on)(top).12^{th} Still frame of CWS in saltation (bottom).

A.0.2 Laser Wall Experiment

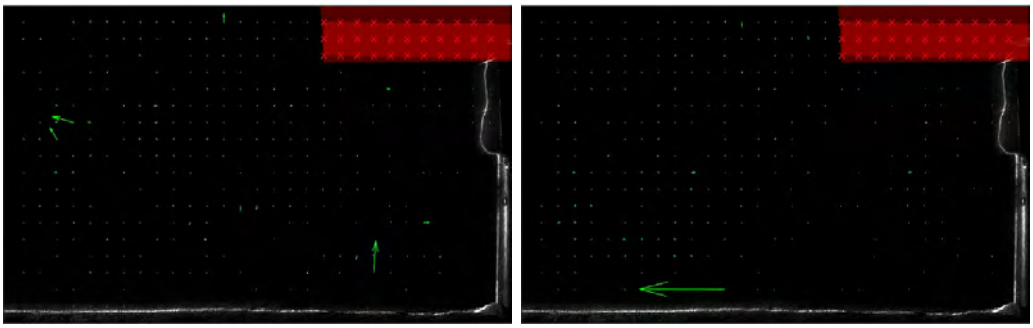

Figure A.13: Vertical Laser plane visualization of the CWS at 0.366 s since helicopter was turned on (Right). It is the first moment at which saltation is seen for height "wheels on ground" . The left image is exactly two frames after, at 0.370 s, and it is the first moment in which the PIV program detects the particle and assigns it a value of 2.6 m/s.

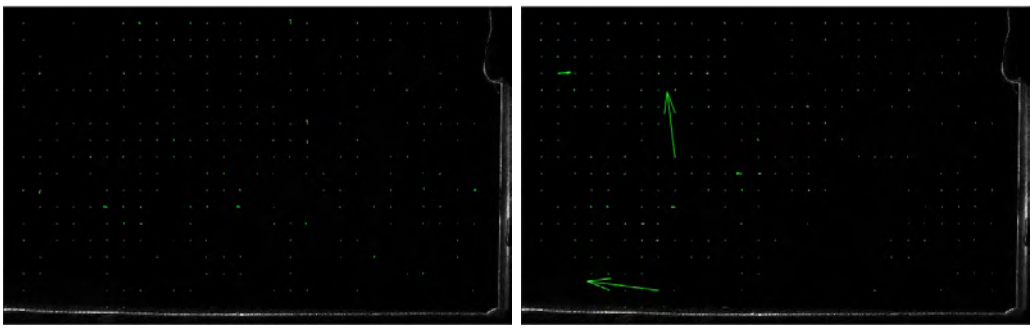

Figure A.14: Vertical Laser plane visualization of the CWS at 0.436 s since helicopter was turned on (Right). It is the first moment at which saltation is seen for height "15 cm" . The left image is exactly one frame after, at 0.438s, and it is the first moment in which the PIV program detects the particle and assigns it a value of 2.6 m/s.

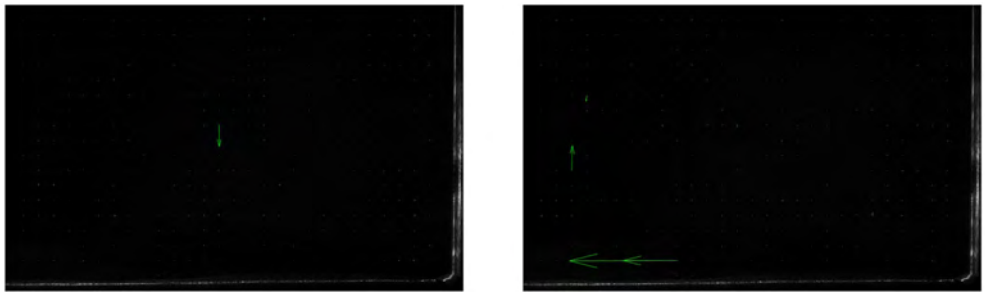

Figure A.15: Vertical Laser plane visualization of the CWS at 0.556 s since helicopter was turned on (Right). It is the first moment at which saltation is seen for height $3R$. The left image is exactly one frame after, at 0.558 s, and it is the first moment in which the PIV program detects the particle and assigns it a value of 2.6 m/s.

Appendix B

Tuft test Results

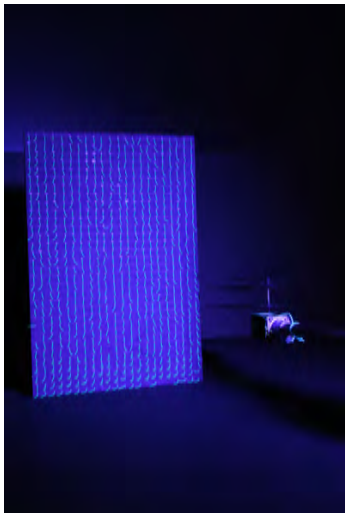

(a) Vertical Big Board

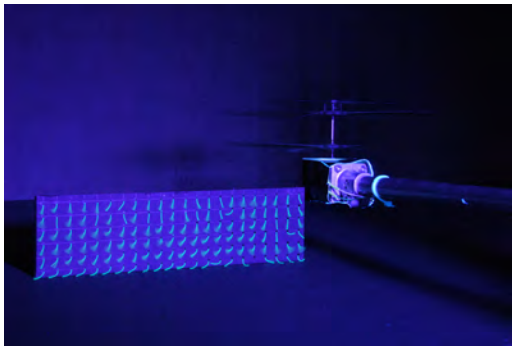

(b) Vertical Small Board

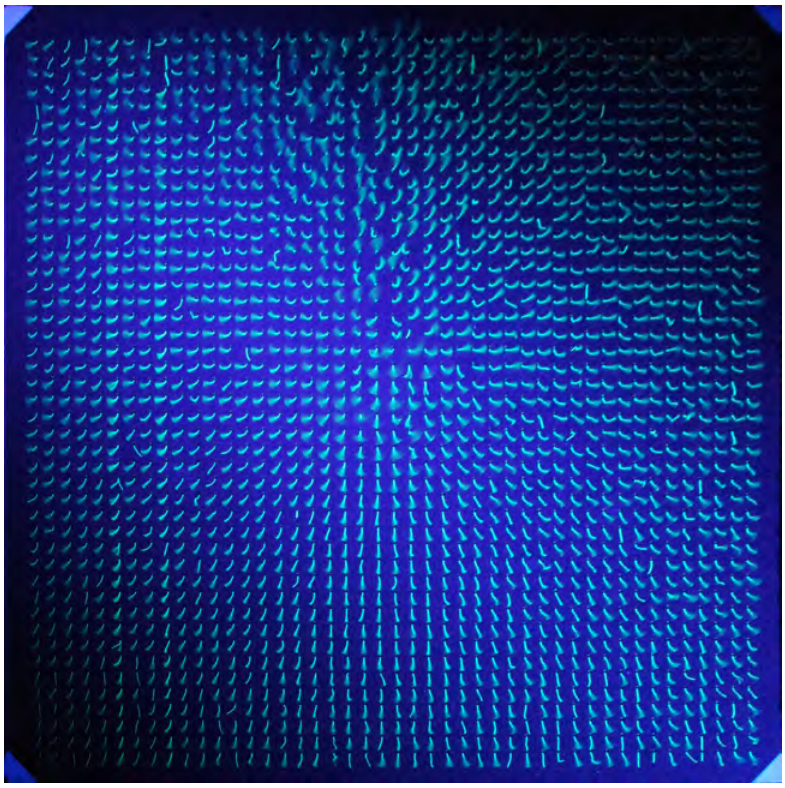

(c) Ground Board

Figure B.1: Tuft pattern visualization of the vertical and horizontal boards with height "wheels on ground" and plane inclination zero.

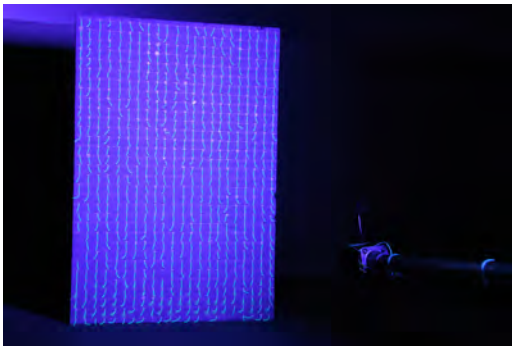

(a) Vertical Big Board (Left)

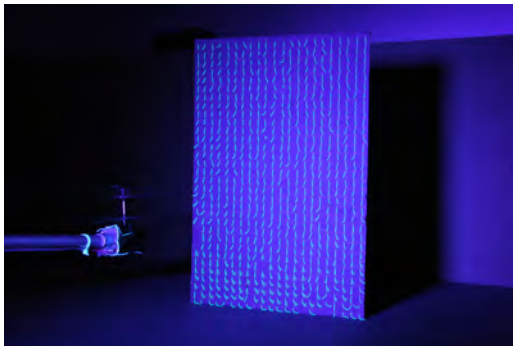

(b) Vertical Big Board (Right)

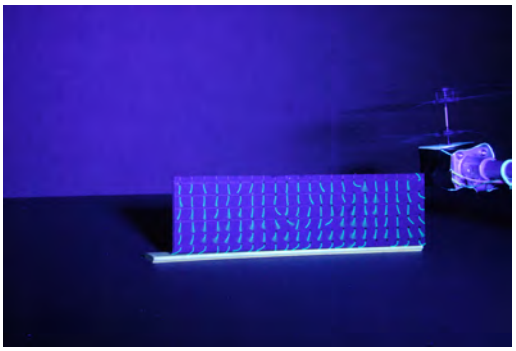

(c) Vertical Small Board (Left)

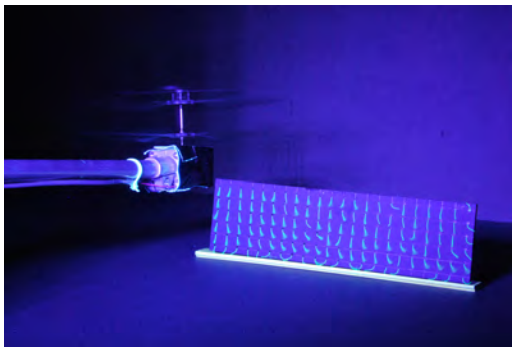

(d) Vertical Small Board (Right)

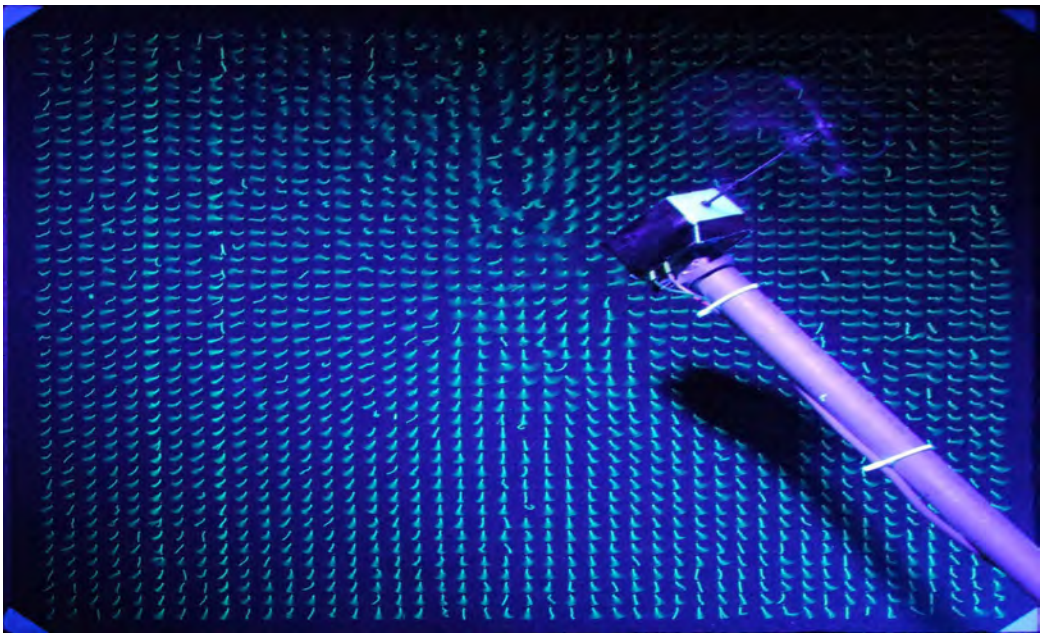

(e) Ground Board

Figure B.2: Tuft pattern visualization of the vertical and horizontal boards with height "wheels on ground" and plane inclination of 5°.

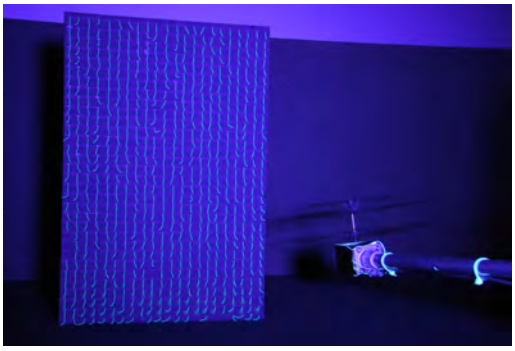

(a) Vertical Big Board (Left)

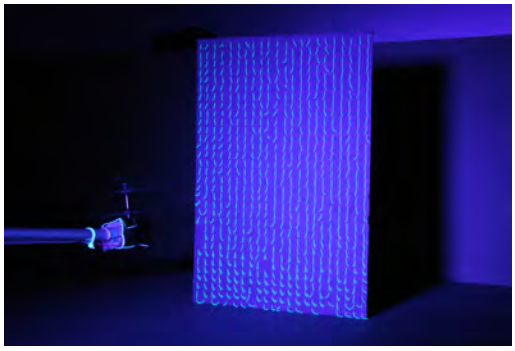

(b) Vertical Big Board (Right)

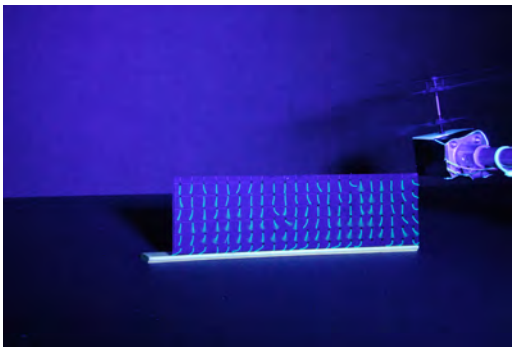

(c) Vertical Small Board (Left)

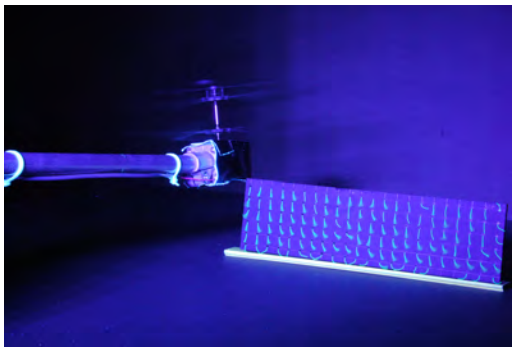

(d) Vertical Small Board (Right)

(e) Ground Board

Figure B.3: Tuft pattern visualization of the vertical and horizontal boards with height "wheels on ground" and plane inclination of 10°.

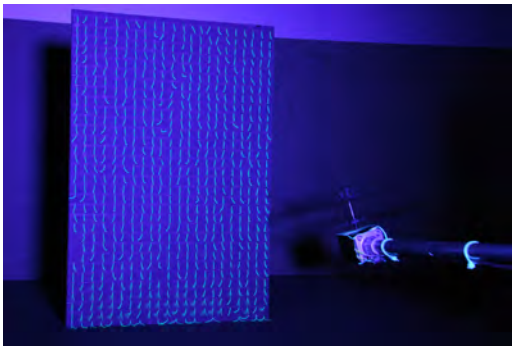

(a) Vertical Big Board (Left)

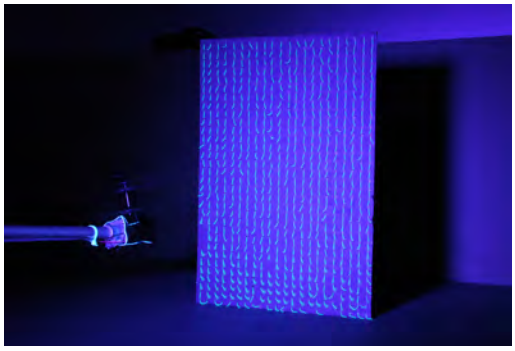

(b) Vertical Big Board (Right)

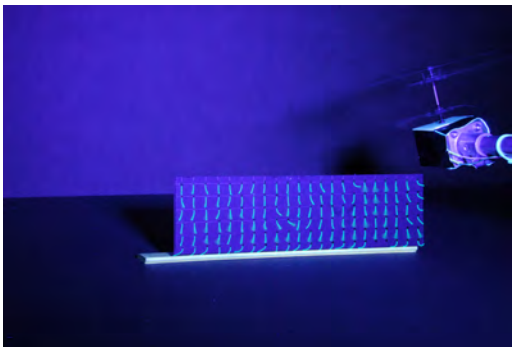

(c) Vertical Small Board (Left)

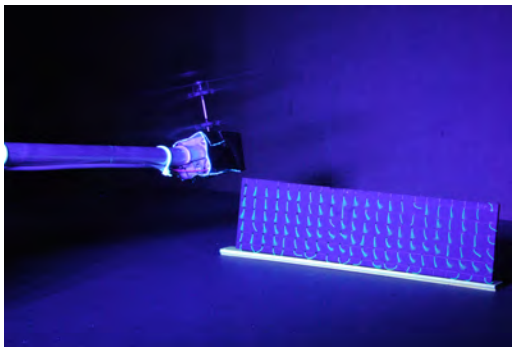

(d) Vertical Small Board (Right)

(e) Ground Board

Figure B.4: Tuft pattern visualization of the vertical and horizontal boards with height "wheels on ground" and plane inclination of 15°.

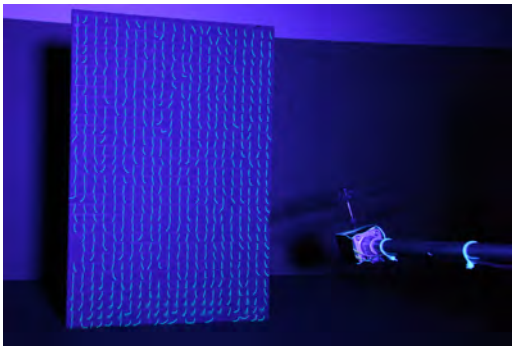

(a) Vertical Big Board (Left)

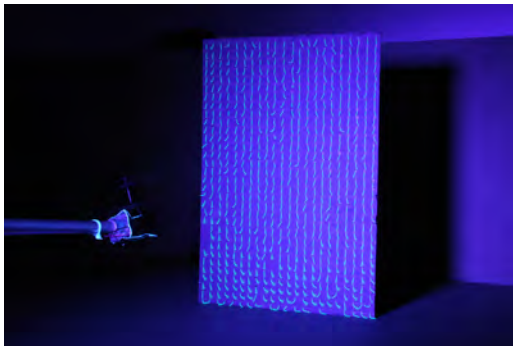

(b) Vertical Big Board (Right)

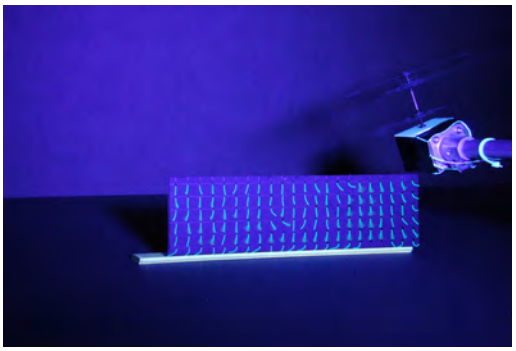

(c) Vertical Small Board (Left)

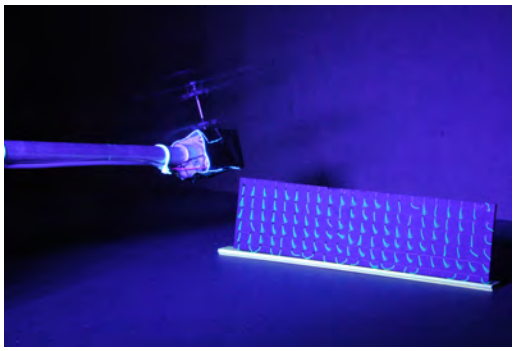

(d) Vertical Small Board (Right)

(e) Ground Board

Figure B.5: Tuft pattern visualization of the vertical and horizontal boards with height "wheels on ground" and plane inclination of 20°.

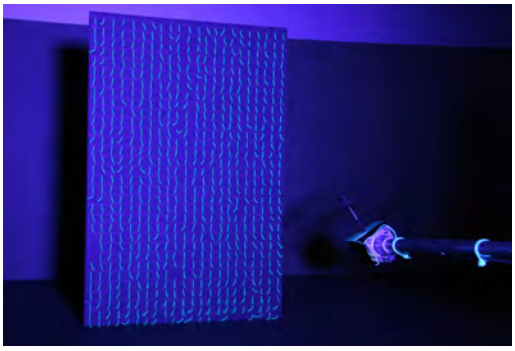

(a) Vertical Big Board (Left)

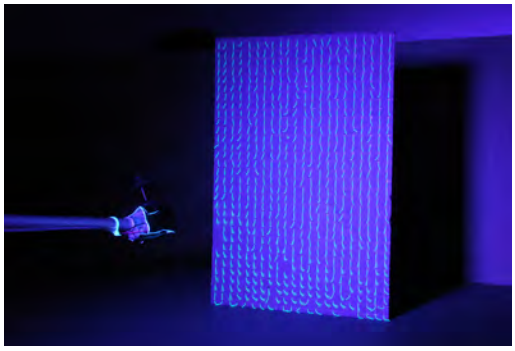

(b) Vertical Big Board (Right)

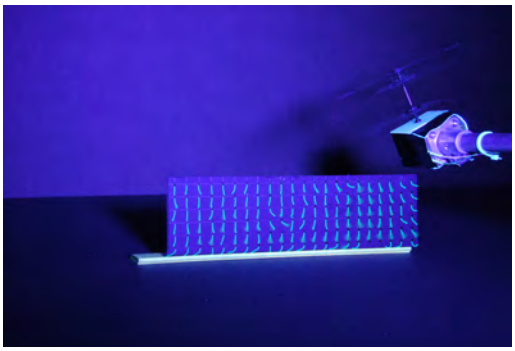

(c) Vertical Small Board (Left)

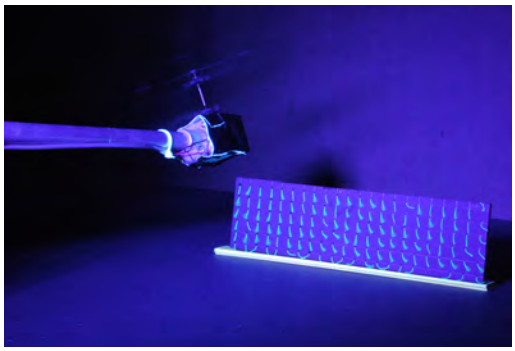

(d) Vertical Small Board (Right)

(e) Ground Board

Figure B.6: Tuft pattern visualization of the vertical and horizontal boards with height "wheels on ground" and plane inclination of 25°.

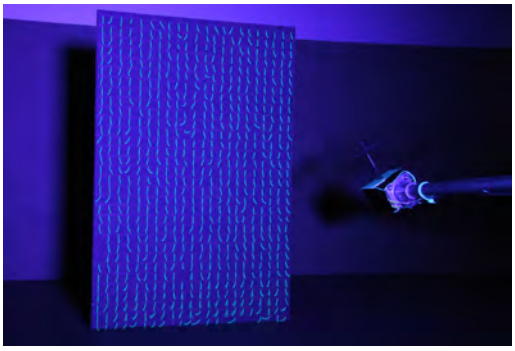

(a) Vertical Big Board (Left)

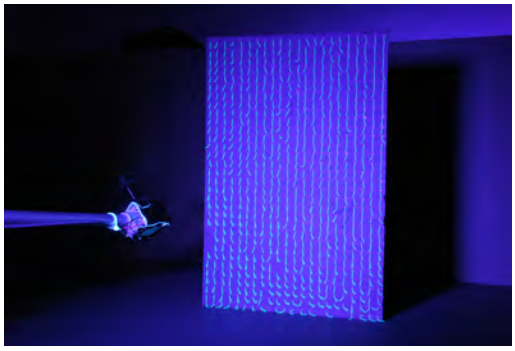

(b) Vertical Big Board (Right)

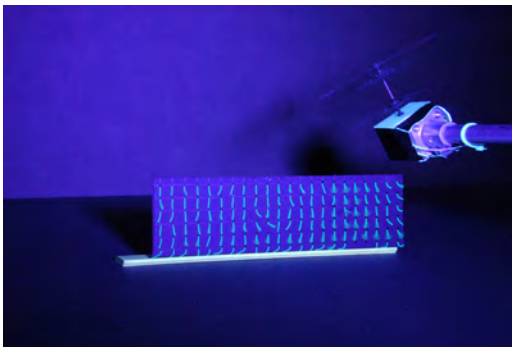

(c) Vertical Small Board (Left)

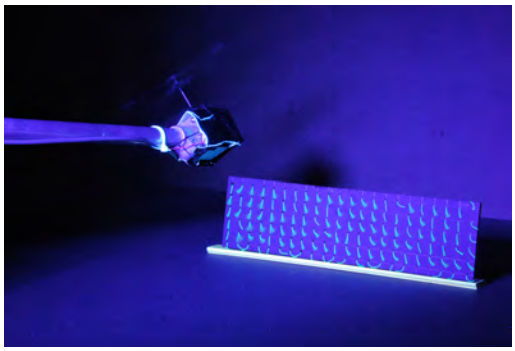

(d) Vertical Small Board (Right)

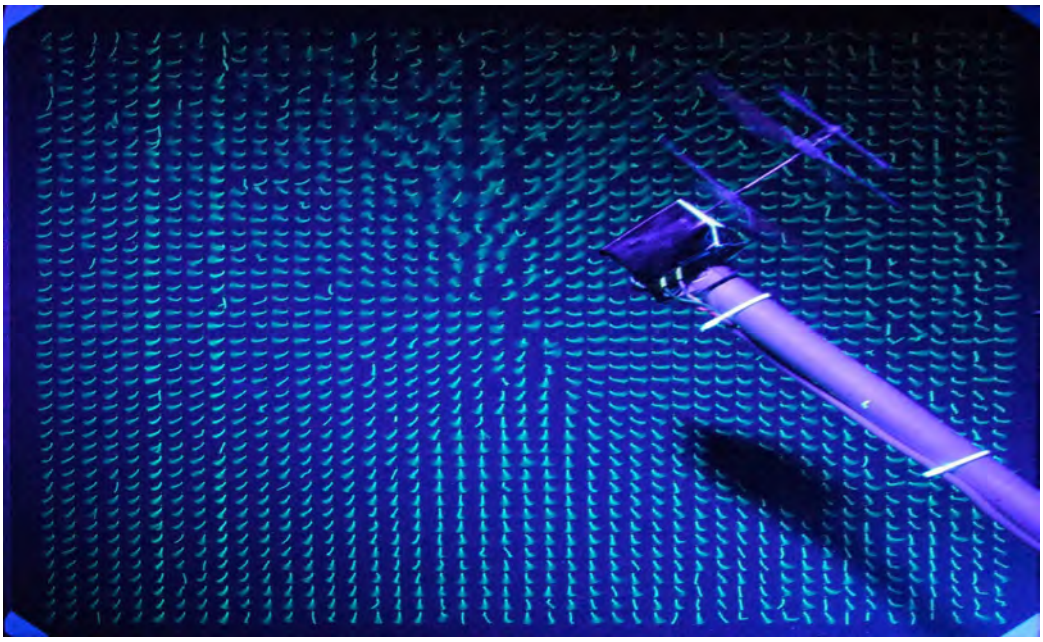

(e) Ground Board

Figure B.7: Tuft pattern visualization of the vertical and horizontal boards with height "wheels on ground" and plane inclination of 30°.

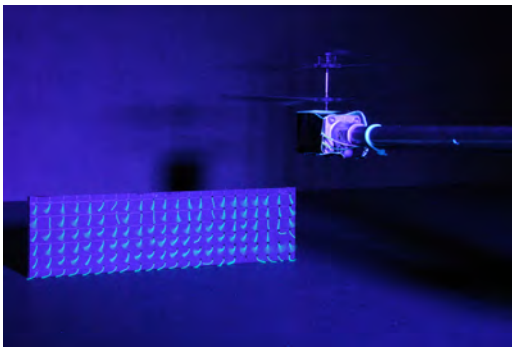

(a) Vertical Small Board (Left)

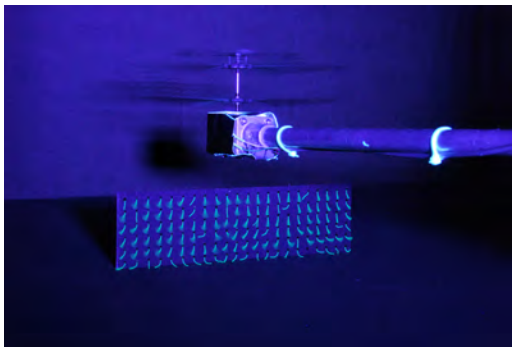

(b) Vertical Small Board (Right)

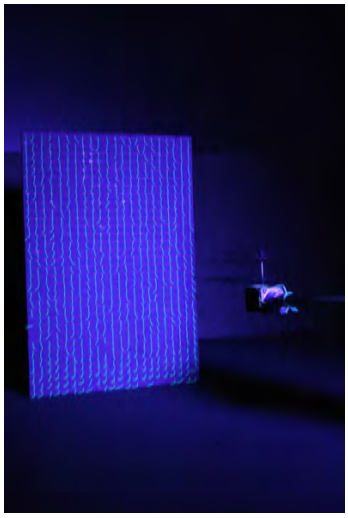

(c) Vertical Big Board

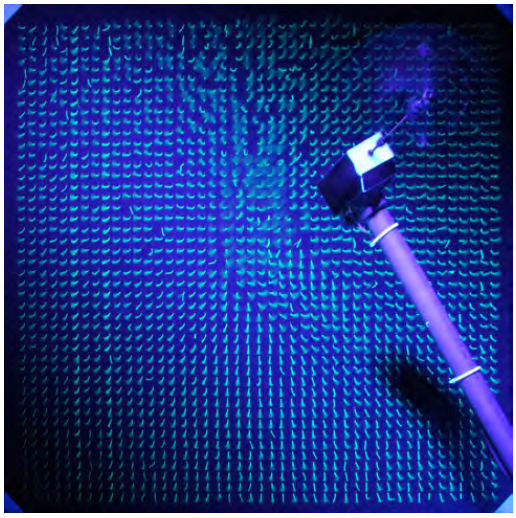

(d) Ground Board

Figure B.8: Tuft pattern visualization of the vertical and horizontal boards with height "15 cm drop" and plane inclination zero.

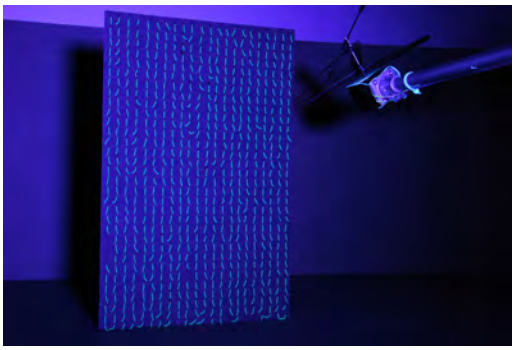

(a) Vertical Big Board (Left)

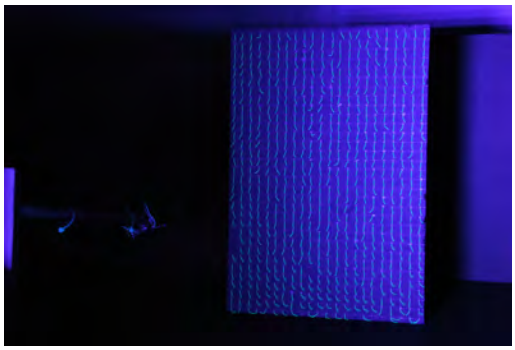

(b) Vertical Big Board (Right)

(c) Ground Board

Figure B.9: Tuft pattern visualization of the vertical and horizontal boards with height "15 cm drop" and plane inclination of 30°.

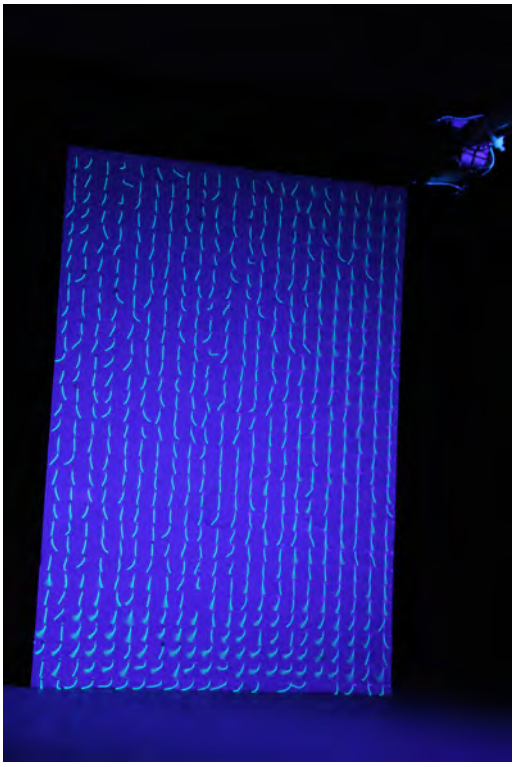

(a) Vertical Board (under rotor)

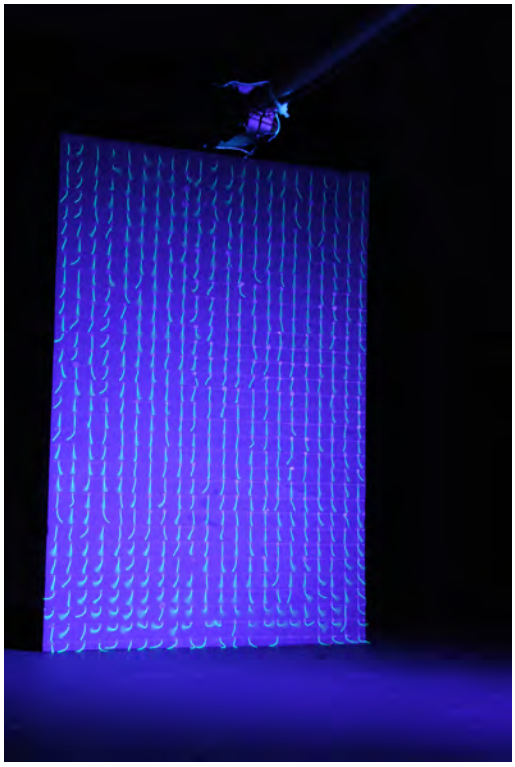

(b) Vertical Board (center)

(c) Vertical Board (Left)

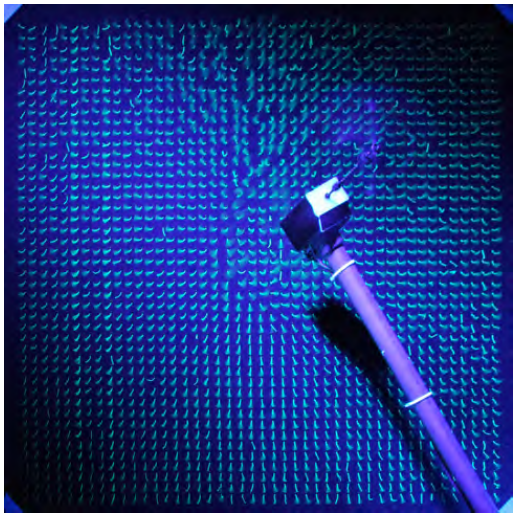

(d) Ground Board

Figure B.10: Tuft pattern visualization of the vertical and horizontal boards with height $3R$ and plane inclination zero.

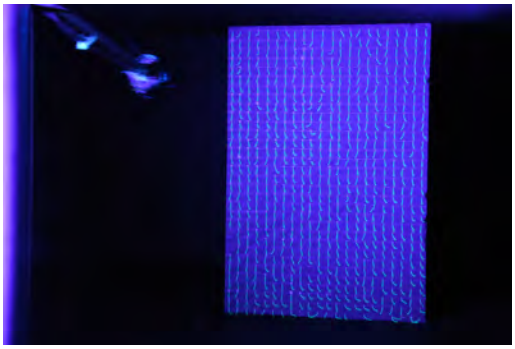

(a) Vertical Big Board (Left)

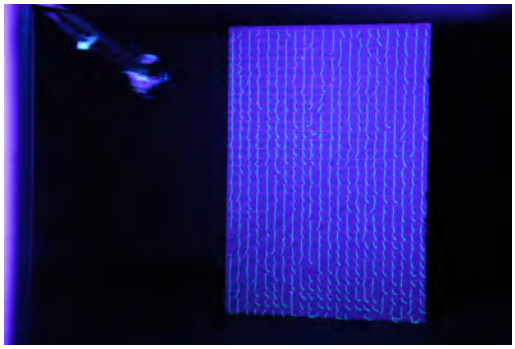

(b) Vertical Big Board (center)

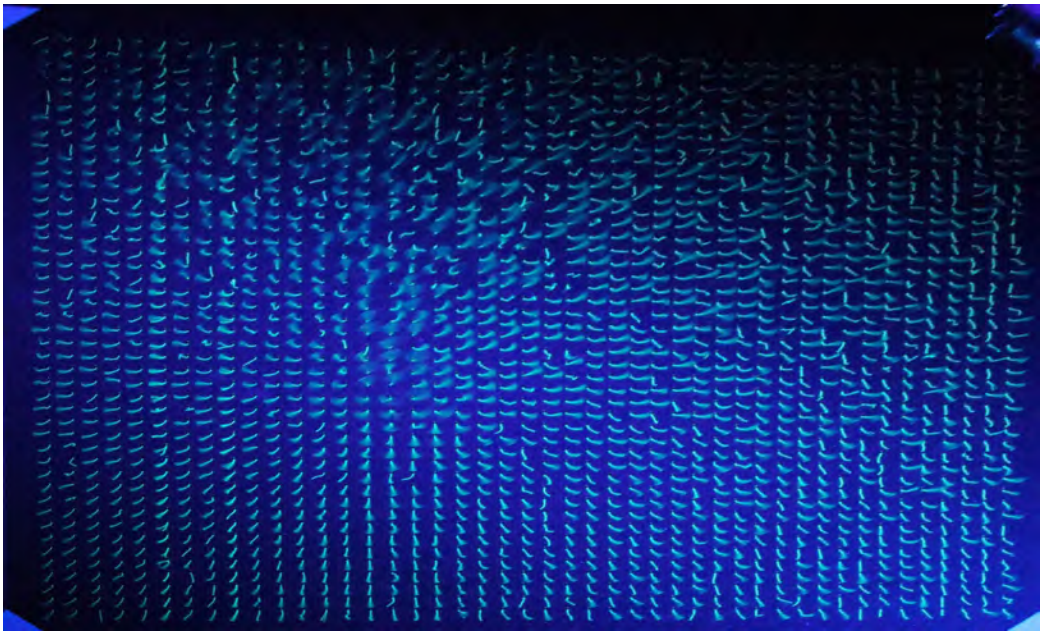

(c) Ground Board

Figure B.11: Tuft pattern visualization of the vertical and horizontal boards with height $3R$ and plane inclination of 30°.

Appendix C

Simulation Results

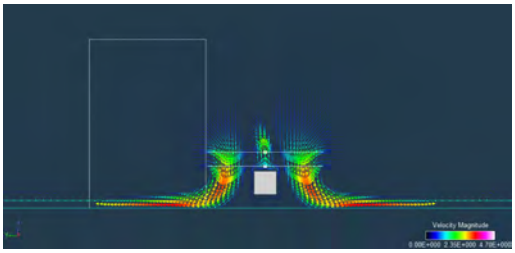

(a) Vertical Big Board

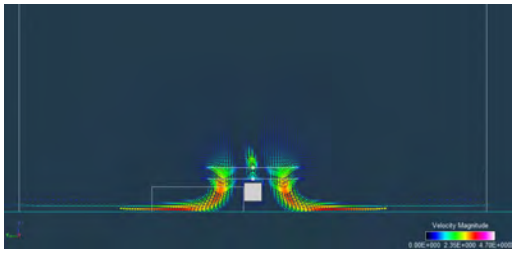

(b) Vertical Small Board

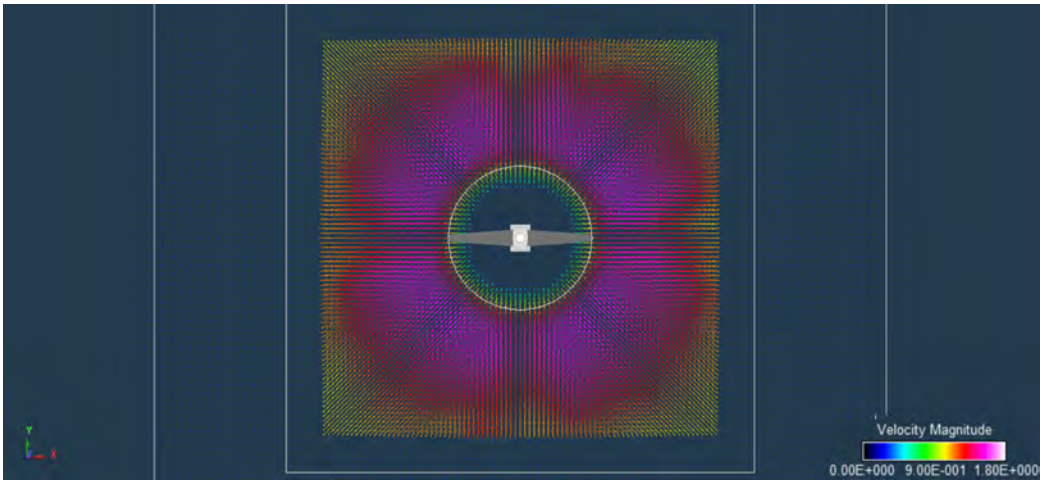

(c) Ground Board

Figure C.1: Flow field visualization of the vertical and horizontal planes with height "wheels on ground" and plane inclination zero.

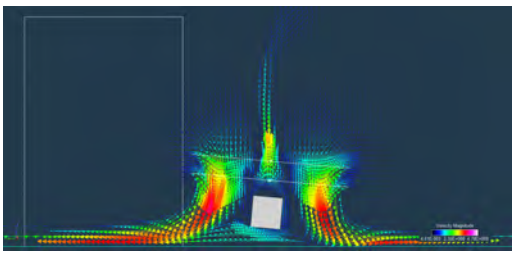

(a) Vertical Big Board (Left)

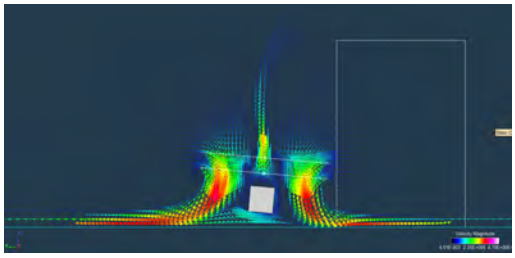

(b) Vertical Big Board (Right)

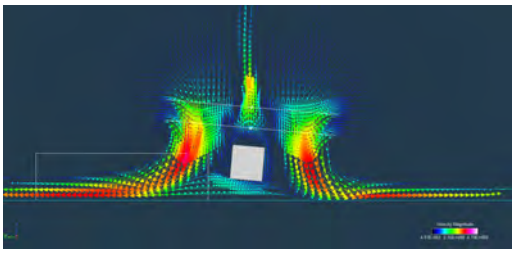

(c) Vertical Small Board (Left)

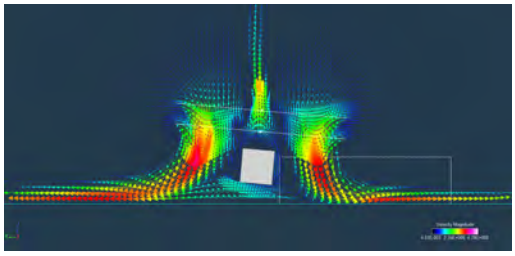

(d) Vertical Small Board (Right)

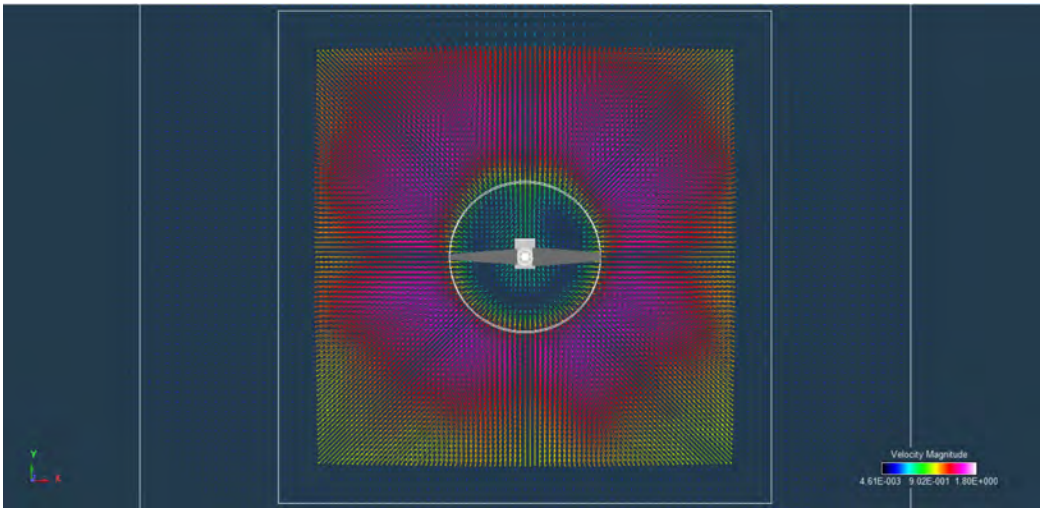

(e) Ground Board

Figure C.2: Flow field visualization of the vertical and horizontal planes with height "wheels on ground" and plane inclination of 5°.

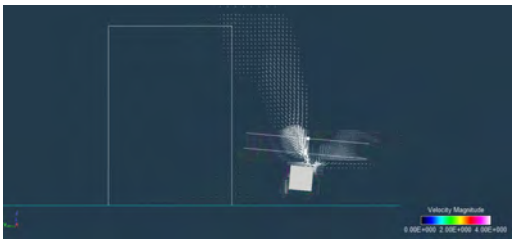

(a) Vertical Big Board (Left)

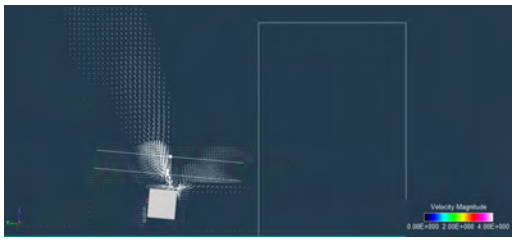

(b) Vertical Big Board (Right)

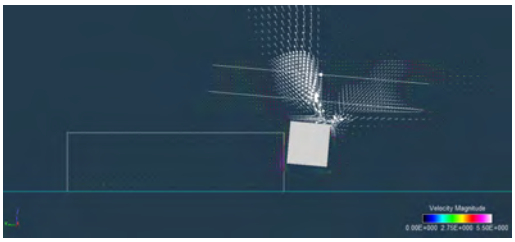

(c) Vertical Small Board (Left)

(d) Vertical Small Board (Right)

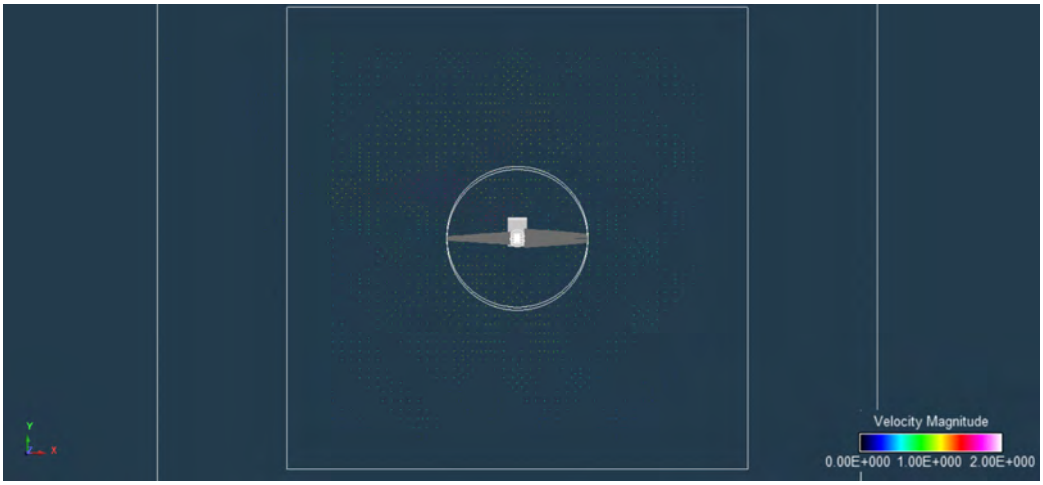

(e) Ground Board

Figure C.3: Flow field visualization of the vertical and horizontal planes with height "wheels on ground" and plane inclination of 10°.

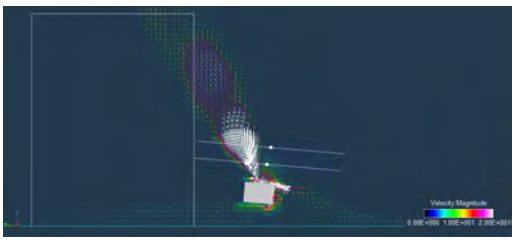

(a) Vertical Big Board (Left)

(b) Vertical Big Board (Right)

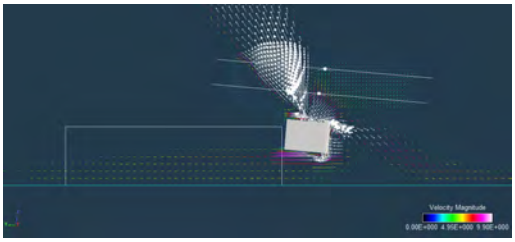

(c) Vertical Small Board (Left)

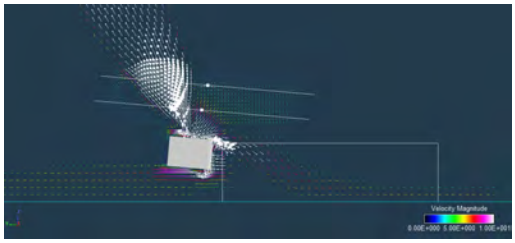

(d) Vertical Small Board (Right)

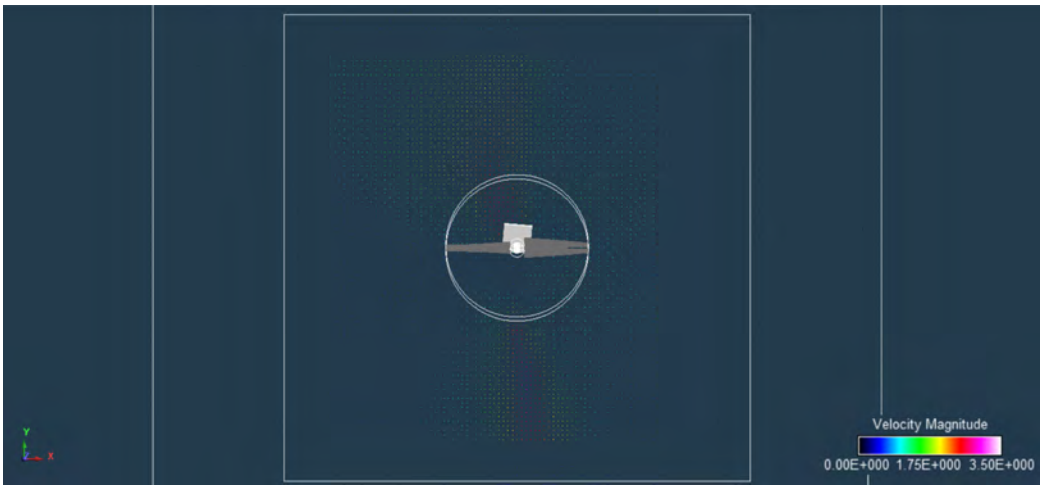

(e) Ground Board

Figure C.4: Flow field visualization of the vertical and horizontal planes with height "wheels on ground" and plane inclination of 15°.

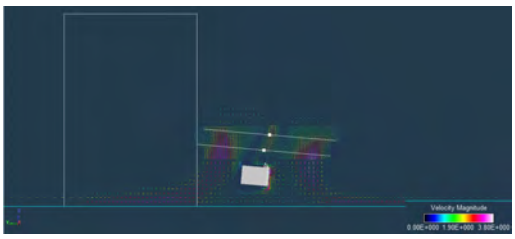

(a) Vertical Big Board (Left)

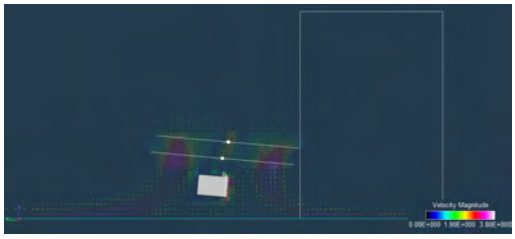

(b) Vetical Big Board (Right)

(c) Vertical Small Board (Left)

(d) Vertical Small Board (Right)

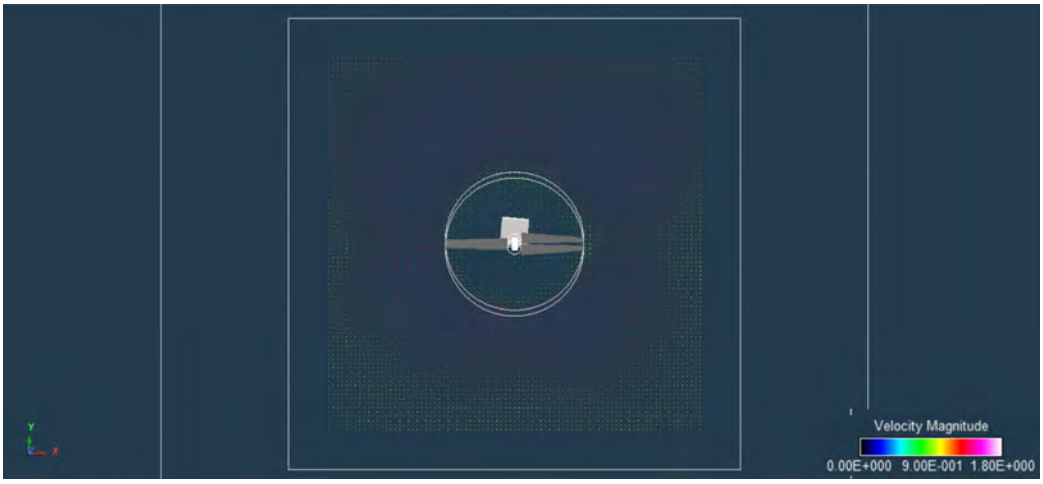

(e) Ground Board

Figure C.5: Flow field visualization of the vertical and horizontal planes with height "wheels on ground" and plane inclination of 20°.

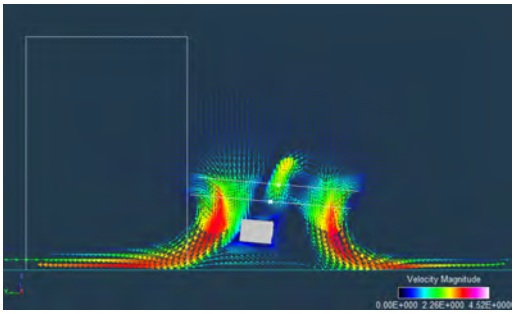

(a) Vertical Big Board (Left)

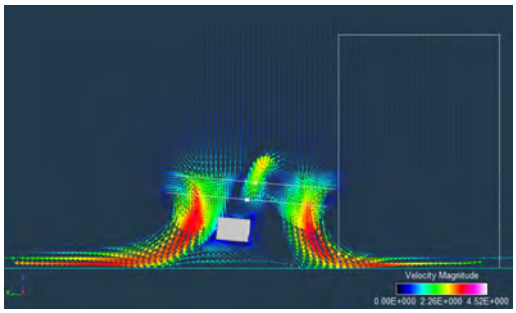

(b) Vertical Big Board (Right)

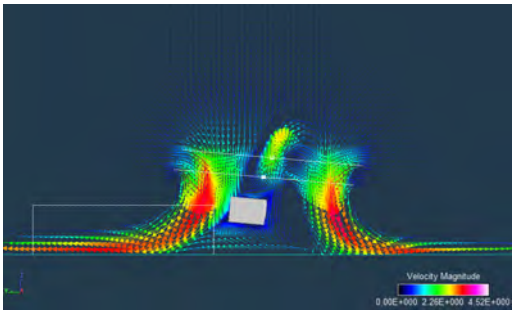

(c) Vertical Small Board (Left)

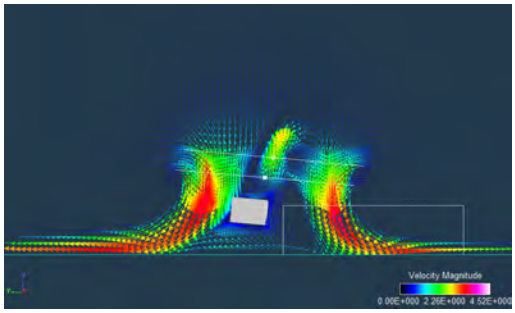

(d) Vertical Small Board (Right)

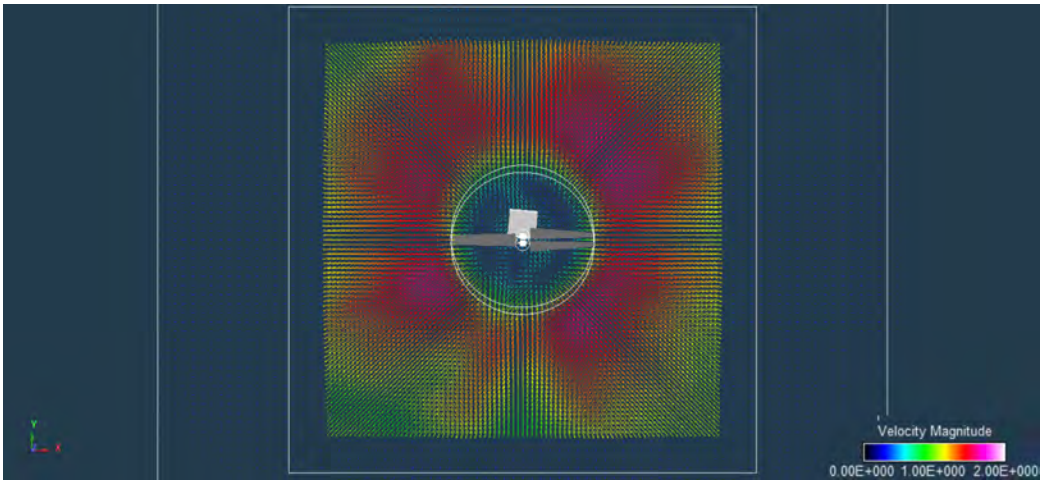

(e) Ground Board

Figure C.6: Flow field visualization of the vertical and horizontal planes with height "wheels on ground" and plane inclination of 25°.

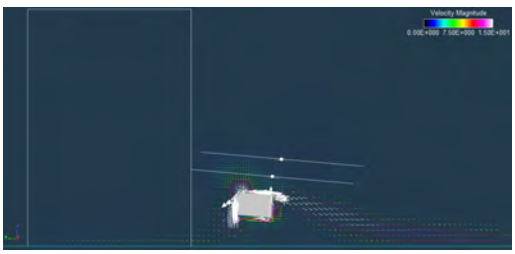

(a) Vertical Big Board (Left)

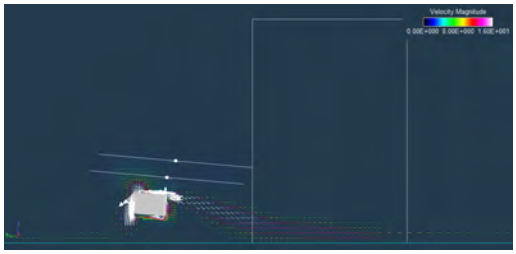

(b) Vertical Big Board (Right)

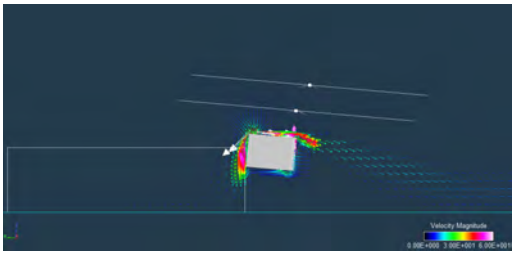

(c) Vertical Small Board (Left)

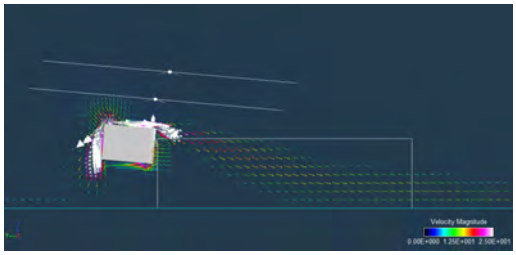

(d) Vertical Small Board (Right)

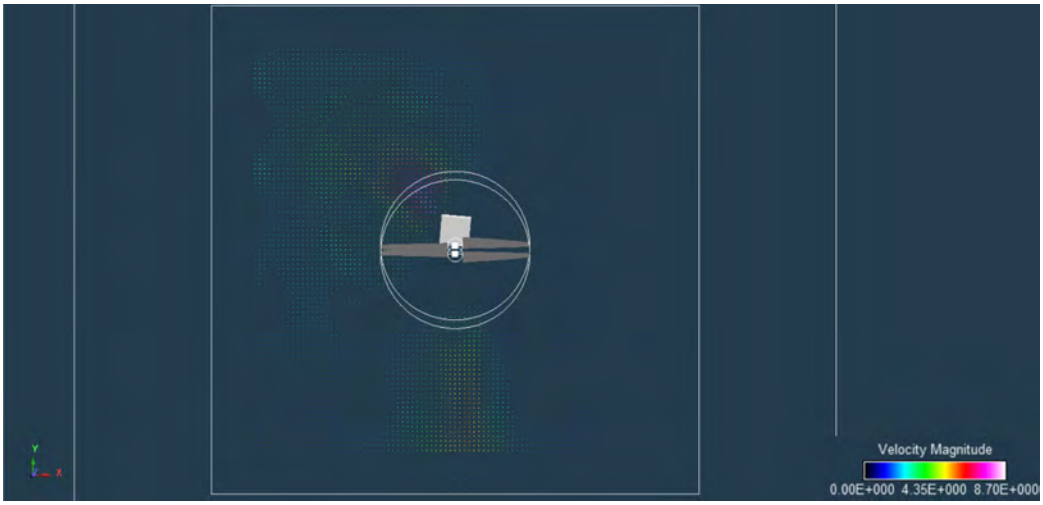

(e) Ground Board

Figure C.7: Flow field visualization of the vertical and horizontal planes with height "wheels on ground" and plane inclination of 30°.

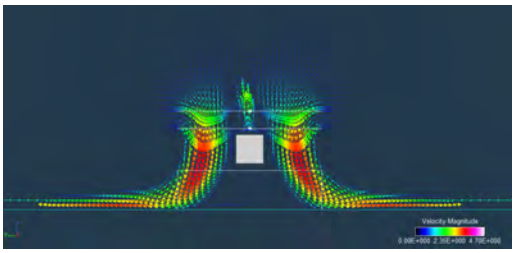

(a) Vertical Small Board (Left)

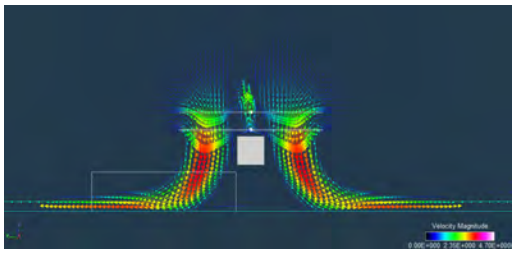

(b) Vertical Small Board (Under)

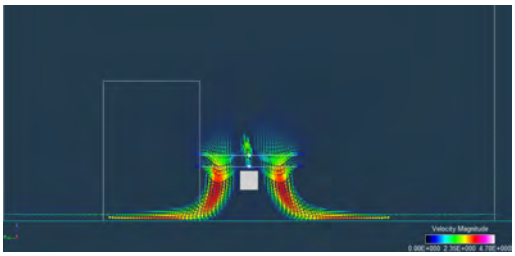

(c) Vertical Big Board (Left)

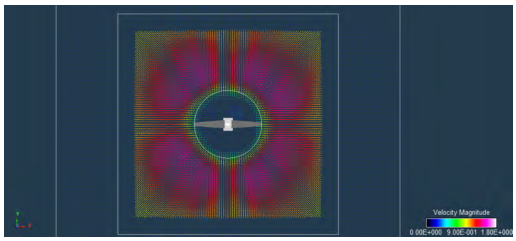

(d) Ground Board

Figure C.8: Flow field visualization of the vertical and horizontal planes with height "15 cm drop" and plane inclination zero.

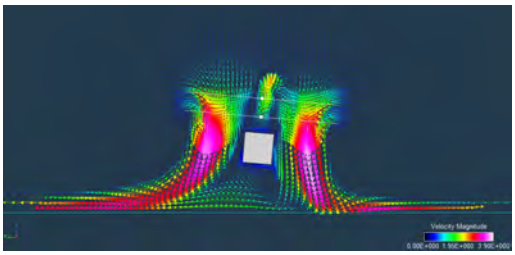

(a) Vertical Plane

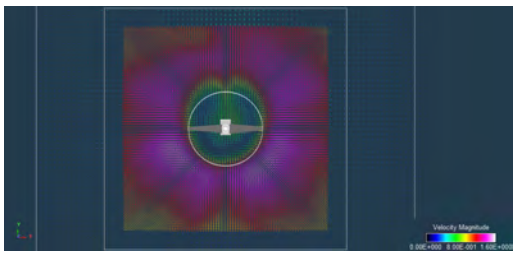

(b) Ground Plane

Figure C.9: Flow field visualization of the vertical and horizontal planes with height "15 cm drop" and plane inclination of 5°.

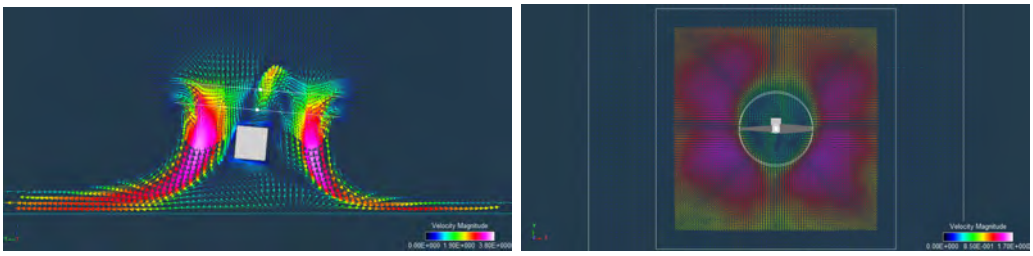

(a) Vertical Plane (b) Ground Plane

Figure C.10: Flow field visualization of the vertical and horizontal planes with height "15 cm drop" and plane inclination of 10°.

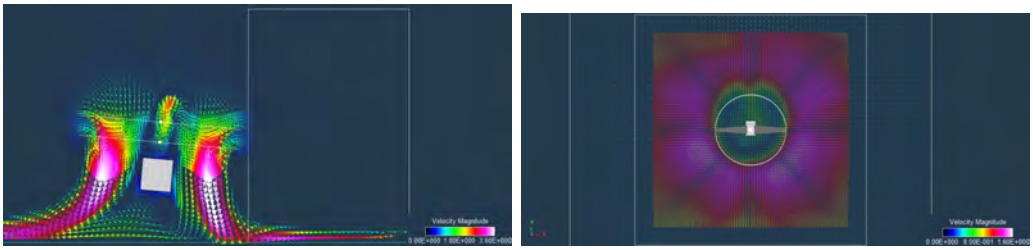

(a) Vertical Plane (b) Ground Plane

Figure C.11: Flow field visualization of the vertical and horizontal planes with height "15 cm drop" and plane inclination of 15°.

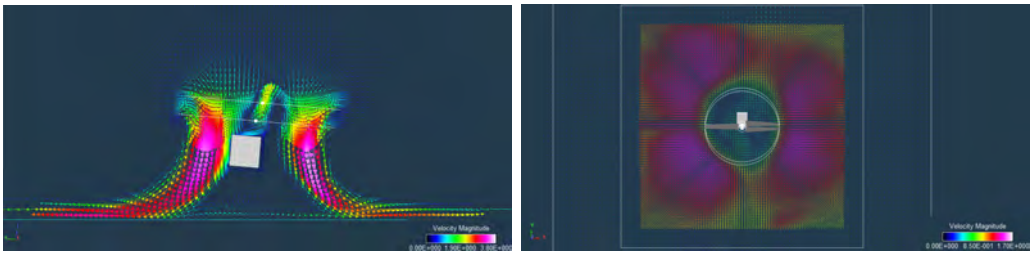

(a) Vertical Plane (b) Ground Plane

Figure C.12: Flow field visualization of the vertical and horizontal planes with height "15 cm drop" and plane inclination of 20°.

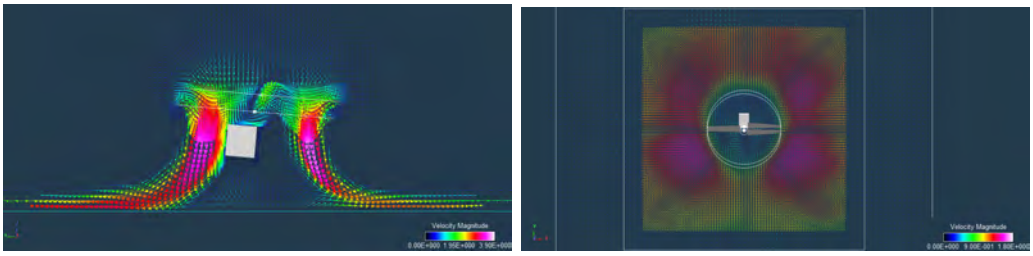

(a) Vertical Plane (b) Ground Plane

Figure C.13: Flow field visualization of the vertical and horizontal planes with height "15 cm drop" and plane inclination of 25°.

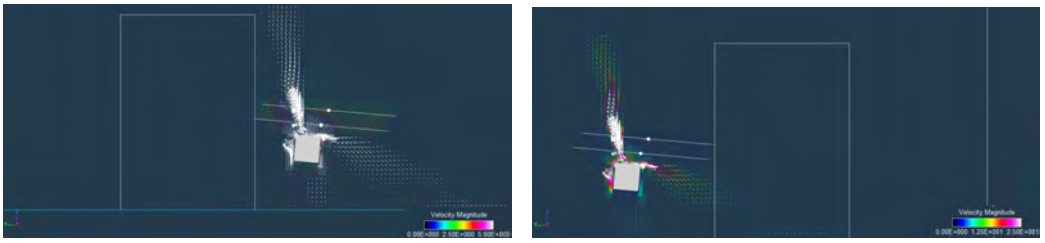

(a) Vertical Big Board (Left) (b) Vertical Big Board (Right)

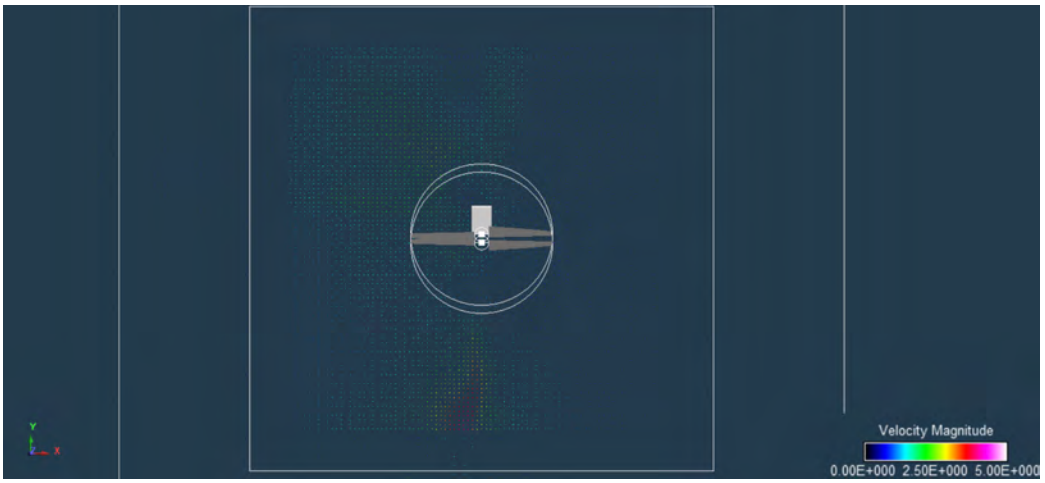

(c) Ground Board

Figure C.14: Flow field visualization of the vertical and horizontal planes with height "15 cm drop" and plane inclination of 30°.

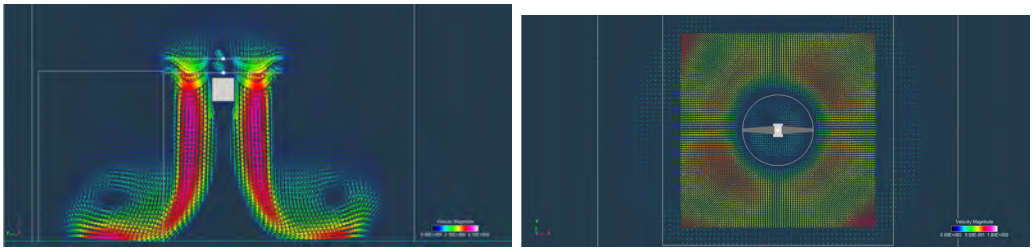

(a) Vertical Big Board (Left) (b) Ground Board

Figure C.15: Flow field visualization of the vertical and horizontal planes with height $3R$ and plane inclination zero.

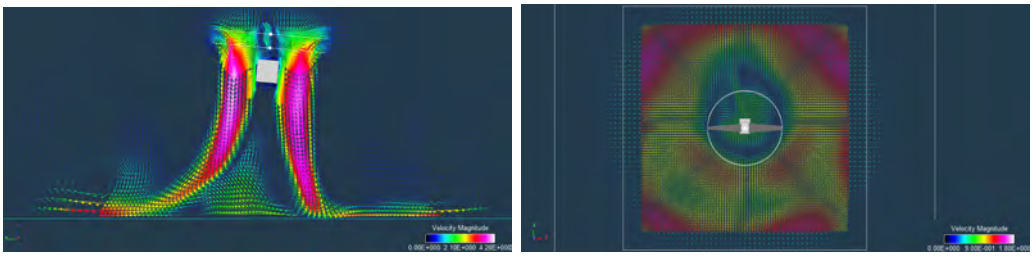

(a) Vertical plane (b) Ground plane

Figure C.16: Flow field visualization of the vertical and horizontal planes with height $3R$ and plane inclination of $5°$.

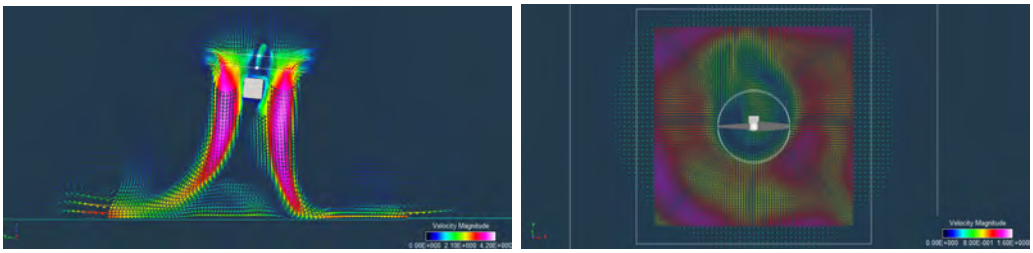

(a) Vertical plane (b) Ground plane

Figure C.17: Flow field visualization of the vertical and horizontal planes with height $3R$ and plane inclination of $10°$.

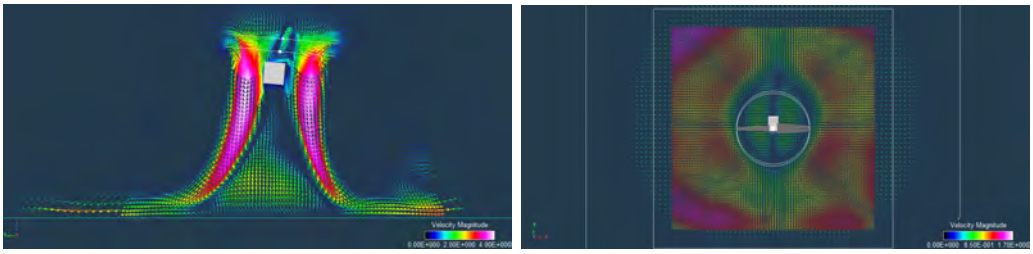

(a) Vertical plane (b) Ground plane

Figure C.18: Flow field visualization of the vertical and horizontal planes with height $3R$ and plane inclination of 15°.

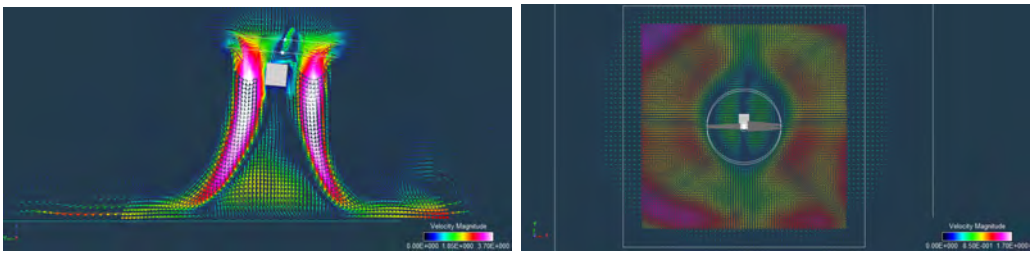

(a) Vertical plane (b) Ground plane

Figure C.19: Flow field visualization of the vertical and horizontal planes with height $3R$ and plane inclination of 20°.

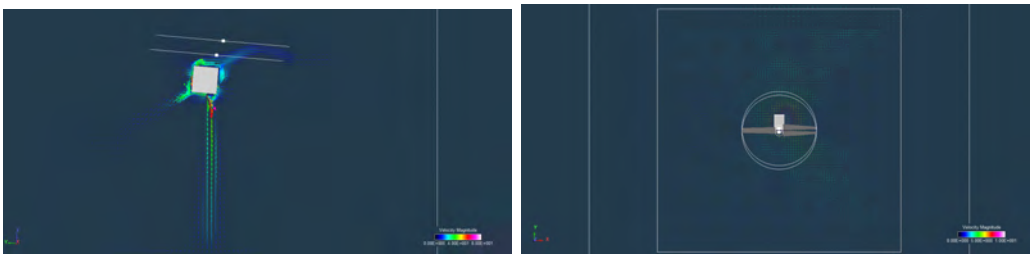

(a) Vertical plane (b) Ground plane

Figure C.20: Flow field visualization of the vertical and horizontal planes with height $3R$ and plane inclination of 25°.

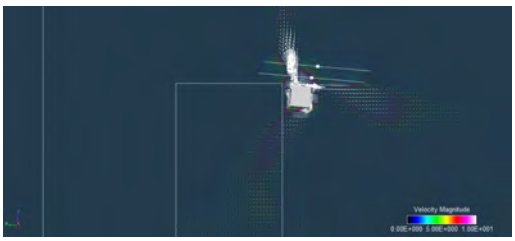

(a) Vertical Big Board (Left)

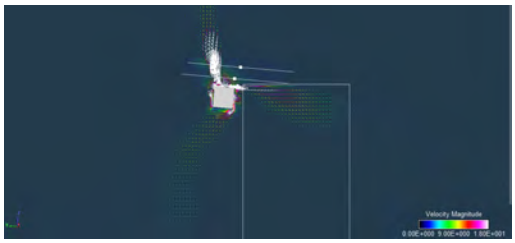

(b) Vertical Big Board (Right)

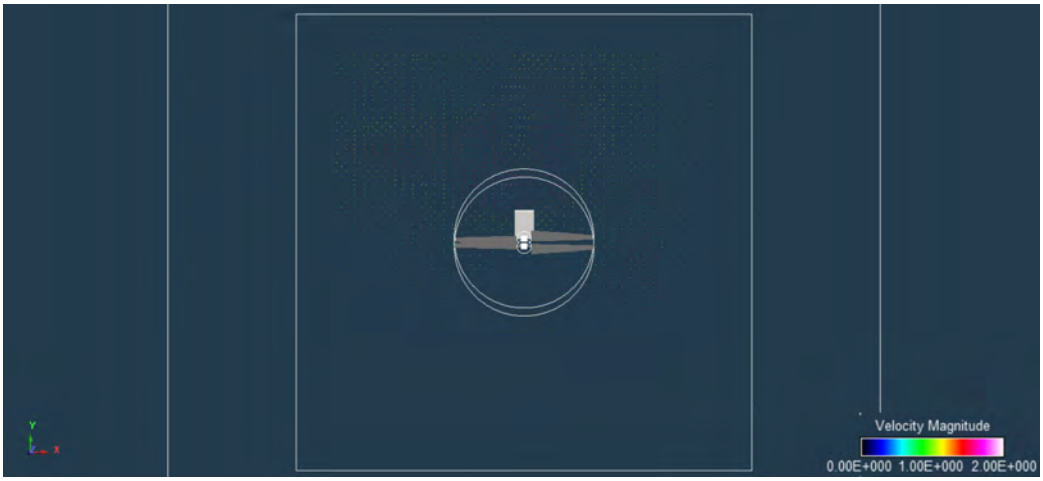

(c) Ground Board

Figure C.21: Flow field visualization of the vertical and horizontal planes with height $3R$ and plane inclination of 30°.

Bibliography

[1] Landau, E. (2015, January 22). Helicopter Could Be Scout for Mars Rover. https://www.jpl.nasa.gov/news/news.php?feature=4457

[2] Wadcock, Alan J., Ewing, Lindsay A., Solis, Eduardo, Potsdam, Mark, Rajagopalan, Ganech 2008 "Rotorcraft Downwash Flow Field Study to Understand the Aerodynamics of Helicopter Brownout" . *American Helicopter Society*

[3] Greeley, R., White, B. R., Pollack, J. B., Iversen, J.D. & Leach, R. N. Dust Storms on Mars: Considerations and Simulations, *NASA-TX-78423*

[4] Williams, D. A., & Smith, J. K. "NASA Facility overview: Planetary Aeolian Laboratory", 47th Lunar and Planetary Science Conference, 2016

[5] Volpe, R. 2014 Robotics Activities at JPL

[6] Young, L. A., Aiken, E. W., Derby, M. R., Johnson, J. L., Navarrete, J., Klem, J., Demblewski, R., Andrews, J. & Torres, R. Engineering Studies into Vertical Lift Planetary Aerial Vehicles, AHS International Meeting on Advanced Rotorcraft Technology and Life

[7] Lodders, K. & Fegley, Jr., B. "The planetary Scientist's Companion", Oxford University Press, 1998

[8] Rathakrishnan, Ethirajan. 2010 Applied Gas Dynamics *Wiley*

[9] Batchelor, G. K. 1967 An Introduction to Fluid Dynamics. *Cambridge University Press* **23**, 7–151.

[10] Johnson, W. 1980 Helicopter Theory. *Dover Publications, Inc.* 28–53, 122–123.

[11] Scanlan, J., Bishop, E. & Powe, R. 2000 Rotorcraft Flying Handbook. *Federal Aviation Administration* **FAA-H-8083-21** 1–1–3–11.

[12] Panigrahi, Durga C., Mishra, Devi P. May 2014 "CFD Simulations for the Selection of an Appropriate Blade Profile for Improving Energy Efficiency in Axial Flow Mine Ventilation Fans" . *Journal of Sustainable Mining*

[13] Bagnold, Ralph A. "The Physics of Blown Sand and Desert Dunes". *W. Morrow & Co.*, N.Y., 1942

[14] Kok,Jasper F.,Parteli, Eric J. R., Michaels, Timothy I.& Karam, Diana Bou 2012 "The physics of wind-blown sand and dust".*Rep. Prog. Phys.* 75 106901.

[15] Aldon, G.L. and Weinberger, R. K.Particle dislodgement entrainment by a low density airstream flowing over a surface . *NASA CR-111924,1972*

[16] Rajagopalan, R. G., Baskaran,V., Hollingsworth, A., Lestari, A., Garrick, D., Solis, E. & Hagerty, B. RotCFD - A Tool for Aerodynamic Interference of Rotors: Validation and Capabilities, AHS Future Vertical Lift Aircraft Design Conference, San Francisco CA, January 2012.

[17] NA "RotUNS Theory", Sukra Helitek, Inc., Ames, Iowa, November 30, 2016

[18] PIVlab - Digital Particle Image Velocimetry Tool for MATLAB: `http://pivlab.blogspot.com/` .

[19] `https://www.creaform3d.com/en/metrology-solutions/optical-3d-scanner-metrascan`

[20] Courant, R., Friedrichs, K., Lewy, H. September 1957, "On the partial difference equations of mathematical physics", *AEC Research and Development Report*,**NYO-7689**, New York: AEC Computing and Applied Mathematics Centre – Courant Institute of Mathematical Sciences,